

2007

## Parity-violation in elastic electron scattering: A first measurement of the parity-violating asymmetry at $Q^2 = 0.631 \text{ (GeV/c)}^2$ at backward angle

Stephanie L. Bailey  
*College of William & Mary - Arts & Sciences*

Follow this and additional works at: <https://scholarworks.wm.edu/etd>



Part of the [Physics Commons](#)

---

### Recommended Citation

Bailey, Stephanie L., "Parity-violation in elastic electron scattering: A first measurement of the parity-violating asymmetry at  $Q^2 = 0.631 \text{ (GeV/c)}^2$  at backward angle" (2007). *Dissertations, Theses, and Masters Projects*. Paper 1539623510.

<https://dx.doi.org/doi:10.21220/s2-nj2h-3k13>

This Dissertation is brought to you for free and open access by the Theses, Dissertations, & Master Projects at W&M ScholarWorks. It has been accepted for inclusion in Dissertations, Theses, and Masters Projects by an authorized administrator of W&M ScholarWorks. For more information, please contact [scholarworks@wm.edu](mailto:scholarworks@wm.edu).

# PARITY-VIOLATION IN ELASTIC ELECTRON SCATTERING

A First Measurement of the Parity-Violating  
Asymmetry at  $Q^2 = 0.631 \text{ (GeV/c)}^2$  at Backward Angle

---

A Dissertation

Presented to

The Faculty of the Department of Physics  
The College of William and Mary in Virginia

In Partial Fulfillment

Of the Requirements for the Degree of  
Doctor of Philosophy

---

by

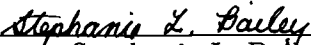
Stephanie L. Bailey

2007

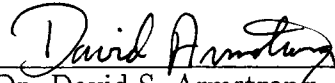
## APPROVAL SHEET


This dissertation is submitted in partial fulfillment of  
the requirements for the degree of

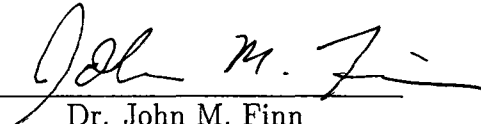
Doctor of Philosophy

  
Stephanie L. Bailey

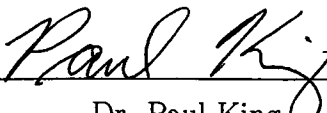
Approved, January 2007

  
Dr. David S. Armstrong, Chair

  
Dr. Todd Averett

  
Dr. John M. Finn

  
Dr. Jeffrey K. Nelson

  
Dr. Paul King  
Assistant Research Professor, Ohio University

## ACKNOWLEDGMENTS

I wish to thank my adviser David Armstrong for his guidance and support. I also wish to acknowledge and thank Paul King. I was very fortunate to have had the opportunity to work with Paul. Thank you for your teachings, help in code development and data analysis, and patience. I also wish to thank Riad Suleiman, my partner in parity quality beam. I would like to thank the  $G^0$  backward angle students Mat Muether, Colleen Ellis, Alex Coppens, John Schaub, Juliette Mammei, Maud Versteegen, and Goulven Guillard. I wish to acknowledge Jianglai Liu and Jeff Secrest for their help even after they completed their degrees and moved away. I also wish to thank Matt Poelker, John Hansknecht, and Joe Grames for their help in the injector. Thank you to Ryan Snyder (HAPPEX Collaboration) for training me in the laser room for many months. Many thanks to Fatiha Benmokthar for her help with the DAQ. I wish to acknowledge Larry Lee, Des Ramsey, and Gary Rutledge for their help in constructing the Cryostat Exit Detectors. Thanks to Mark Pitt for his help with the beam, Dave Mack for his feedback about my log entries, and Bill Vulcan for his grand smile and car honking. Thank you to Walter Kellner for his help in the hall and the Mexican cumbia. Thank you to Dave Gaskell and Tanja Horn for their Moller work. I owe a very special thank you to Michael Gericke for being my crutch. I wish you and your family a happy beginning in Canada. I will miss you.

Finally, I wish to thank my family and friends. To Yelena Prok and Stephen Bueltmann, thank you for your friendship and love. Thank you for the the hot cooked meals, long walks with Roscoe to the pier, ridiculous movies, stolen figs, racy novels, good Russian music, tennis games, and rose gardens. Thank you for showing me how good chesse and wine really are. You are both beautiful people and you lead beautiful lives. Be strong and don't lose spirit. To Sabine Fuchs and Klaus Grimm, thank you for always being there for me. Thank you for eating Top's with me, inviting me to ladies nights, cake and candles on all of my birthdays, and long heart-felt talks on the telephone. Thank you to Chris and Gail Kulp for your friendship and support. I really enjoyed my visit to Kentucky and your visits to Williamsburg. To my parents Michael and Deborah Bailey, my sisters Jacqueline Luders and Nichole McAdams and their families, and my grandmother Ruth Asrican and my late grandfather Phill Asrican, I could not have done this without you. Thank you for your support, encouragement and love. Thank you for taking care of me when I was sick and for lifting my spirits when I was down. Thank you for believing in me. I love you.

## CONTENTS

<b>LIST OF TABLES</b> . . . . .	<b>ix</b>
<b>LIST OF ILLUSTRATIONS</b> . . . . .	<b>xiv</b>
<b>CHAPTER</b>	
<b>1 Theory</b> . . . . .	<b>1</b>
1.1 The Quark Model . . . . .	1
1.2 Quantum Chromodynamics . . . . .	3
1.3 Strange Quarks in the Nucleon . . . . .	4
1.3.1 Strange Quark Contribution to the Nucleon's Momentum . . . . .	6
1.3.2 Strange Quark Contributions to the Nucleon's Mass . . . . .	7
1.3.3 Strange Quark Contributions to the Nucleon's Spin . . . . .	9
1.4 Electromagnetic Interaction . . . . .	11
1.5 Weak Neutral Interaction . . . . .	14
1.6 Weak Axial Form Factors . . . . .	14
1.7 Vector Form Factors . . . . .	15
1.8 Energy-Momentum 4-vector Transfer Squared . . . . .	18
1.9 Elastic Parity-Violating Electron Neutron Scattering . . . . .	20
1.9.1 Parity-Violating Asymmetry . . . . .	20
1.9.2 Higher Order Effects . . . . .	25
1.10 Unpolarized Electron Scattering . . . . .	29
1.10.1 Elastic Electron-Proton Scattering . . . . .	30

1.10.2	Electron-Deuteron Scattering . . . . .	30
1.11	Polarized Electron Scattering . . . . .	34
1.11.1	Elastic Electron-Proton Scattering . . . . .	34
1.12	Related Experiments . . . . .	35
1.12.1	SAMPLE . . . . .	36
1.12.2	HAPPEX . . . . .	38
1.12.3	PVA4 . . . . .	41
1.12.4	$G^0$ Forward Angle Experiment . . . . .	43
1.12.5	World Data on Strange Form Factors at $Q^2 = 0.1 \text{ GeV}^2$ . .	44
<b>2</b>	<b><math>G^0</math> Experimental Equipment . . . . .</b>	<b>47</b>
2.1	Experimental Overview . . . . .	47
2.2	Magnet . . . . .	49
2.3	Target . . . . .	51
2.4	Detectors . . . . .	54
2.4.1	Focal Plane Detector . . . . .	54
2.4.2	Cryostat Exit Detectors . . . . .	56
2.4.3	Aerogel Cherenkov Detectors . . . . .	58
2.5	Electronics . . . . .	62
2.6	Beam Instrumentation . . . . .	63
2.6.1	Beam Current Monitors . . . . .	64
2.6.2	Beam Position Monitors . . . . .	65
2.6.3	Halo Monitors . . . . .	68
2.6.4	Lumi Monitors . . . . .	72
2.6.5	Polarimetry . . . . .	74
2.6.6	Coil Modulation . . . . .	78
2.7	DAQ . . . . .	80

<b>3</b>	<b>The Polarized Electron Source</b>	<b>83</b>
3.1	CEBAF Accelerator	83
3.2	Polarized Electron Source	84
3.2.1	Photocathodes	85
3.2.2	The Laser System	89
3.2.3	Optical Elements in Source	91
3.3	Beam Structure	96
3.4	Types of Laser Systematics	97
3.4.1	Charge Asymmetry	97
3.4.2	Position Differences	99
3.5	Controlling Laser Systematics	101
3.5.1	Controlling Charge Asymmetries	101
3.5.2	Controlling Position Differences	106
3.6	PC Installation Procedure	108
<b>4</b>	<b>Analysis</b>	<b>110</b>
4.1	Raw Data Management and Processing	110
4.2	Nominal Running Conditions	112
4.3	The Measured Asymmetry	112
4.4	Cerenkov Efficiencies	113
4.5	CED-FPD Matrix Space Cuts	116
4.6	Deadtime	119
4.7	Linear Regression	126
4.7.1	Formalism	127
4.7.2	Slope Stability	131
4.7.3	Slopes Before and After Deadtime	135
4.7.4	A Comparison of Raw and Corrected Yields	140

4.7.5	Target Projections by Different Sets of BPMs . . . . .	141
4.7.6	A Comparison of Natural Beam Motion and Coil Modulation	147
4.7.7	Simulation of the Slopes . . . . .	154
4.7.8	Conclusion on Beam Correction Method . . . . .	156
4.8	Background . . . . .	157
4.9	Beam Polarization . . . . .	159
<b>5</b>	<b>Results . . . . .</b>	<b>162</b>
5.1	Introduction . . . . .	162
5.2	Parity Quality Beam . . . . .	162
5.3	Raw Asymmetry . . . . .	165
5.4	Physics Asymmetry . . . . .	169
5.5	Strange Form Factors . . . . .	170
5.5.1	Parametrization of the Electromagnetic Form Factors . . .	171
5.5.2	Parameterization of the Axial Form Factor . . . . .	172
5.5.3	Results . . . . .	173
<b>APPENDIX A</b>		
	<b>Mathematical Identities . . . . .</b>	<b>176</b>
<b>APPENDIX B</b>		
	<b>Construction and Assembly of CEDs . . . . .</b>	<b>179</b>
<b>BIBLIOGRAPHY . . . . .</b>		<b>184</b>
<b>VITA . . . . .</b>		<b>189</b>



## LIST OF TABLES

1.1	Quark masses. . . . .	5
1.2	Electroweak couplings of charged fundamental particles. . . . .	15
1.3	One-quark vector electroweak radiative correction parameters. . . . .	28
1.4	Multi-quark axial electroweak radiative correction parameters. . . . .	29
1.5	Contributors to recent world data on the electric form factor of the neutron. . . . .	32
1.6	Contributors to recent world data on the proton form factor ratio. . . . .	35
2.1	Halo measurements to determine if the halo specification is achieved. . . . .	72
2.2	Range of motion for a typical run for both natural beam motion and coil modulation. . . . .	80
2.3	ROCS and their functions. . . . .	81
3.1	IA Voltage Scans. . . . .	104
3.2	IA Angle Scans. . . . .	105
4.1	Nominal running conditions. . . . .	112
4.2	Results of the deadtime correction. . . . .	126
4.3	Deadtime slopes presented as $p_1/p_0$ in units of $\%/ \mu A$ ( $10^{-3}$ ), where $p_0$ is the intercept and $p_1$ is the slope. . . . .	126

4.4	Helicity-correlated differences/asymmetries of individual parameters and average slope for all octants determined using natural beam motion and BPMs H00 and G0B. . . . .	145
4.5	Overall false asymmetry and false asymmetries of individual beam parameters determined using natural beam motion and BPMs H00 and G0B. . . . .	145
4.6	Helicity-correlated differences/asymmetries of individual parameters and average slope determined using natural beam motion and based on BPMs G0 and G0B for all octants. . . . .	146
4.7	Overall false asymmetry and false asymmetries of individual beam parameters determined using natural beam motion and based on BPMs G0 and G0B. . . . .	146
4.8	Average slopes for all octants and detectors as determined using coil modulation. . . . .	154
4.9	Overall false asymmetry and false asymmetries of individual beam parameters determined using coil modulation. . . . .	155
4.10	A comparison of the geometry amplitudes between simulation and the measured slopes from coil modulation. . . . .	155
4.11	A comparison of the slopes averaged over the 8 octants between the forward and backward angle experiments. . . . .	158
4.12	Moller and Mott measurements of beam polarization in April, 2006. .	161
5.1	Position differences obtained on the QPD when steering is the dominant effect (LP out) . . . . .	164
5.2	Position differences obtained on the QPD when phase gradients are the dominant effect (LP in). . . . .	164
5.3	The sizes and corresponding uncertainties of the systematic corrections leading to the physics asymmetry. . . . .	170

## LIST OF FIGURES

1.1	Measured values of $xs(x)$ vs $x$ from deep inelastic neutrino scattering.	7
1.2	The spin alignment of the strange quarks at $\langle Q^2 \rangle = 2.5 \text{ GeV}^2$ , as a function of Bjorken $x$ .	12
1.3	An electron $e$ scatters from a nucleon $N$ , exchanging a virtual photon $\gamma$ , left, and a neutral weak boson $Z^0$ , right.	21
1.4	Higher-order one-quark diagrams.	25
1.5	Higher-order multiple-quark diagrams.	26
1.6	Recent world data on the proton magnetic and electric form factors.	31
1.7	Recent world data on the electric form factor of the neutron.	33
1.8	Recent world data on the magnetic form factor of the neutron.	34
1.9	World data on the proton electric and magnetic form factor ratio $\frac{\mu G_E^p}{G_M^p}$ as a function of $Q^2$ .	35
1.10	Schematic diagram of the layout of the SAMPLE target and detector system.	37
1.11	Results from the 200 MeV SAMPLE data.	38
1.12	Schematic of the HAPPEX Experiment.	39
1.13	Schematic of the PVA4 experiment.	42
1.14	Results of the $G^0$ forward angle experiment.	44
1.15	World data on strange form factors at $Q^2 = 0.1 \text{ GeV}^2$ .	46
2.1	Schematic view of the $G^0$ Experiment showing the spectrometer in the forward angle configuration.	48

2.2	Floor plan of Hall C with the $G^0$ apparatus installed in the backward-angle mode. . . . .	49
2.3	The SMS cold mass and cryostat shell. . . . .	50
2.4	Schematic of the liquid hydrogen target, centered inside the liquid nitrogen shield of the superconducting magnet. . . . .	51
2.5	The target cell and manifold. . . . .	52
2.6	A French FPD octant. . . . .	55
2.7	The Focal Plane Detector. . . . .	56
2.8	The CED octant support structure. . . . .	57
2.9	The full eight-sectored $G^0$ backward angle setup. . . . .	58
2.10	The Cherenkov Detector. . . . .	61
2.11	North American electronics chain. . . . .	63
2.12	A Beam Cavity Monitor. . . . .	65
2.13	Diagram of a BPM. . . . .	66
2.14	The correlation plot between the measured and calculated beam positions at H00C. . . . .	67
2.15	A histogram of the residual between the measured and calculated beam positions at H00C. . . . .	68
2.16	Halo targets and halo installed in beamline. . . . .	69
2.17	Overhead schematic of halo monitors on the girder. . . . .	70
2.18	Side schematic of the halo monitors in the alcove. . . . .	70
2.19	Halo yields over the duration of the run. . . . .	71
2.20	Cross-section schematic of lumis in downstream beam pipe. . . . .	73
2.21	Side view schematic of lumis in downstream beam pipe . . . . .	73
2.22	The Hall C Moller Polarimeter. . . . .	77
2.23	Cross section through the MeV Mott polarimeter. . . . .	78

2.24	A coil modulation cycle . . . . .	82
3.1	A schematic of the CEBAF accelerator. . . . .	84
3.2	A schematic of the injector laser table. . . . .	85
3.3	Electromagnetic transitions in bulk and strained GaAs. . . . .	88
3.4	A Pockels Cell. . . . .	94
3.5	The orientation of the PC with respect to the polarization direction of the input light beam. . . . .	94
3.6	A Quadrant Photodiode. . . . .	95
3.7	Polarized source signal timing for $G^0$ . . . . .	97
3.8	Polarization ellipses for non-zero $\alpha$ and $\Delta$ phase shifts. . . . .	100
3.9	Illustration of a GaAs crystal being irradiated by light in which the residual linear polarization varies from a minimum at the left of the crystal to a maximum at the right of the crystal. . . . .	101
3.10	The effect of a linear gradient in the phase across the face of the laser beam on the spatial intensity profile of the electron beam. . . . .	102
3.11	Illustration of steering due to a Pockels Cell having lens-like properties when it is pulsed at high voltages. . . . .	103
3.12	The basic setup for using a rotatable half-wave plate to minimize charge asymmetry. . . . .	105
3.13	A RHWP scan. . . . .	106
3.14	A steering scan. . . . .	107
3.15	A phase gradient scan. . . . .	108
4.1	Cerenkov ADC versus FPD TDC of the the elastic locus on LH2. . .	115
4.2	Measured yield versus SMS current for two representative cells in the CED-FPD electron matrix. . . . .	118
4.3	CED-FPD matrix space cuts for hydrogen. . . . .	120

4.4	Measured yield versus SMS current for two representative cells in the CED-FPD pion matrix. . . . .	121
4.5	Normalized yield versus beam current. . . . .	125
4.6	Run-by-run fluctuations of the $x$ slopes determined using natural beam motion over the duration of the run for all eight octants. . . . .	133
4.7	Run-by-run fluctuations of the slopes of the six beam parameters determined using natural beam motion over the duration of the run for octant 1. . . . .	134
4.8	Average slope determined using natural beam motion versus average $\Phi$ of each octant before and after a crude deadtime correction. . . . .	137
4.9	Relationship between octant number and average $\Phi$ . . . . .	138
4.10	Average slope determined using coil modulation versus average $\Phi$ of each octant before and after a crude deadtime correction. . . . .	139
4.11	The raw (black) and corrected (blue) elastic electron locus yield vs beam parameters for octant 1 in run 29023 based on natural beam slopes determined for that run and applied to natural beam motion of that run. . . . .	140
4.12	A diagram showing the position and angle projection onto the target. . . . .	141
4.13	Average slope determined using natural beam motion versus octant for BPMs H00 and G0B and BPMs G0 and G0B. . . . .	143
4.14	The $x$ position of multiple BPMs subtracted from the $x$ position of BPM G0B mps by mps. . . . .	144
4.15	The $x$ slope versus run number for normal beam motion and coil modulation. . . . .	148
4.16	Yield for a typical octant versus mps showing the sometimes ineffectual beam trip cut. . . . .	149
4.17	Average slope versus average $\Phi$ of each octant for both natural beam motion and coil pulsing where the phase is fixed at zero. . . . .	151
4.18	Average slope of the last ten runs versus average $\Phi$ of each octant for both natural beam motion and coil pulsing and fitted to sine curves with phase being a free parameter. . . . .	153

4.19	Simulated average $x$ slope versus octant number at 687 MeV. . . . .	156
4.20	Simulated average $y$ slope versus octant number at 687 MeV. . . . .	157
5.1	Accumulated charge on target versus date. . . . .	163
5.2	The helicity-correlated differences/asymmetry of the six beam parameters versus slug number. . . . .	166
5.3	The average raw (blinded) asymmetry of the elastic electron locus versus slug number. . . . .	167
5.4	The average raw asymmetry of the elastic electron locus versus octant number. . . . .	168
5.5	A linear combination of strange form factors. . . . .	174
B.1	<i>CED Construction Step 2.</i> . . . . .	180
B.2	<i>CED Construction Step 3.</i> . . . . .	181
B.3	<i>CED Construction Step 4.</i> . . . . .	182
B.4	<i>CED Construction Step 5.</i> . . . . .	182
B.5	<i>CED Construction Step 6.</i> . . . . .	183
B.6	<i>CED Construction Step 7.</i> . . . . .	183

## ABSTRACT

The goal of Experiment E04-115 (the  $G^0$  backward angle measurement) at Jefferson Lab is to investigate the contributions of strange quarks to the fundamental properties of the nucleon. The experiment measures parity-violating asymmetries in elastic electron scattering off hydrogen and quasielastic electron scattering off deuterium at backward angles at  $Q^2 = 0.631 \text{ (GeV/c)}^2$  and  $Q^2 = 0.232 \text{ (GeV/c)}^2$ . The backward angle measurement represents the second phase of the  $G^0$  experiment. The first phase, Experiment E00-006 (the  $G^0$  forward angle experiment), measured parity-violating asymmetries in elastic electron scattering off hydrogen at forward angles over a  $Q^2$  range of 0.1-1.0  $\text{(GeV/c)}^2$ . The experiments used a polarized electron beam and unpolarized hydrogen and deuterium liquid targets. From these measurements, along with the electromagnetic form factors, one can extract the contribution of the strange quark to the proton's charge and magnetization distributions.

This thesis represents a first measurement of a parity-violating asymmetry in elastic electron scattering at  $Q^2 = 0.631 \text{ (GeV/c)}^2$  off hydrogen at backward angles. This work is based on data obtained during the first part of the run, beginning in March 2006 and ending in May 2006. During this period, a total of 15 C of beam charge was accumulated. The total accumulated charge represents about 15% of the 110 C which was proposed for this  $Q^2$ . The measured asymmetry is  $A = (-47.4 \pm 7.1 \pm 5.9 \pm 11.8)$  ppm, where the first uncertainty is due to statistics, the second uncertainty is systematic, and the third uncertainty is associated with the blinding factor. This result is consistent with a zero contribution from the strange quarks. The helicity-correlated beam properties and slopes are under adequate control for the final precision of the experiment.



# CHAPTER 1

## Theory

### 1.1 The Quark Model

Prior to the 1960s, physicists believed that protons, neutrons, and electrons were fundamental particles. In 1964, two physicists, Murray Gell-Mann and George Zweig, independently hit on the idea that the nucleon was a composite of even more elementary particles, called quarks. The nucleon is a collective name for the proton and neutron. The theory asserted that quarks come in three flavors, called up, down, and strange, with spin  $\frac{1}{2}\hbar$  and electric charges  $\frac{2}{3}e$ ,  $-\frac{1}{3}e$ , and  $-\frac{1}{3}e$ , respectively. Corresponding to each quark is an antiquark, a particle with the opposite sign of charge. According to this model, the proton is comprised of two up quarks and one down quark. Conversely, the neutron is comprised of one up quark and two down quarks. Composite particles made up of quarks are called hadrons.

Although Murray Gell-Mann conceived the idea of quarks, he did not think such fractionally charged entities could exist. He believed that quarks had to be “mathematical”, a convenient rubric for organizing the growing zoo of hadrons. In 1964, he wrote that “a search for stable quarks of charge  $-1/3$  or  $+2/3$  . . . at the

highest-energy accelerators would help to reassure us of the non-existence of real quarks” [1]. The first evidence that quarks were not just hypothetical mathematical identities but indeed the true building blocks of matter appeared in experiments at the Stanford Linear Accelerator Center (SLAC). These experiments were designed to measure electromagnetic structure functions of the proton and neutron and involved firing a high-energy beam of electrons at a target of liquid hydrogen. Much to the surprise of the experimenters, a large fraction of the electrons fired into protons ricocheted off at large angles, as if there were some small, hard center or centers within the proton. Bjorken and Richard Feynman proposed that the electrons might have bounced off tiny pits inside the protons, which Feynman dubbed “partons.” To check parton ideas against other explanations, more detailed measurements were made at SLAC over the next five years. In 1973, when results of the second-generation experiments were complete, everything seemed to be coming up quarks. The numbers suggested that matter in the proton is concentrated in much smaller particles, the quarks. It was especially appealing that quarks should be discovered using this technique as the nucleus of the atom was discovered in the same way, sixty years earlier.

There was a theoretical objection to the quark model, however. It violated the Pauli exclusion principle, which states that no two particles with half-integer spin can occupy the same state. For example, the  $\Delta^{++}$  baryon, which was supposed to consist of three identical up quarks in the same state, was inconsistent with the Pauli principle. In 1964, Oscar Greenberg proposed a solution that was later elaborated by Fritzsch, Gell-Mann and Heinrich Leutwyler. They suggested that quarks carry a new quantum number dubbed “color” and that colorless combinations of quarks are the only stable states. This idea provided the basis for Quantum chromodynamics (QCD), the currently accepted mathematical description of the strong interaction.

## 1.2 Quantum Chromodynamics

QCD is the theory of the strong interaction, the fundamental force that binds quarks together to form hadrons. QCD was constructed in analogy to quantum electrodynamics (QED), the quantum theory of the electromagnetic force. QED describes interactions of light with matter and those of charged particles with one another. It rests on the idea that charged particles interact by emitting and absorbing photons.

In QED, there are two values for electric charge, positive and negative. To explain the behavior of quarks in QCD, there are three different types of color charge called red, green, and blue. Each color can occur as color or anticolor. All observed particles are color-neutral objects. They are either leptons, particles with no color charges inside them, or hadrons. Hadrons occur in one of two ways. In baryons, the three quarks are each of a different color, and a combination of the three colors produces a particle that is neutral. In mesons, the anticolor of the antiquark neutralizes the color of the quark to produce a particle that is neutral.

In contrast to QED, where the photons exchanged are electrically neutral, the gluons of QCD carry color charge. Consequently, gluons interact directly with each other as well as with quarks. Gluons carry a mixture of a color and an anticolor of a different kind and can change one color charge into another. For example, if a blue quark absorbs a gluon and becomes red, then the gluon carried one unit of red charge and one unit of antiblue charge.

The strength of the electron-photon interaction is characterized by the fine-structure constant  $\alpha = \frac{1}{137}$ . The interaction of two charged particles occurs in a series of processes of increasing complexity. In the simplest case, only one virtual photon is exchanged. In a second-order process, two virtual photons are involved. There are an infinite number of processes and for each level of complexity, a factor of

$\frac{1}{137}$  decreases the contribution of the process. Thus, after a few levels the contribution is negligible. QCD is remarkably resistant to this approach. The strength of the interaction is parametrized by the strong coupling constant  $\alpha_s$ . The characteristic feature of the strong interaction is that the strong coupling constant decreases as the distance becomes smaller so that quarks are able to move freely within the hadrons. At distances an order of magnitude smaller than 1 fm (the radius of the proton), the strong coupling constant is effectively weak. In that limited regime, perturbation theory works. But for larger distances where confinement is the dominating process,  $\alpha_s$  is effectively large.

A virtual photon is created during an interaction between two real particles or during the decay of a real particle and is gone when the process is over. The distinction between a real photon and a virtual photon is in the 4-momentum transfer. A real photon has  $E = pc$  and  $Q^2 = \left(\frac{E^2}{c^2} - p^2\right) = 0$ . The energy of a virtual photon is not related to its momentum in the same way as for real photons. Instead, the energy of the virtual photon is determined by conservation of energy and momentum applied to the reaction.

### 1.3 Strange Quarks in the Nucleon

According to the Standard Model, there are a total of six quark flavors (up, down, strange, charm, top, and bottom) and eight species of gluons. The up and down quarks are the lightest quarks and have approximately the same mass. The strange quark is somewhat more massive than the up and down quarks. The charm, bottom and top quarks, in order of increasing mass, are significantly more massive than than the strange quark. Confinement of quarks implies that we cannot isolate them to measure their masses in a direct way. The masses must be implied indirectly from scattering experiments. As a result, quark mass makes sense only when one

Quark	Mass
up	1.5-3 MeV
down	3-7 MeV
strange	$95 \pm 25$ MeV
charm	$1.25 \pm 0.09$ GeV
bottom	$4.20 \pm 0.07$ GeV
top	$174.2 \pm 3.3$ GeV

TABLE 1.1: *Quark masses in the  $\overline{\text{MS}}$  scheme [2].*

specifies exactly the procedure used to define it. The bare quark masses are given in Table 1.1 and should be taken as indicative only.

In addition to the proton's three resident quarks, there is a sea of virtual quark antiquark pairs that constantly blink into and out of existence in the proton. These pairs originate from the gluon via the fundamental QCD vertex. These ghostly particles usually vanish in a tiny fraction of a second, but it's possible that they stay around long enough to influence the structure of the proton. At low energies, these pairs are expected to be made up predominantly of up, down and strange quarks. The heavier quarks are less likely to form since they are significantly more massive. The up and down quarks in the sea are difficult to distinguish from the valence up and down quarks. Thus, the strange quark provides a unique window on the sea and lends itself to study.

The  $G^0$  experiment seeks to determine the contribution of the strange quark to the charge and magnetic distributions within the nucleon. The motivation for this lies in experimental evidence that suggests that strange quarks contribute to other properties of the nucleon, including momentum, mass and spin. Section 1.3.1 discusses the strange quark contribution to the nucleon's momentum. The strange quark contributions to the nucleon's mass and spin are discussed in Sections 1.3.2 and 1.3.3, respectively.

### 1.3.1 Strange Quark Contribution to the Nucleon's Momentum

The strange-quark contribution to the nucleon's momentum is obtained by studying deep inelastic lepton scattering. Measurements of deep inelastic lepton scattering lead to a determination of the structure functions which describe aspects of the quark structure of the nucleon. Structure functions are dependent on the Bjorken scaling variable  $x = \frac{Q^2}{2M_N\nu}$ , where  $Q^2$  is the 4-momentum transfer squared,  $M_N$  is the nucleon mass, and  $\nu$  is the energy transfer measured in the rest frame of the target. The Bjorken scaling variable is dimensionless and is interpreted as the momentum fraction carried by the struck quark in the infinite momentum frame ( $q^2 \rightarrow \infty$  and  $\nu \rightarrow \infty$ ). The nucleon quark structure is described by the individual Parton Distribution Functions  $u(x)$ ,  $\bar{u}(x)$ ,  $d(x)$ ,  $\bar{d}(x)$ ,  $s(x)$ ,  $\bar{s}(x)$ , etc., where the bar indicates an antiquark. A quark structure function  $q(x)$  is the probability of finding quark flavor  $q$  carrying a fraction  $x$  of the nucleon momentum.

The flavor structure can be accessed by using charged-current neutrino and antineutrino interactions. Neutrinos are similar to the electron, with one crucial difference: neutrinos do not carry electric charge. The neutrino has half-integer spin and is therefore a fermion. Neutrino interactions can be reduced to two categories: Charged Current, when they weakly interact through the exchange of a  $W^\pm$  boson to form charged particles, and Neutral Current, when they produce uncharged particles through the weak exchange of  $Z^0$  particles. Neutrinos can interact with  $d$  and  $s$  quarks by raising their charge and producing a negative lepton. For example, the muon neutrino can interact with the down quark as described by  $\nu_\mu + d \rightarrow \mu^- + u$ . Similarly, the muon neutrino can interact with the strange quark as described by  $\nu_\mu + s \rightarrow \mu^- + c$ . The charmed quarks produced by the strange quarks can decay semileptonically yielding  $\mu^+s$ . Hence, in  $\nu_\mu$  interactions with strange quarks, one

observes  $\mu^- \mu^+$  pairs. Similarly, antineutrinos will produce  $\mu^+ \mu^-$  pairs from  $\bar{s}$  quarks. By this process, measurements of  $s(x)$  and  $\bar{s}(x)$  have been made. The results of these experiments are shown in Figure 1.1. They indicate that  $s(x)$  and  $\bar{s}(x)$  are significant at low  $x < 0.1$  and that  $s(x)$  and  $\bar{s}(x)$  each carry about 2% of the nucleon momentum.

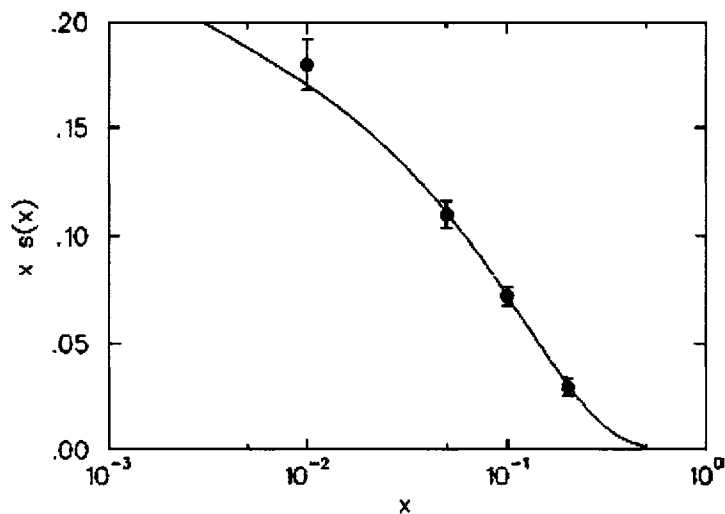


FIG. 1.1:

*Measured values of  $xs(x)$  versus  $x$  from deep inelastic neutrino scattering [3]. There is no significant difference between  $s(x)$  and  $\bar{s}(x)$  so this analysis assumed they were equal.*

### 1.3.2 Strange Quark Contributions to the Nucleon's Mass

The mass of the nucleon is given by the matrix element

$$M_N = \langle N | \mathcal{H} | N \rangle, \quad (1.1)$$

where  $\mathcal{H}$  is the QCD Hamiltonian of a nucleon, and  $|N\rangle$  is the initial and final state of the nucleon. The contribution of the up and down quarks to the mass of the

nucleon is given by

$$\hat{\sigma} = \hat{m} \langle N | \bar{u}u + \bar{d}d | N \rangle, \quad (1.2)$$

where  $\hat{m} = \frac{m_u + m_d}{2}$  is the average of the light quarks. Similarly, the contribution of the strange quark to the mass of the nucleon is given by the matrix element

$$\sigma_s = m_s \langle N | \bar{s}s | N \rangle, \quad (1.3)$$

where  $m_s$  is the mass of the strange quark. It follows that the strangeness content of the nucleon's mass is

$$y = \frac{2 \langle N | \bar{s}s | N \rangle}{\langle N | \bar{u}u + \bar{d}d | N \rangle}. \quad (1.4)$$

The strange quark term  $\sigma_s$  cannot at present be determined directly from either experiment or theory. However, two constraints on  $m_s$  arising from measurement are available. The first constraint is a result of hyperon mass splitting due to the SU(3) flavor symmetry breaking effect [4]

$$\frac{1}{3} (\hat{m} - m_s) \langle N | \bar{u}u + \bar{d}d - 2\bar{s}s | N \rangle = M_\Lambda - M_\Xi, \quad (1.5)$$

where  $M_\Lambda$  and  $M_\Xi$  are the masses of  $\Lambda$  and  $\Xi$  hyperons respectively. A hyperon is a baryon with non-zero strangeness. Strangeness  $S$  is a quantum number defined as the number of strange anti-quarks  $\bar{s}$  minus the number of strange quarks  $s$  in a particle. All hyperons have half-integer spin and are composed of three quarks, at least one of which is a strange quark. The  $\Lambda$  hyperon is composed of an up, down and strange quark while a  $\Xi$  hyperon is composed of a down and two strange quarks.

Substituting Equation 1.4 into Equation 1.5 yields

$$\frac{1}{3} \left(1 - \frac{m_s}{\hat{m}}\right) (1 - y) \hat{\sigma} = M_\Lambda - M_\Xi. \quad (1.6)$$

Taking the canonical ratio that  $m_s/\hat{m} \sim 26$  [5] and assuming the strange matrix element is zero ( $y = 0$ ) gives  $\hat{\sigma} \sim 25$  MeV. After accounting for higher order corrections,  $\hat{\sigma} \sim 35$  MeV [6].



A second constraint comes from the  $\pi - N$  “sigma term”,  $\Sigma_{\pi N}$ , at the Cheng- Daschen point. The Cheng-Daschen point is unphysical ( $s = M_N^2, t = m_\pi^2$ ) so it is necessary to extrapolate it to  $t = 0$  using dispersion relations. According to these calculations,  $\hat{\sigma} \sim 45$  MeV [6]. If the strange quark does not contribute to the scalar matrix element ( $y = 0$ ), then  $\hat{\sigma}$  as obtained via the two approaches should agree. The discrepancy between 35 and 45 MeV implies a 20% strange sea quark content ( $y \sim 0.2$ ) in the proton. The uncertainty of this result is large due to a number of factors: experimental uncertainties of the  $\pi - N$  data, the extrapolation of the data to the physical region, and the uncertainty in the quark mass ratio  $m_s/\hat{m}$ .

### 1.3.3 Strange Quark Contributions to the Nucleon’s Spin

The strange-quark contribution to the nucleon spin is obtained by studying spin-dependent deep inelastic lepton scattering. The inclusive scattering of a charged lepton from a nucleon is described by four structure functions:  $F_1$ ,  $F_2$ ,  $g_1$ , and  $g_2$ . The  $g_1(x)$  structure function is the vector sum of the quark polarizations, weighted by the charge of that flavor quark

$$g_1(x) = \frac{1}{2} \sum e_q \Delta q(x), \quad (1.7)$$

where

$$\Delta q(x) = [q^+(x) - q^-(x) + \bar{q}^+(x) - \bar{q}^-(x)]. \quad (1.8)$$

The superscript  $+(-)$  corresponds to the spin of the quark being aligned (anti-aligned) with the spin of the nucleon. The total spin carried by the quarks is the first moment of the  $g_1(x)$  structure function

$$\Gamma_1 \equiv \int_0^1 g_1(x) dx. \quad (1.9)$$

Ignoring the heavy quarks, the proton first moment is

$$\Gamma_1^p = \frac{1}{2} \left( \frac{4}{9} \Delta u + \frac{1}{9} \Delta d + \frac{1}{9} \Delta s \right), \quad (1.10)$$

where  $\Delta q$  is now the integral of  $\Delta q$ . Combining this information with the isovector axial matrix element (known from neutron beta decay [2])

$$G_A(Q^2 = 0) = \Delta u - \Delta d = 1.2601 \pm 0.0025, \quad (1.11)$$

and the octet combination (known from hyperon beta decay [8])

$$a_8 = (\Delta u + \Delta d - 2\Delta s) = -0.60 \pm 0.12, \quad (1.12)$$

yields values for the individual quark flavor components  $\Delta u$ ,  $\Delta d$ , and  $\Delta s$ . In neutron beta decay, the weak interaction converts a neutron into a proton while emitting an electron and an anti-neutrino  $n^0 \rightarrow p^+ + e^- + \bar{\nu}_e$ . At the fundamental level, this is due to the conversion of a down quark to an up quark by emission of a W boson. Hyperon beta decay is an SU(3) symmetry reflection of the neutron beta decay (e.g. a quark transition of  $uss$  to  $uus$  instead of  $udd$  to  $uud$ ).

According to a recent result [9, 10], the fraction of the nucleon spin carried by quark spins is

$$\Delta u + \Delta d + \Delta s = 0.20 \pm 0.10. \quad (1.13)$$

In other words, 20% of the nucleon's spin is carried by the quark spins. The remaining 80% is expected to come from the orbital angular momenta of the quarks, as well as the spins and orbital angular momenta of the gluons.

According to recent analyses [9, 10], the contribution of strange quarks to the nucleon's spin is given

$$\Delta s \simeq -0.1 \pm 0.1. \quad (1.14)$$

Although this number is small, the central value is significant compared to the total spin carried by the quark spins. Regardless, there is high uncertainty associated with this number. Concerns about SU(3) breaking, extrapolation of the data to  $x = 0$  to form the integral in Equation 1.10, and uncertainties in the  $Q^2$  evolution of the structure functions all contribute to reduced confidence.

Additional information on the spin alignment of the quarks with respect to the nucleon spin comes from results obtained from the HERMES experiment at DESY's HERA electron-proton collider in Hamburg, Germany. The HERMES spectrometer detects electrons scattered from a polarized nucleon target and determines the energy and the angle through which the electrons are deflected. By comparing the distribution of scattered electrons for different polarization states of the beam and the target, information about the spin of the proton can be deduced. During its first run, HERMES provided the first separate determinations of the polarizations of the up, down and strange sea quarks. The data reveal that while the spins of the up valence quarks point in the same direction as the overall nucleon spin, the down valence quarks carry a spin pointing in the opposite direction. The polarizations of the sea quarks are all consistent with zero [11]. Figure 1.2 shows the spin alignment of the strange quark as a function of Bjorken  $x$ .

## 1.4 Electromagnetic Interaction

We have discussed the strange quark contribution to several experimental observables. To determine the contribution of the strange quark to the charge and magnetic distributions within the nucleon, it is necessary to develop some formalism. The lowest-order amplitude for electron-nucleon scattering via the electromagnetic

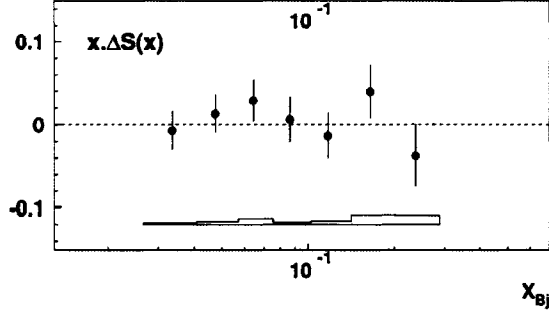


FIG. 1.2:

The spin alignment of the strange quarks at  $\langle Q^2 \rangle = 2.5 \text{ GeV}^2$ , as a function of Bjorken  $x$ . The error bars are statistical and the error bands are systematic [11].

interaction is given by

$$\mathcal{M}_\gamma = -\frac{4\pi\alpha}{q^2} J_e^\mu J_\mu^p, \quad (1.15)$$

where  $J_e^\mu$  is the electron transition current

$$J_e^\mu = \bar{u}\gamma^\mu u. \quad (1.16)$$

The terms  $u$  and  $u'$  are the Dirac 4-component spinors that describe the initial and final electron, respectively, and  $\gamma^\mu$  is the Dirac gamma matrix. The proton, being an extended spin-1/2 particle, yields a more complex transition current

$$J_\mu^p = \bar{u}(p') \left[ F_{1,p}^\gamma(q^2) \gamma^\mu + \frac{\kappa}{2M_p} F_{2,p}^\gamma(q^2) i\sigma^{\mu\nu} q_\nu \right] u(p), \quad (1.17)$$

where  $p$  and  $p'$  are the initial and final 4-momenta of the proton,  $M_p$  is the mass of the proton,  $\sigma^{\mu\nu} = \frac{i}{2} [\gamma^\mu, \gamma^\nu]$ , and  $\kappa$  is the anomalous magnetic moment. The anomalous magnetic moment is the difference between the observed gyromagnetic ratio of the electron and the value of exactly two predicted by Dirac's theory of the electron.  $F_{1,p}^\gamma(q^2)$  and  $F_{2,p}^\gamma(q^2)$  are the proton Dirac and Pauli electromagnetic form factors, respectively, which are functions of the squared momentum transfer. We also use the Sachs form factors, which are linear combinations of the Dirac and

Pauli form factors

$$G_E^p = F_{1,p}^\gamma - \frac{\kappa q^2}{4M_p^2} F_{2,p}^\gamma \quad (1.18)$$

$$G_M^p = F_{1,p}^\gamma + \kappa F_{2,p}^\gamma. \quad (1.19)$$

$G_E^p$  is the proton electric form factor and  $G_M^p$  is the proton magnetic form factor. In contrast to the Dirac and Pauli form factors, the Sachs' form factors have physical interpretations. In electron scattering, it is common practice to use the inverse of the four-momentum transfer squared  $Q^2 = -q^2 \geq 0$ . In the limit  $Q^2 = 0$ , we have

$$G_E^p(Q^2 = 0) = 1 \quad G_E^n(Q^2 = 0) = 0 \quad (1.20)$$

$$G_M^p(Q^2 = 0) = \mu_p \quad G_M^n(Q^2 = 0) = \mu_n, \quad (1.21)$$

where  $\mu_p$  is the proton's magnetic moment and  $\mu_n$  is the neutron's magnetic moment. The electric and magnetic form factors are the Fourier transforms of the charge and magnetization radial distributions  $\rho_{chg}(r)$  and  $\rho_{mag}(r)$ , respectively, of the nucleon in the Breit frame. The Breit (or "brick wall") frame is a special Lorentz frame in which there is no transfer of energy. In the case of elastic electron-nucleon scattering, the Breit frame is the center-of-mass frame of the electron-nucleon system.

In the non-relativistic limit, the nucleon electric form factor is related to the root-mean-square (rms) charge radius of the nucleon

$$\left. \frac{dG_E(Q^2)}{dQ^2} \right|_{Q^2=0} = -\frac{\langle r^2 \rangle}{6}, \quad (1.22)$$

with the condition that  $G_E(Q^2 = 0) = 1$  for the proton and 0 for the neutron. The nucleon magnetic form factor is related to the root-mean-square (rms) magnetic radius of the nucleon

$$\left. \frac{dG_M(Q^2)}{dQ^2} \right|_{Q^2=0} = -\mu_N \frac{\langle r^2 \rangle}{6}. \quad (1.23)$$

## 1.5 Weak Neutral Interaction

The amplitude for electron-proton scattering via the weak neutral interaction is given by

$$\mathcal{M}_z = \frac{G_F}{\sqrt{2}} J_e^{Z\mu} J_\mu^{Zp}, \quad (1.24)$$

where  $G_F$  is the charged weak coupling constant

$$G_F = \frac{e^2}{4\sqrt{2}M_W^2 \sin^2 \theta_W}, \quad (1.25)$$

$M_W$  is the  $W$  boson mass, and  $\theta_W$  is the weak mixing angle. The weak mixing angle is related to the neutral (Z) and charged (W) boson masses by the relation

$$\cos \theta_W = \frac{M_W}{M_Z}. \quad (1.26)$$

The neutral current for the proton is

$$J_\mu^{Zp} = \bar{u} \left[ \gamma_\mu F_1^Z + i \frac{\sigma_{\mu\nu} q^\nu}{2M_p} F_2^Z + \gamma_\mu \gamma_5 G_A^Z \right] u, \quad (1.27)$$

where  $G_A^Z$  is the weak axial form factor, and  $F_1^Z$  and  $F_2^Z$  are the weak neutral form factors and are analogous to the electromagnetic form factors  $F_1^\gamma$  and  $F_2^\gamma$  and can be similarly combined to give  $G_E^Z$  and  $G_M^Z$ . The neutral current for the electron is

$$J_e^{Z\mu} = \bar{u} \frac{1}{2} (g_V \gamma^\mu - g_A \gamma^\mu \gamma_5) u, \quad (1.28)$$

where the weak axial charges  $g_A$  and weak vector charges  $g_V$  for the individual quark flavors are given in Table 1.2.

## 1.6 Weak Axial Form Factors

The weak axial form factors can be expressed as a sum of the individual quark flavor form factors, weighted by the weak axial charge of that flavor quark

$$G_A^{Z,p} = g_A^u G_A^{u,p} + g_A^d G_A^{d,p} + g_A^s G_A^{s,p} \quad (1.29)$$

	$q^\gamma$	$g_V$	$g_A$
$e$	$-1$	$-1(1 - 4\sin^2\theta_W)$	$+1$
$u$	$\frac{2}{3}$	$1 - \frac{8}{3}\sin^2\theta_W$	$-1$
$d$	$-\frac{1}{3}$	$-1 + \frac{4}{3}\sin^2\theta_W$	$+1$
$s$	$-\frac{1}{3}$	$-1 + \frac{8}{3}\sin^2\theta_W$	$+1$

TABLE 1.2: *Electroweak couplings of charged fundamental particles.*

$$G_A^{Z,n} = g_A^u G_A^{u,n} + g_A^d G_A^{d,n} + g_A^s G_A^{s,n}. \quad (1.30)$$

The weak axial form factors can also be expressed as a sum of an isovector  $G_A^{T=1}$ , isoscalar  $G_A^8$ , and strange  $G_A^s$  components

$$G_A^{Z,p} = Q_A^{T=1,p} G_A^{T=1,p} + Q_A^{T=0,p} G_A^{(8),p} + Q_A^{0,p} G_A^{s,p}, \quad (1.31)$$

where

$$G_A^{T=1,p} = G_A^{u,p} - G_A^{d,p}, \quad (1.32)$$

and

$$G_A^{(8),p} = \frac{1}{2\sqrt{3}} \left( G_A^{u,p} + G_A^{d,p} - 2G_A^{s,p} \right). \quad (1.33)$$

The isovector, isoscalar, and strange components in Equation 1.31 are weighted by linear combinations of the axial charges

$$\begin{aligned} Q_A^{T=1,p} &= \frac{1}{2} \left( g_A^{u,p} - g_A^{d,p} \right) \\ Q_A^{T=0,p} &= \sqrt{3} \left( g_A^{u,p} + g_A^{d,p} \right) \\ Q_A^{(0),p} &= g_A^{u,p} + g_A^{d,p} + g_A^{s,p}. \end{aligned} \quad (1.34)$$

## 1.7 Vector Form Factors

Analogous to the weak axial form factor, the charge and magnetization form factors of the nucleon associated with  $\gamma$  exchange can be expressed in terms of

quark-flavor dependent form factors as

$$G_{E,M}^{\gamma,p} = \frac{2}{3}G_{E,M}^{u,p} - \frac{1}{3}G_{E,M}^{d,p} - \frac{1}{3}G_{E,M}^{s,p} \quad (1.35)$$

$$G_{E,M}^{\gamma,n} = \frac{2}{3}G_{E,M}^{u,n} - \frac{1}{3}G_{E,M}^{d,n} - \frac{1}{3}G_{E,M}^{s,n}. \quad (1.36)$$

These are a sum of the individual quark flavor form factors, weighted by the electromagnetic charge of that flavor quark. Here, we assume that the charm, bottom, and top quark contributions are negligible. Similarly, the neutral weak form factors can be expressed as a sum of the individual quark flavor form factors. In this case, the form factors are weighted by the weak vector charge of that flavor quark

$$G_{E,M}^{Z,p} = g_V^u G_{E,M}^{u,p} + g_V^d G_{E,M}^{d,p} + g_V^s G_{E,M}^{s,p} \quad (1.37)$$

$$G_{E,M}^{Z,n} = g_V^u G_{E,M}^{u,n} + g_V^d G_{E,M}^{d,n} + g_V^s G_{E,M}^{s,n}. \quad (1.38)$$

If we assume charge symmetry, then interchanging up and down quarks will transform a neutron into a proton and vice versa. In this language,

$$G_{E,M}^{u,n} = G_{E,M}^{d,p}, \quad (1.39)$$

$$G_{E,M}^{d,n} = G_{E,M}^{u,p}, \quad (1.40)$$

$$G_{E,M}^{s,p} = G_{E,M}^{s,n} \equiv G_{E,M}^s. \quad (1.41)$$

Making the above substitutions, Equation 1.36 becomes

$$G_{E,M}^{\gamma,n} = \frac{2}{3}G_{E,M}^{d,p} - \frac{1}{3}G_{E,M}^{u,p} - \frac{1}{3}G_{E,M}^s, \quad (1.42)$$

and Equation 1.37 can be written

$$G_{E,M}^{Z,p} = g_V^u G_{E,M}^{u,p} + g_V^d G_{E,M}^{d,p} + g_V^s G_{E,M}^s. \quad (1.43)$$



Equations 1.35 and 1.42 can be combined to eliminate  $G_{E,M}^{u,p}$ , yielding

$$G_{E,M}^{d,p} = 2G_{E,M}^{\gamma,n} + G_{E,M}^s + G_{E,M}^{\gamma,p}. \quad (1.44)$$

Similarly, Equations 1.35 and 1.42 can be combined to eliminate  $G_{E,M}^{d,p}$ , yielding

$$G_{E,M}^{u,p} = G_{E,M}^{\gamma,n} + G_{E,M}^s + 2G_{E,M}^{\gamma,p}. \quad (1.45)$$

Substituting Equations 1.44 and 1.45 into Equation 1.43 gives

$$G_{E,M}^{Z,p} = \xi_V^p G_{E,M}^{\gamma,p} + \xi_V^n G_{E,M}^{\gamma,n} + \xi_V^{(0)} G_{E,M}^s, \quad (1.46)$$

where

$$\begin{aligned} \xi_V^p &= 2g_V^n + g_V^d \\ \xi_V^n &= 2g_V^d + g_V^u \\ \xi_V^{(0)} &= g_V^u + g_V^d + g_V^s. \end{aligned} \quad (1.47)$$

Proceeding in the same way for the neutron, one gets

$$G_{E,M}^{Z,n} = \xi_V^n G_{E,M}^{\gamma,p} + \xi_V^p G_{E,M}^{\gamma,n} + \xi_V^{(0)} G_{E,M}^s. \quad (1.48)$$

Equations 1.46 and 1.48 are key results. They show how the neutral weak form factors are related to the electromagnetic form factors plus a contribution from the strange form factor. Thus measurement of the neutral weak form factor will allow (after combination with the electromagnetic form factors determined from other experiments) determination of the strange form factor of interest.

The physical interpretation of the Fourier transform  $G_E^s(Q^2)$  of the strange charge distribution  $\rho_s(r)$  in the proton is the amount of variation in  $\rho_s(r)$ . The strange charge distribution  $\rho_s(r)$  is the average difference in radial distance to the center of the proton between strange and anti-strange quarks. It is plausible that the strange charge distribution is non-zero. For example, in a simple model, the

proton can fluctuate into a neutron  $n$  and a positive pion  $\pi^+$ . Similarly, the proton can fluctuate into a positive kaon  $k^+$  and a neutral lambda  $\Lambda^0$ . The  $k^+$  is a meson composed of an up quark and an anti-strange quark while the  $\Lambda^0$  is a baryon composed of an up quark, down quark, and strange quark. Since the rest mass of the  $\Lambda^0$  is about three times more massive than the rest mass of the  $k^+$ , the proton's center of mass is closer to the  $\Lambda^0$  than the  $k^+$ . In this simple model, one might expect that the radial distance of the strange quark to the center of the proton is smaller than the radial distance of the anti-strange quark to the center of the proton.

As an aside, the  $G^0$  form factor (which gave the present experiment its name) can be defined as the difference between the electric form factor of the proton associated with the electromagnetic interaction and the electric neutral weak form factor

$$G_E^{0,p} = (2 - 4 \sin^2 \theta_w) G_E^{p,\gamma} - 4G_E^{p,Z}. \quad (1.49)$$

It is also the average of the up, down, and strange quark distributions with the proton (i.e. it is the SU(3) singlet form factor)

$$G_E^{0,p} = \frac{1}{3} \left( G_E^{u,p} + G_E^{d,p} + G_E^{s,p} \right). \quad (1.50)$$

$G_M^{0,p}$  can be similarly defined.

## 1.8 Energy-Momentum 4-vector Transfer Squared

Up to this point, multiple references to the energy-momentum 4-vector transfer squared have been made. This section defines the energy-momentum 4-vector transfer squared. Consider the elastic collision

$$a + b \rightarrow c + d, \quad (1.51)$$

where  $a$  is the electron projectile,  $b$  is the stationary target proton,  $c$  is the scattered electron and  $d$  is the scattered proton. The energy-momentum 4-vectors are

$$\begin{aligned}
 p_a^\mu &= (E_a, \vec{p}_a) \\
 p_b^\mu &= (E_b, \vec{p}_b) \\
 p_c^\mu &= (E_c, \vec{p}_c) \\
 p_d^\mu &= (E_d, \vec{p}_d).
 \end{aligned} \tag{1.52}$$

According to the conservation of energy and momentum,

$$p_a^\mu - p_c^\mu = p_d^\mu - p_b^\mu \tag{1.53}$$

and

$$E_a - E_c = E_d - E_b. \tag{1.54}$$

For an elastic scattering process, the energy-momentum 4-vector transfer squared between the incident and emergent electron is invariant, with a value of

$$\begin{aligned}
 Q^2 &= (\vec{p}_c - \vec{p}_a)^2 - (E_c - E_a)^2 \\
 &= (p_c^2 - E_c^2) + (p_a^2 - E_a^2) - 2\vec{p}_c\vec{p}_a + 2E_cE_a \\
 &= -2m^2 - 2p_cp_a \cos \theta + 2E_cE_a \\
 &\simeq 2E_cE_a (1 - \cos \theta) \\
 &\simeq 4E_cE_a \sin^2 \theta/2,
 \end{aligned} \tag{1.55}$$

where  $\theta$  is the angle between the initial and final momentum in the lab frame and we make the approximation that  $m \ll p$ .

We can also express the energy-momentum 4-vector transfer squared in terms of the stationary target proton and scattered proton. To indicate the energy-momentum 4-vector transfer in the process, we define  $q^\mu = (\omega, \vec{q})$ , where

$$\omega = E_d - E_b = E_d - m_b^2 \tag{1.56}$$

and

$$\mathbf{q} = \vec{p}_d - \vec{p}_b. \quad (1.57)$$

Taking the square of Equation 1.57 gives

$$q^2 = p_d^2 = E_d^2 - m_d^2 \quad (1.58)$$

since  $b$  is stationary and has zero momentum. Solving Equation 1.58 for  $E_d$  yields

$$E_d = \sqrt{q^2 + m_d^2}. \quad (1.59)$$

Substituting Equation 1.59 into Equation 1.56 gives

$$\omega = \sqrt{q^2 + m_d^2} - m_b. \quad (1.60)$$

Solving Equation 1.60 for  $Q^2 \equiv q^2 - \omega^2$  yields

$$Q^2 = 2m_b\omega. \quad (1.61)$$

## 1.9 Elastic Parity-Violating Electron Neutron Scattering

### 1.9.1 Parity-Violating Asymmetry

Elastic scattering of an electron,  $e$ , from a nucleon,  $N$ , is described to lowest order by the Feynman diagrams in Figure 1.3. The scattering is described by the interference of two interactions, electromagnetic and neutral weak. The electromagnetic interaction is mediated by a photon,  $\gamma$ , while the neutral weak interaction is mediated by a neutral weak vector boson,  $Z^0$ .

The weak force, being a mixed vector and axial-vector interaction, does not conserve parity. The difference between axial vectors and vectors is the effect of an

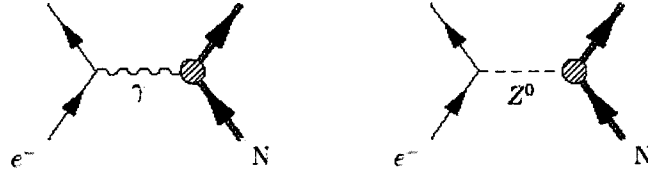


FIG. 1.3: An electron  $e$  scatters from a nucleon  $N$ , exchanging a virtual photon  $\gamma$ , left, and a neutral weak boson  $Z^0$ , right.

inversion of the coordinate system (parity transformation) on their coordinates; i.e.,

$$x \rightarrow -x \quad (1.62)$$

$$y \rightarrow -y \quad (1.63)$$

$$z \rightarrow -z. \quad (1.64)$$

Under this inversion, an ordinary vector  $V$  is transformed into its negative, whereas the coordinates of an axial vector  $A$  are unchanged by the inversion; i.e.,

$$V \rightarrow -V \quad (1.65)$$

$$A \rightarrow A. \quad (1.66)$$

In other words, an axial vector behaves like a vector except that it is invariant under the inversion of its coordinate axes.

A parity transformation produces the same effect as looking into a mirror. It reverses the travel direction of a spinning object approaching the mirror without reversing the direction of rotation. For example, a right-handed object will produce a mirror-image counterpart that is left-handed. By definition, a right-handed particle is one that rotates in the direction of the fingers of the right hand while traveling in the direction of the thumb. Similarly, a left-handed particle rotates in the opposite direction. According to parity conservation, left- and right-handed particles have identical interaction rates.

To be parity-violating, the  $Z^0$  exchange must involve either  $V(e) \times A(N)$  or  $A(e) \times V(N)$  coupling, where  $V$  represents weak vector coupling and  $A$  represents weak axial coupling. The weak vector coupling of the electron is suppressed because  $1 - 4 \sin^2 \theta_W \simeq 0.074 \ll 1$  (see Table 1.2). Consequently, parity-violating electron scattering is most sensitive to the case where the weak axial coupling is to the electron and the weak hadronic interaction is vector in character.

The scattering amplitude of an electron-proton interaction, associated with Figure 1.3 is

$$\mathcal{M} = \mathcal{M}_\gamma + \mathcal{M}_Z, \quad (1.67)$$

where  $\mathcal{M}_\gamma$  is the electromagnetic interaction amplitude and  $\mathcal{M}_Z$  is the weak interaction amplitude. The term  $\mathcal{M}_Z$  is often neglected since it is roughly  $10^5$  times smaller than  $\mathcal{M}_\gamma$  at  $Q^2 \simeq 1 \text{ GeV}^2$ . The cross section is proportional to the square of the scattering amplitude

$$\begin{aligned} |\mathcal{M}|^2 &= |\mathcal{M}_\gamma + \mathcal{M}_Z|^2 \\ &= (\mathcal{M}_\gamma^R + i\mathcal{M}_\gamma^C + \mathcal{M}_Z^R + i\mathcal{M}_Z^C) (\mathcal{M}_\gamma^R - i\mathcal{M}_\gamma^C + \mathcal{M}_Z^R - i\mathcal{M}_Z^C) \\ &= |\mathcal{M}_\gamma|^2 + |\mathcal{M}_Z|^2 + 2\mathcal{M}_\gamma^R \mathcal{M}_Z^R + 2\mathcal{M}_\gamma^C \mathcal{M}_Z^C \\ &= |\mathcal{M}_\gamma|^2 + |\mathcal{M}_Z|^2 + 2\text{Re} (\mathcal{M}_\gamma^R - i\mathcal{M}_\gamma^C) (\mathcal{M}_Z^R - i\mathcal{M}_Z^C) \\ &= |\mathcal{M}_\gamma|^2 + |\mathcal{M}_Z|^2 + 2\text{Re} [(\mathcal{M}_\gamma^*) (\mathcal{M}_Z)] \\ &= |\mathcal{M}_\gamma|^2 + |\mathcal{M}_Z|^2 + 2\text{Re} [(\mathcal{M}_\gamma) (\mathcal{M}_Z^*)]. \end{aligned} \quad (1.68)$$

Similarly, the term  $|\mathcal{M}_Z|^2$  is negligible. The electromagnetic interaction conserves parity and hence its scattering amplitude  $\mathcal{M}_\gamma$  is a vector interaction. Since the weak interaction violates parity, its scattering amplitude  $\mathcal{M}_Z$  has both vector and axial-vector pieces. It is proportional to the difference between a vector and an axial vector,  $V - A$ . The cross term in Equation 1.68 is therefore a sum of a vector-vector cross-product and a vector-axial-vector cross-product. The cross-product of two

vectors is an axial-vector while the cross-product of a vector and an axial-vector is a vector. So the cross term is proportional to the difference between a vector and an axial-vector. In the mirror experiment, the vector in the cross term will change signs but the axial-vector will not. Therefore, because the weak interaction violates parity, the cross term in Equation 1.68 will be different in the mirror experiment. In parity-violating electron scattering, the mirror measurement is made by reversing the beam helicity. The cross term can be determined experimentally by comparing the cross sections of the polarized electron beam with positive and negative helicities. An asymmetry,  $A$ , can be formed by taking the difference over the sum of the helicity dependent scattering cross sections

$$A = \frac{\sigma_R - \sigma_L}{\sigma_R + \sigma_L}, \quad (1.69)$$

where  $\sigma_R$  and  $\sigma_L$  are the right-handed and left-handed helicity dependent scattering cross sections, respectively. In terms of scattering amplitudes, the asymmetry can be written as

$$A = \frac{|\mathcal{M}_\gamma + \mathcal{M}_z|_R^2 - |\mathcal{M}_\gamma + \mathcal{M}_z|_L^2}{|\mathcal{M}_\gamma + \mathcal{M}_z|_R^2 + |\mathcal{M}_\gamma + \mathcal{M}_z|_L^2} \simeq 2 \frac{\mathcal{M}_\gamma^* \mathcal{M}_z}{|\mathcal{M}_\gamma|^2}. \quad (1.70)$$

Substituting Equations 1.15 and 1.24 in Equation 1.70 yields

$$A = \left( \frac{-G_F Q^2}{4\sqrt{2}\pi\alpha} \right) \frac{\epsilon G_E^{\gamma,x} G_E^{Z,x} + \tau G_M^{\gamma,x} G_M^{Z,x} - \frac{1}{2}(1 - 4\sin^2\theta_W) \epsilon' G_M^{\gamma,x} G_A^{Z,x}}{\epsilon (G_E^{\gamma,x})^2 + (G_M^{\gamma,x})^2}, \quad (1.71)$$

where  $\epsilon$  is the longitudinal polarization of the virtual photon

$$\epsilon = \frac{1}{1 + 2(1 + \tau)\tan^2\frac{\theta}{2}}, \quad (1.72)$$

$$\epsilon' = \sqrt{\tau(1 + \tau)(1 - \epsilon^2)}, \quad (1.73)$$

$$\tau = \frac{Q^2}{4M_N^2}, \quad (1.74)$$

$x = p, n$  represents a proton  $p$  or a neutron  $n$ , and  $\theta$  is the laboratory electron scattering angle. Equation 1.71 can be written in a more compact form

$$A = A_0 \frac{A_E + A_M + A_A}{D}, \quad (1.75)$$

where

$$A_0 = -\frac{G_F Q^2}{4\pi\alpha\sqrt{2}} \quad (1.76)$$

$$A_E = \epsilon G_E^{\gamma,x} G_E^{Z,x} \quad (1.77)$$

$$A_M = \tau G_M^{\gamma,x} G_M^{Z,x} \quad (1.78)$$

$$A_A = -\frac{1}{2} (1 - 4 \sin^2 \theta_W) \epsilon' G_M^{\gamma,x} G_A^{Z,x} \quad (1.79)$$

$$D = \epsilon G_E^{\gamma,x^2} + \tau G_M^{\gamma,x^2}. \quad (1.80)$$

The term  $A_0$  gives the scale of the asymmetry. The quantities  $A_E$ ,  $A_M$ , and  $A_A$  are terms that contain cross products of electromagnetic and weak form factors of the proton.

Three independent measurements are needed for a complete determination of the three weak form factors  $G_E^{Z,x}$ ,  $G_M^{Z,x}$ , and  $G_A^{Z,x}$  at a given  $Q^2$ . This can be achieved by varying the kinematical variables  $\epsilon$  and  $\epsilon'$  at a fixed  $Q^2$ . In very forward scattering,  $\theta \rightarrow 0$ . Consequently,  $\epsilon \rightarrow 1$  and  $\epsilon' \rightarrow 0$ . The asymmetry is sensitive to the combination  $A_E + A_M$ . The axial contribution is suppressed. In very backward scattering,  $\theta \rightarrow \pi$ . Consequently,  $\epsilon \rightarrow 0$  and  $\epsilon' \rightarrow \sqrt{\tau(1+\tau)}$ . The asymmetry is sensitive to the combination  $A_M + A_A$ . The electric contribution is suppressed. Alternately, the use of targets with different  $Z$  can allow a means to separate the form factors.



### 1.9.2 Higher Order Effects

The parity-violating asymmetry in Equation 1.71 corresponds to the lowest order (tree level) contribution in perturbation theory. The evaluation of higher order corrections is called the radiative correction. The radiative correction of the parity-violating asymmetry is composed of three contributions: heavy quark contributions, one-quark and multiple-quark electroweak radiative corrections.

Heavy quark contributions refer to contributions of the charm, bottom, and top quarks. This contribution is less than  $10^{-2}$  [12] and is therefore neglected.

One-quark corrections refer to higher-order corrections to the scattering in which only a single quark is involved. Two representative higher-order one-quark diagrams are shown in Figure 1.4. Figure 1.4(a) is the  $\gamma - Z^0$  mixing diagram in which a  $Z^0$  and  $\gamma$  couple to a  $q\bar{q}$  loop. Figure 1.4(b) is the  $\gamma - Z^0$  box diagram.

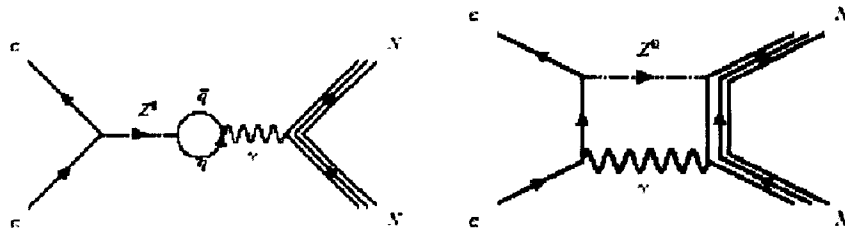


FIG. 1.4:

*Higher-order one-quark diagrams. (a) is the  $\gamma - Z^0$  mixing diagram in which a  $Z^0$  and  $\gamma$  couple to a  $q\bar{q}$  loop. (b) is the  $\gamma - Z^0$  box diagram.*

The multiple-quark or “anapole” correction involves an exchange of a photon with multiple quarks inside a nucleon interacting weakly. This produces an additional parity-violating term called the “anapole moment”. Two representative processes are shown in Figure 1.5.

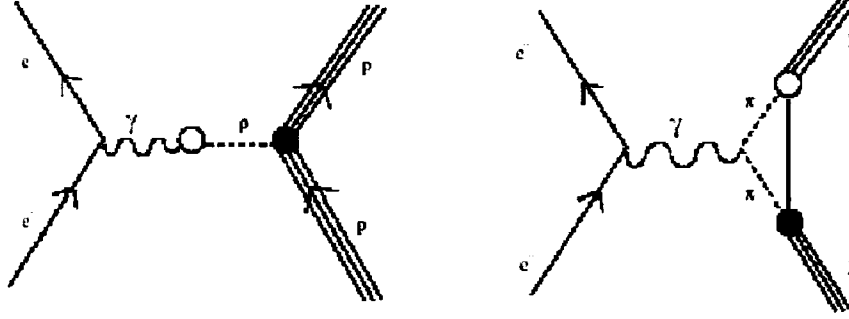


FIG. 1.5:

*Higher-order multiple-quark diagrams.*

### One-quark Correction

Using Equation 1.46 in Equation 1.71, the electron-proton parity-violating asymmetry becomes

$$\begin{aligned}
 A(\vec{e}p) = & - \frac{G_F Q^2}{4\sqrt{2}\pi\alpha} \left( \xi_V^p + \xi_V^n \frac{\epsilon G_E^{\gamma,p} G_E^{\gamma,n} + \tau G_M^{\gamma,p} G_M^{\gamma,n}}{\epsilon (G_E^{\gamma,p})^2 + \tau (G_M^{\gamma,p})^2} \right) \\
 & - \frac{G_F Q^2}{4\sqrt{2}\pi\alpha} \xi_V^{(0)} \frac{\epsilon G_E^{\gamma,p}}{\epsilon (G_E^{\gamma,p})^2 + \tau (G_M^{\gamma,p})^2} G_E^{\gamma,s} \\
 & - \frac{G_F Q^2}{4\sqrt{2}\pi\alpha} \xi_V^{(0)} \frac{\tau G_M^{\gamma,p}}{\epsilon (G_E^{\gamma,p})^2 + \tau (G_M^{\gamma,p})^2} G_M^{\gamma,s} \\
 & + \frac{G_F Q^2}{4\sqrt{2}\pi\alpha} \xi_V^{(0)} \frac{(1 - 4 \sin^2 \theta_W) \epsilon' G_M^{\gamma,p}}{\epsilon (G_E^{\gamma,p})^2 + \tau (G_M^{\gamma,p})^2} G_A^{e,p}, \tag{1.81}
 \end{aligned}$$

where  $G_A^{e,p}$  represents the radiatively corrected axial form factor.

It can also be written as a function of  $R$  parameters

$$\begin{aligned}
 A(\vec{e}p) = & - \frac{G_F Q^2}{4\pi\alpha\sqrt{2}} (1 - 4 \sin^2 \theta_w) (1 + R_V^p) \\
 & + \frac{G_F Q^2}{4\pi\alpha\sqrt{2}} (1 + R_V^n) \frac{(\epsilon G_E^{\gamma,p} G_E^{\gamma,n} + \tau G_M^{\gamma,p} G_M^{\gamma,n})}{\epsilon (G_E^{\gamma,p})^2 + \tau (G_M^{\gamma,p})^2} \\
 & + \frac{G_F Q^2}{4\pi\alpha\sqrt{2}} (1 + R_V^{(0)}) \frac{(\epsilon G_E^{\gamma,p} G_E^{\gamma,s} + \tau G_M^{\gamma,p} G_M^{\gamma,s})}{\epsilon (G_E^{\gamma,p})^2 + \tau (G_M^{\gamma,p})^2} \\
 & + \frac{G_F Q^2}{4\pi\alpha\sqrt{2}} (1 - 4 \sin^2 \theta_w) \frac{\epsilon' G_M^{\gamma,p} G_A^{e,p}}{\epsilon (G_E^{\gamma,p})^2 + \tau (G_M^{\gamma,p})^2}, \tag{1.82}
 \end{aligned}$$

where

$$\begin{aligned}
R_V^{(0)} &\equiv -\left(1 + \xi_V^{(0)}\right) \\
R_V^n &\equiv -(1 + \xi_V^n) \\
R_V^p &\equiv \frac{\xi_V^p}{(1 - 4 \sin^2 \theta_w)} - 1
\end{aligned} \tag{1.83}$$

and

$$G_A^{e,p} = -(1 + R_A^{T=1}) G_A^{T=1} + \sqrt{3} R_A^{T=0} G_A^{(8)} + (1 + R_A^{(0)}) G_A^s. \tag{1.84}$$

It is convenient to write Equation 1.82 in the following form

$$\begin{aligned}
A(\vec{e}p) = & - \frac{G_F Q^2}{4\pi\alpha\sqrt{2}} (1 - 4 \sin^2 \theta_w) (1 + R_V^p) \\
& + \frac{G_F Q^2}{4\pi\alpha\sqrt{2}} (1 + R_V^n) \frac{(\epsilon G_E^{\gamma,p} G_E^{\gamma,n} + \tau G_M^{\gamma,p} G_M^{\gamma,n})}{\epsilon (G_E^{\gamma,p})^2 + \tau (G_M^{\gamma,p})^2} \\
& + \frac{G_F Q^2}{4\pi\alpha\sqrt{2}} (1 + R_V^{(0)}) \epsilon G_E^{\gamma,p} \frac{(G_E^{\gamma,s} + \eta G_M^{\gamma,s})}{\epsilon (G_E^{\gamma,p})^2 + \tau (G_M^{\gamma,p})^2} \\
& + \frac{G_F Q^2}{4\pi\alpha\sqrt{2}} (1 - 4 \sin^2 \theta_w) \frac{\epsilon' G_M^{\gamma,p} G_A^{e,p}}{\epsilon (G_E^{\gamma,p})^2 + \tau (G_M^{\gamma,p})^2},
\end{aligned} \tag{1.85}$$

where

$$\eta = \frac{\tau G_M^{\gamma,p}}{\epsilon G_E^{\gamma,p}}. \tag{1.86}$$

Similarly, using Equation 1.48 in Equation 1.71, the electron-neutron parity-violating asymmetry becomes

$$\begin{aligned}
A(\vec{e}n) = & - \frac{G_F Q^2}{4\pi\alpha\sqrt{2}} (1 - 4 \sin^2 \theta_w) (1 + R_V^p) \\
& + \frac{G_F Q^2}{4\pi\alpha\sqrt{2}} (1 + R_V^n) \frac{(\epsilon G_E^{\gamma,p} G_E^{\gamma,n} + \tau G_M^{\gamma,p} G_M^{\gamma,n})}{\epsilon (G_E^{\gamma,n})^2 + \tau (G_M^{\gamma,n})^2} \\
& + \frac{G_F Q^2}{4\pi\alpha\sqrt{2}} (1 + R_V^{(0)}) \frac{(\epsilon G_E^{\gamma,n} G_E^{\gamma,s} + \tau G_M^{\gamma,m} G_M^{\gamma,s})}{\epsilon (G_E^{\gamma,n})^2 + \tau (G_M^{\gamma,n})^2} \\
& + \frac{G_F Q^2}{4\pi\alpha\sqrt{2}} (1 - 4 \sin^2 \theta_w) \frac{\epsilon' G_M^{\gamma,n} G_A^{e,n}}{\epsilon (G_E^{\gamma,n})^2 + \tau (G_M^{\gamma,n})^2},
\end{aligned} \tag{1.87}$$

The numerical values of the one-quark axial and vector electroweak radiative correction parameters are listed in Table 1.3.

R parameter	Value
$R_V^p$	-0.045(3)
$R_V^n$	-0.012(2)
$R_V^{(0)}$	-0.012(2)
$R_A^{T=1}$	-0.173(3)
$R_A^{T=0}$	-0.253(2)
$R_A^{(0)}$	-0.552(5)

TABLE 1.3: *One-quark vector electroweak radiative correction parameters [13]. The numbers in parentheses are errors.*

### Multi-quark correction

This section provides a brief summary of multi-quark effects to the electromagnetic amplitude [38]. The contribution of multi-quark effects to the electromagnetic amplitude is the addition of an anapole term to the proton transition current. The matrix element of the total current is

$$\mathcal{M}_\gamma + \mathcal{M}_\gamma^{anapole} = -i \frac{4\pi\alpha}{q^2} \bar{u} \gamma_\mu u (J_\mu^p + J_\mu^{anapole}), \quad (1.88)$$

where  $J_\mu^p$  is defined in Equation 1.17 and  $J_\mu^{anapole}$  is the anapole current. The interference between these two amplitudes produces an additional asymmetry  $A^{anapole}$ . The total asymmetry is then the sum of the one-quark asymmetry given in Equation 1.82 and the anapole asymmetry

$$A = A^{1-quark} + A^{anapole}. \quad (1.89)$$

The anapole current can be written as

$$J_\mu^{anapole} = \mathcal{K} (a_s F_s^{anapole}(Q^2) + a_v F_v^{anapole}(Q^2)) \bar{u}_x [(q^2 \gamma^\mu - q^\mu \Gamma) \gamma_5] u_x, \quad (1.90)$$

where  $x = p, n$  represents a proton  $p$  or a neutron  $n$ ,  $u_x$  and  $u_{x'}$  are the Dirac spinors for the nucleon in the entrance and exit channel respectively, and  $a_s$  and  $a_v$  are the scalar and vector contributions to the anapole moment respectively.  $F_s^{anapole}(Q^2)$

R parameter	Value
$R_A^{T=1}$	-0.087(0.35)
$R_A^{T=0}$	0.015(0.20)

TABLE 1.4: *Multi-quark axial electroweak radiative correction parameters [14].*

and  $F_v^{anapole}(Q^2)$  are scalar and vector anapole form factors, where

$$F_s^{anapole}(Q^2 = 0) = F_v^{anapole}(Q^2 = 0) = 1. \quad (1.91)$$

The  $\mathcal{K}$  coefficient is a numerical constant which allows one to normalize the different theoretical calculations according to the lagrangians used. The anapole asymmetry is

$$A^{anapole} = -2\mathcal{K}Q^2 \frac{\epsilon' G_M^{\gamma,x} \left( a_s F_s^{anapole}(Q^2) + a_v F_v^{anapole}(Q^2) \tau_3(x) \right)}{\epsilon (G_E^{\gamma,x})^2 + \tau (G_M^{\gamma,x})^2}, \quad (1.92)$$

where

$$\tau_3 = \begin{cases} 1 & x = p \\ -1 & x = n \end{cases} \quad (1.93)$$

The numerical values of the multi-quark axial electroweak radiative correction parameters are listed in Table 1.4.

## 1.10 Unpolarized Electron Scattering

The electromagnetic form factors of the nucleon  $G_{E,M}^{p,n}$  are important quantities to us since they are necessary to extract  $G_{E,M}^s$ . The proton electric and magnetic form factors have been studied extensively in the past from unpolarized electron-proton elastic scattering using the Rosenbluth separation technique [39]. The neutron electric and magnetic form factors have been deduced from unpolarized elastic and quasielastic electron-deuteron scattering, respectively [39].

### 1.10.1 Elastic Electron-Proton Scattering

The differential cross-section for electron-neutron scattering, in terms of the electric and magnetic form factors, is given by the Rosenbluth formula

$$\frac{d\sigma}{d\Omega} = \left(\frac{d\sigma}{d\Omega}\right)_{Mott} \left[ \frac{(G_E^p)^2 + \tau(G_M^p)^2}{1 + \tau} + 2\tau(G_M^p)^2 \tan^2\left(\frac{\theta}{2}\right) \right], \quad (1.94)$$

where  $\sigma_M$  is the Mott cross section describing the scattering from a pointlike target.

The essential feature is that

$$\frac{\left(\frac{d\sigma}{d\Omega}\right)}{\left(\frac{d\sigma}{d\Omega}\right)_{Mott}} = A(Q^2) + B(Q^2) \tan^2 \frac{\theta}{2}. \quad (1.95)$$

If one plots the cross-section versus  $\tan^2 \frac{\theta}{2}$  for different incident momenta and different scattering angles, such that  $Q^2$  remains fixed, a linear dependence is obtained. Information about  $(G_E^p)^2$  and  $(G_M^p)^2$  can be obtained from the slope and intercept of the curve. This is called the Rosenbluth technique. In the low  $Q^2$  region, the  $(G_E^p)^2$  term dominates the cross section (since  $\tau$  is directly proportional to  $Q^2$ ). Conversely, the  $(G_M^p)^2$  term dominates the cross section in the high  $Q^2$  region. Therefore, the determination of  $G_E^p$  at high  $Q^2$  and  $G_M^p$  at low  $Q^2$  is difficult. Recent world data on the proton magnetic and electric form factors is shown in Figure 1.6. The data are presented as  $\frac{G_E^p}{G_D}$  and  $\frac{G_M^p}{\mu_p G_D}$ , where  $G_D = \left(1 + \frac{Q^2}{0.71 \text{ MeV}^2}\right)^{-2}$  is the standard dipole parameterization. The data are plotted as a function of  $Q^2$ .

### 1.10.2 Electron-Deuteron Scattering

Less is known about the neutron electromagnetic structure because free neutron targets do not exist. Therefore, the neutron electric and magnetic form factors are known with much less precision than the proton electric and magnetic form factors. In the past, they have been deduced from both elastic and quasielastic electron-deuteron scattering [39]. Another difficulty is that the net charge of the neutron is

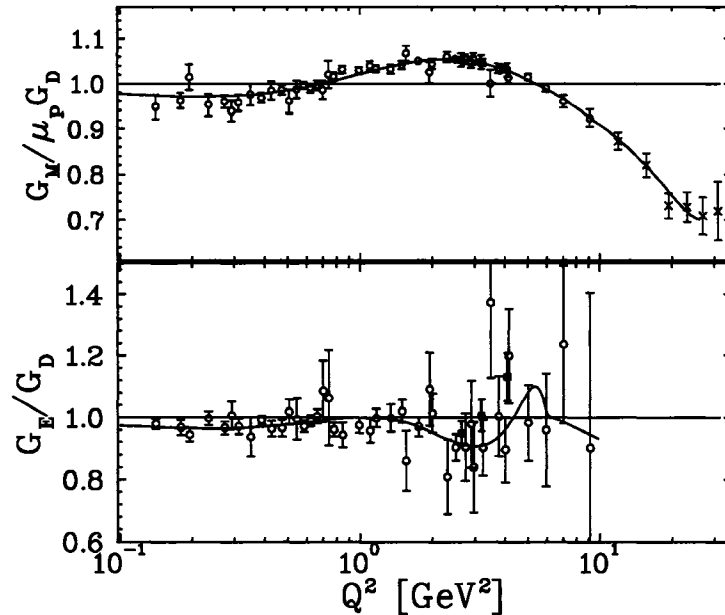


FIG. 1.6:

*Recent world data on the proton magnetic and electric form factors [18]. The black circles represent a global analysis by J. Arrington [15], the blue squares correspond to I.A. Qattan [16], and the pink “x”s correspond to Sill [17]. The line is a fit to all data.*

zero. In other words, the neutron electric form factor is much smaller than its magnetic form factor. Consequently, the magnetic part of the contribution dominates the cross section. This makes it difficult to extract  $G_E^n$  from the unpolarized cross section using nuclear targets.

### Elastic Electron-Deuteron Scattering

The differential cross-section for unpolarized elastic electron-deuteron scattering takes the form of Equation 1.95, where  $A(Q^2)$  and  $B(Q^2)$  are structure functions which can be separated by the Rosenbluth technique. The deuteron is a spin-1 nucleus and it requires three form factors to characterize its charge and magnetization distributions:  $F_C(Q^2)$ ,  $F_Q(Q^2)$ , and  $F_M(Q^2)$ . They are the charge monopole,

black square	C. Herberg [23]	D(e,e'n)p - recoil polarization
green triangle	I. Passchier [24]	D(e,e'n)p - polarized target (exclusive)
red triangle	R. Madey [25]	D(e,e'n)p - recoil polarization
blue "x"	Schiavilla and Sick [26]	theory from deuteron form factors
blue diamond	J. Golak [27]	<sup>3</sup> He(e,e'n) - polarized target (exclusive)
pink star	D.I. Glazier [28]	D(e,e'n)p - recoil polarization
black circle	G. Warren [29]	D(e,e'n)p - polarized target (exclusive)

TABLE 1.5:

*Contributors to recent world data on the electric form factor of the neutron.*

quadrupole and the magnetic dipole form factors, respectively. In terms of the three form factors, the structure functions are

$$A(Q^2) = F_C^2(Q^2) + \frac{8}{9}\tau^2 F_Q^2(Q^2) + \frac{2}{3}\tau F_M^2(Q^2) \quad (1.96)$$

$$B(Q^2) = \frac{4}{3}\tau(1 + \tau) F_M^2(Q^2). \quad (1.97)$$

This system of equations cannot be solved. Hence, it is impossible to separate all three deuteron form factors from the unpolarized elastic electron-deuteron cross section. An additional measurement involving polarization is required. Figure 1.7 shows recent world data on  $G_E^n$  as a function of  $Q^2$ . The different symbols are defined in Table 1.5. Recoil polarization is a technique which employs a polarized beam and an unpolarized target and measures the polarization of the outgoing proton. Inclusive scattering measures only the outgoing electron while exclusive scattering makes other measurements to determine the final state (elastic, inelastic, quasi-elastic).

### Quasielastic Electron-Deuteron Scattering

Quasielastic electron-deuteron scattering is a second technique used to extract the electromagnetic form factors of the neutron. In this process, the electron scatters



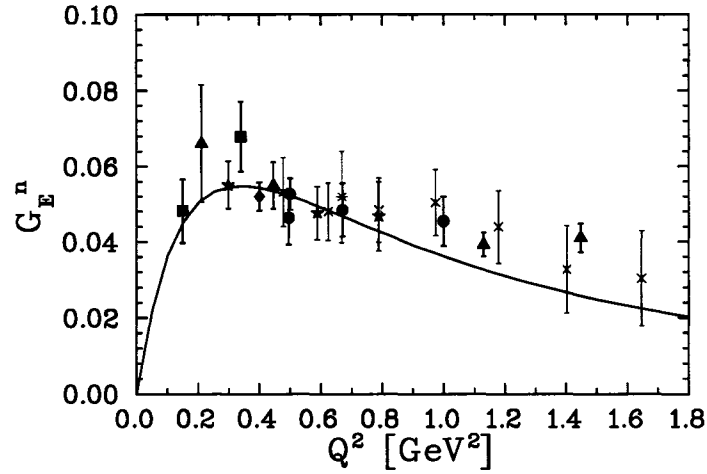


FIG. 1.7:

*Recent world data on the electric form factor of the neutron [18]. See Table 1.5 for a definition of the symbols.*

from the nucleon inside the deuteron. It includes measurements in which only scattered electrons are detected and coincidence measurements where both the scattered electron and the knockout neutron are measured.

The quasielastic electron-deuteron cross-section per nucleon,  $\sigma(E, E', \theta)$  converted to the reduced cross-section is

$$\sigma_R = \epsilon(1 + \tau) \frac{\sigma(E, E', \theta)}{\sigma_M} = R_T + \epsilon R_L, \quad (1.98)$$

where  $R_T$  and  $R_L$  are the transverse and longitudinal nuclear response functions. In the plane wave impulse approximation (PWIA), the  $R_T$  response function is proportional to  $(G_M^n)^2 + (G_M^p)^2$ . Similarly, the  $R_L$  response function is proportional to  $(G_E^n)^2 + (G_E^p)^2$ . Hence, the extraction of the neutron electromagnetic form factor requires the separation of the  $R_L$  and  $R_T$  response functions. Recent world data on  $G_M^n$  are shown in Figure 1.8. The data are plotted as a function of  $Q^2$ .

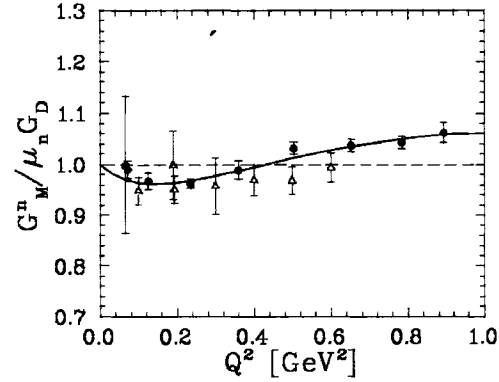


FIG. 1.8:

Recent world data on the magnetic form factor of the neutron [18]. The black circles are quasielastic  $d(e, e'n)/d(e, e'p)$  ratio measurements by Anklin [19] and Kubon [20], and the red triangles are polarization measurements by Anderson [21] and Gao [22].

## 1.11 Polarized Electron Scattering

### 1.11.1 Elastic Electron-Proton Scattering

With a polarized beam and either a polarized target or detection of the polarization of the recoiling proton, it is possible to determine directly the ratio  $\frac{G_E^p}{G_M^p}$ . The elastic scattering of longitudinally-polarized electrons from unpolarized protons results in a transfer of polarization to the recoil proton with two nonzero components.  $P_t$  is perpendicular to the proton momentum in the scattering plane while  $P_l$  parallel to the proton momentum in the scattering plane. With a longitudinally polarized beam and detection of the recoil polarization, the ratio of polarization components perpendicular and parallel to the nucleon is

$$\frac{G_E^p}{G_M^p} = -\frac{P_t}{P_l} \frac{E + E'}{2M} \tan \frac{\theta}{2}. \quad (1.99)$$

green "x"	BLAST [30]
black circle	JLab polarization transfer [31], [32], [33]
solid star	G. MacLachlan [34]
hollow star	M. Jones [35]
red square	T. Pospischil [36]
blue triangle	B. Milbrath [37]

TABLE 1.6:

*Contributors to recent world data on the proton form factor ratio.*

The form factor ratio can be determined from a simultaneous measurement of the two recoil polarization components. Figure 1.9 shows recent world data on the proton form factor ratio. The different symbols are defined in Table 1.6.

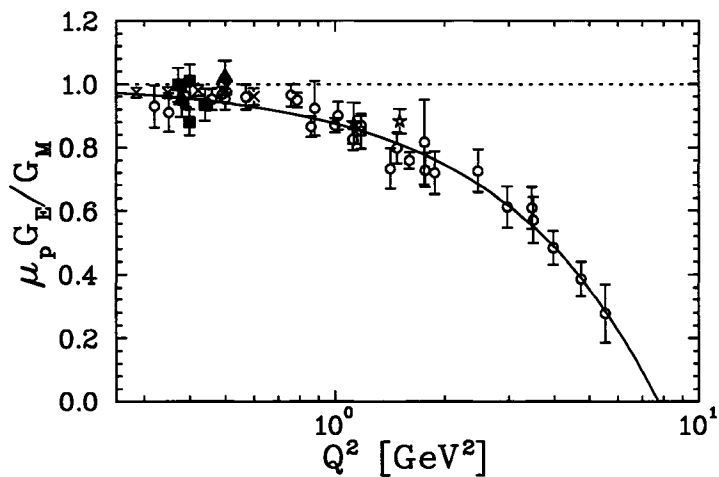


FIG. 1.9:

*World data on the proton electric and magnetic form factor ratio  $\frac{\mu G_E}{G_M}$  as a function of  $Q^2$  [18]. See Table 1.6 for a definition of the symbols.*

## 1.12 Related Experiments

Three experiments have published results of parity-violating electron scattering measurements on the proton at forward angles, and on the proton and deuteron at

backward angles. Each of these individual experiments is sensitive to different linear combinations of  $G_E^s$ ,  $G_M^s$ , and the axial form factor  $G_A^{Z,p}$  at different values of  $Q^2$ .

### 1.12.1 SAMPLE

The primary goal of the SAMPLE experiment at the MIT-Bates Laboratory was to determine the contribution of strange quarks to the nucleon's magnetic moment. In the SAMPLE experiment, parity-violating electron scattering was measured in the backward direction, from both hydrogen and deuterium targets, in order to determine  $G_M^s$  and  $G_A^e(T = 1)$  at  $Q^2 = 0.1$  (GeV/c)<sup>2</sup>. The hydrogen measurement was carried out in 1998, followed by the deuterium measurement in 1999.

The experiment consisted of a 200 MeV, 40  $\mu$ A polarized beam incident on a 40 cm long aluminum cell filled with liquid hydrogen. After the scattered electrons exited the target, they passed through a 3.1 mm thick hemispherical aluminum scattering chamber lined with 2.5 mm of Pb. The scattering chamber was followed by a volume of air that served as a Cerenkov medium for the detector. The detector was made up of ten ellipsoidal mirrors that focused Cerenkov light onto ten photomultiplier tubes arranged symmetrically about the beam axis, covering angles between 130° and 170°. The scattered electron rate was integrated over the 25  $\mu$ s beam pulse and sorted by beam helicity state, which was flipped pseudo-randomly at 600 Hz. A schematic of the SAMPLE detector is shown in Figure 1.10.

The first analysis of the hydrogen and deuterium data sets found the measured isovector (isospin 1) axial form factor  $G_A^e(T = 1)$  to be in disagreement with the theoretical expectation. As a result, a second deuterium scattering experiment was performed in 2001-2002, at a lower beam energy of 125 MeV, corresponding to a momentum transfer of 0.038 (GeV/c)<sup>2</sup>. An analysis of the third data set yielded different experimental systematic uncertainties than the first experiment but similar

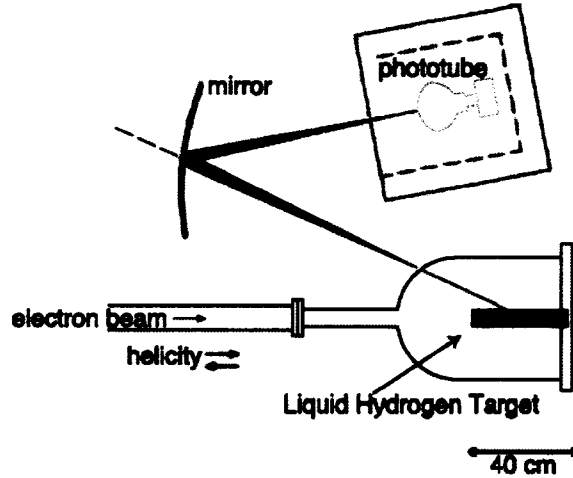


FIG. 1.10:

*Schematic diagram of the layout of the SAMPLE target and detector system.*

sensitivity to  $G_A^e(T = 1)$ . An updated analysis of all three data sets has brought both deuterium experiments into good agreement with theory, with little change to the extracted value of  $G_M^s$ .

Combining the measured hydrogen asymmetry with the theoretically determined value of  $G_A^e(T = 1) = -0.83 \pm 0.26$  [14], results in [42]

$$G_M^s(Q^2 = 0.091) = 0.37 \pm 0.20 \pm 0.26 \pm 0.07 \quad (1.100)$$

where the first uncertainty is statistical, the second uncertainty is systematic, and the third uncertainty is due to knowledge of the electromagnetic form factors and of the electroweak radiative corrections to  $G_A^e(T = 1)$ .

The results from the 200 MeV data, in the space of  $G_M^s$  versus  $G_A^e(T = 1)$ , along with the theoretically expected value of  $G_A^e(T = 1)$ , are shown in Figure 1.11. The three bands correspond to the hydrogen data, deuterium data, and the theoretically expected value of  $G_A^e(T = 1)$ . The larger ellipse corresponds to a  $1\sigma$  overlap of the two data sets and the smaller ellipse corresponds to an overlap of the hydrogen data

and theory. The resulting values of the form factors are [42]

$$G_M^s = 0.23 \pm 0.36 \pm 0.40 \quad (1.101)$$

$$G_A^e(T=1) = -0.53 \pm 0.57 \pm 0.50. \quad (1.102)$$

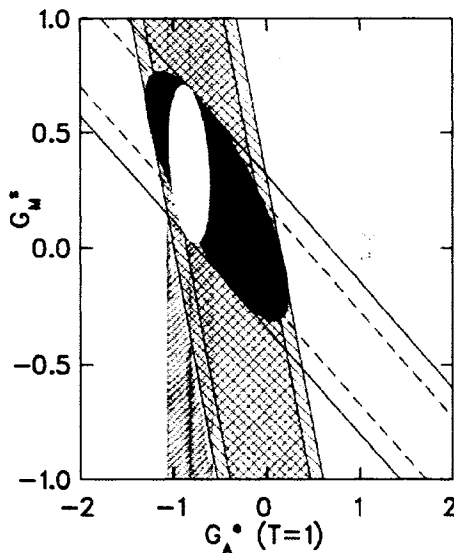


FIG. 1.11: Results from the 200 MeV SAMPLE data, in the space of  $G_M^s$  versus  $G_A^e(T=1)$ . The three bands correspond to hydrogen, deuterium, and the theoretically expected value of  $G_A^e(T=1)$ . The larger ellipse is a  $1\sigma$  overlap of the two data sets and the smaller ellipse is an overlap of the hydrogen data and theory.

### 1.12.2 HAPPEX

The first measurements of parity-violating electron scattering at Jefferson Laboratory were carried out by the HAPPEX collaboration. The experiment used a 3.2 GeV polarized beam on a 15 cm long unpolarized liquid hydrogen target and detected the scattered electrons using the pair of high resolution spectrometers (HRS) in Hall A at  $12.5^\circ$ . A schematic of the HAPPEX experiment is shown in Figure 1.12. Since measurements are made at forward angles, the asymmetry

is sensitive to  $G_E^s$  and  $G_M^s$ . The measured asymmetry, at  $Q^2 = 0.477 \text{ (GeV/c)}^2$ , is  $A_{PV} = (-15.05 \pm 0.98 \pm 0.56) \text{ ppm}$  [43], where the first uncertainty is due to statistics and the second uncertainty is systematic. Based on these data as well as data on electromagnetic form factors, HAPPEX extracted a linear combination of strange form factors [43]

$$G_E^s + 0.392G_M^s = 0.014 \pm 0.020 \pm 0.010, \quad (1.103)$$

where the first error arises from this experiment and the second arises from the electromagnetic form factor data.

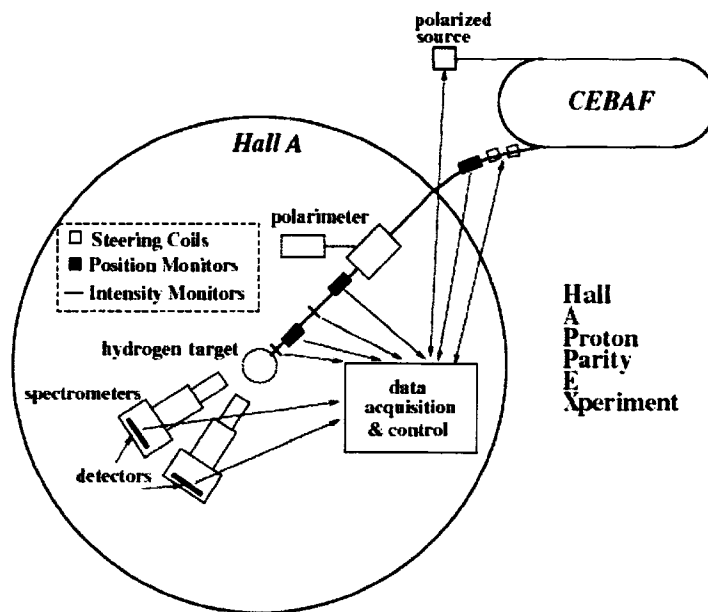


FIG. 1.12: Schematic of the HAPPEX experiment.

The second measurement was carried out with a beam energy of 3.03 GeV on a 20 cm long unpolarized liquid hydrogen target and a scattering angle  $\theta_{lab} = 6.0^\circ$ . The measured asymmetry, at  $Q^2 = 0.099 \text{ (GeV/c)}^2$ , is  $A_{PV} = -1.14 \pm 0.24 \pm 0.06$

ppm [44]. From this, the strange form factor combination is [44]

$$G_E^s + 0.080G_M^s = 0.030 \pm 0.025 \pm 0.006 \pm 0.012, \quad (1.104)$$

where the first two errors are experimental and the last error is due to the uncertainty in the electromagnetic form factors.

The third experiment measured the parity-violating electroweak asymmetry in the elastic scattering of polarized electrons from  ${}^4\text{He}$  at an average scattering angle  $\theta_{lab} = 5.7^\circ$  and a  $Q^2 = 0.091 \text{ GeV}^2$ . From these data, for the first time, the strange electric form factor of the nucleon  $G_E^s$  was isolated. The measured asymmetry is  $A_{PV} = 6.72 \pm 0.84 \pm 0.21 \text{ ppm}$  [45] and yields a value of [45]

$$G_E^s = -0.038 \pm 0.042 \pm 0.010 \quad (1.105)$$

consistent with zero.

The fourth experiment measured the parity-violating electroweak asymmetry in the elastic scattering of polarized electrons off both hydrogen and  ${}^4\text{He}$  with  $\theta_{lab} \sim 6^\circ$ . This experiment significantly improved the previous two measurements of  $A_{PV}$  for hydrogen  ${}^1\text{H}$  and  ${}^4\text{He}$  nuclei and reported the most precise constraints on the strange form factors at  $Q^2 \sim 1 \text{ GeV}^2$ . The  ${}^4\text{He}$  result is  $A_{PV} = (6.40 \pm 0.23 \pm 0.12) \text{ ppm}$  and the hydrogen result is  $A_{PV} = (-1.58 \pm 0.12 \pm 0.04) \text{ ppm}$  [46], where the first uncertainty is due to statistics and the second uncertainty is systematic. From these results, HAPPEX extracted [46]

$$G_E^s = 0.002 \pm 0.014 \pm 0.007, \quad (1.106)$$

at  $\langle Q^2 \rangle = 0.077 \text{ GeV}^2$  and

$$G_E^s + 0.09G_M^s = 0.007 \pm 0.011 \pm 0.006 \quad (1.107)$$

at  $\langle Q^2 \rangle = 0.109 \text{ GeV}^2$ . These results provide new limits on the role of strange quarks in the nucleon charge and magnetization distributions.



### 1.12.3 PVA4

The PVA4 experiment is underway at the Mainzer Microton (MAMI) in Mainz, Germany. The experiment measured the parity-violating asymmetry in the scattering of polarized electrons on unpolarized protons using counting techniques. This was the first time that a parity-violating asymmetry in electron scattering was been measured by counting individual, scattered particles. The scattered electrons were detected over a range of angles, centered at  $35^\circ$ , with a  $\text{PbF}_2$  Cerenkov shower calorimeter. The calorimeter design consists of 1022  $\text{PbF}_2$  crystals of 16-20 radiation lengths thickness, arranged in 7 rings. A schematic of the experiment is shown in Figure 1.13.

The first PVA4 measurement was at a beam energy of 855 MeV, corresponding to  $Q^2 = 0.23 (\text{GeV}/c)^2$  and a sensitivity to the combination  $G_E^s + 0.22G_M^s$ . A  $20 \mu\text{A}$  beam of polarized electrons was incident on a 10 cm liquid hydrogen target. The experimental asymmetry was measured to be  $A = -5.44 \pm 0.54 \pm 0.26$  ppm [47], where the first error represents the statistical accuracy, and the second represents the systematical uncertainties including beam polarization. A linear combination of the strange electric and magnetic form factors was extracted [47]

$$G_E^s + 0.255G_M^s = 0.039 \pm 0.034. \quad (1.108)$$

The statistical and systematic errors are added in quadrature.

The second measurement was at 570 MeV beam energy and a corresponding  $Q^2 = 0.108 (\text{GeV}/c)^2$  and at a forward electron scattering angle of  $30^\circ < \theta_e < 40^\circ$ . The measured asymmetry is  $A = -1.36 \pm 0.29 \pm 0.13$  ppm [48]. The strangeness contribution to the electromagnetic form factors is [48]

$$G_E^s + 0.106G_M^s = 0.071 \pm 0.036. \quad (1.109)$$

To separate the electric and magnetic strangeness contributions to the electromag-

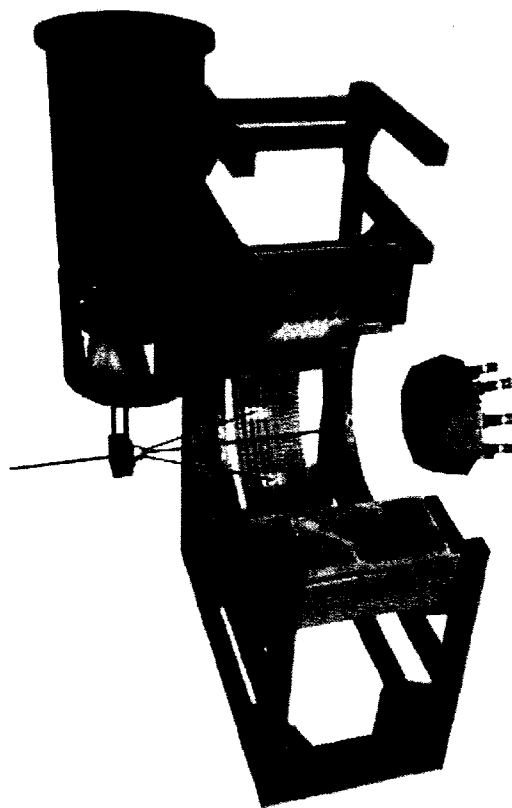


FIG. 1.13: Schematic of the PVA4 experiment performed at the Mainz Microtron. The calorimeter is comprised of 1022  $\text{PbF}_2$  crystals. The beam enters from the left and hits the hydrogen (deuterium) cell. Elastic scattered electrons deposit their energy in 9 crystals where the electromagnetic shower is converted into Cherenkov light. The light is read out by 1022 photomultiplier tubes. The detector on the right is a water cherenkov luminosity detector. It is positioned symmetrically around the beam axis and registers the flux of scattered particles.

netic form factors of the nucleon, the PVA4 collaboration is preparing to measure the parity violating asymmetry in the scattering of electrons off both protons and deuterons at backward scattering angles. This will allow a confirmation of the strange quark contribution to the nucleon form factors.

### 1.12.4 $G^0$ Forward Angle Experiment

The  $G^0$  experiment at JLab is a dedicated apparatus designed to determine  $G_E^s$ ,  $G_M^s$ , and  $G_A^e$  from a single experimental apparatus over a broad  $Q^2$  range. The actual measurement is being performed in two phases. The first phase is the forward angle experiment and the second phase is the backward angle experiment. In the forward angle experiment, the detector consisted of a superconducting toroidal spectrometer with an array of scintillators along the focal plane to determine the parity-violating asymmetry at forward electron scattering angles. Polarized electrons were scattered from a 20 cm liquid hydrogen target. The recoil protons were detected and sorted by  $Q^2$ , covering the range  $0.1 < Q^2 < 1.0$  (GeV/c)<sup>2</sup>. The flight time from the target to the scintillator array was determined for each scattered particle, allowing the rejection of photo-produced pions and many of the protons generated from inelastic processes. In order to determine the flight times of the detected particles, which range from 5-25 ns, the time structure of the JLab beam was modified from its nominal 2 ns between micropulses to be 32 ns between micropulses.

While a determination of separated values for  $G_M^s$  and  $G_E^s$  will require the backward angle measurements as well, of which this thesis represents a first step, the results of the forward angle experiment extended the kinematic reach and improved the precision of the available data on parity-violating  $e - p$  scattering. The results of the experiment are shown as a function of momentum transfer in Figure 1.14. The quantity  $G_E^s + \eta G_M^s$  is calculated using the electromagnetic form factors of Kelly. Also shown is the excellent agreement with the HAPPEX measurements made at nearly the same kinematic points. The error bars include the statistical uncertainty (inner) and statistical plus point-to-point systematic uncertainties added in quadrature (outer). The error bands represent, for the  $G^0$  experiment, the global systematic uncertainties: from the measurement (upper) and from the uncertainties

in the quantities entering  $A_{NVS}$  (lower).

To characterize the result with a single number, randomized data sets were generated with the constraint  $G_E^s + G_M^s = 0$ , distributed according to the statistical and systematic uncertainties. The fraction of these with  $\chi^2$  larger than that of our data set was 11%, so we conclude that the non-strange hypothesis is disfavored with 89% confidence.

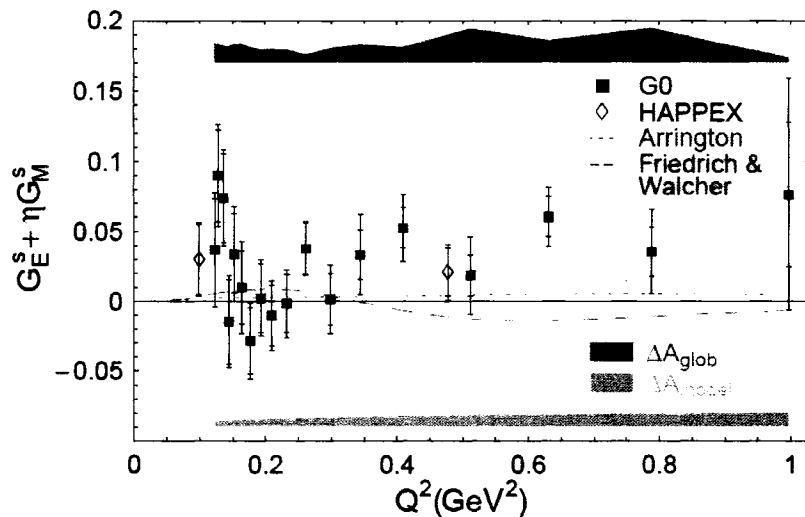


FIG. 1.14: *Results of the  $G^0$  forward angle experiment as a function of momentum transfer. The gray bands indicate systematic uncertainties. The lines correspond to different electromagnetic nucleon form factor models [49].*

### 1.12.5 World Data on Strange Form Factors at $Q^2 = 0.1$ $\text{GeV}^2$

The most amount of information about strange form factors is located near  $Q^2 = 0.1 \text{ GeV}^2$ . At this  $Q^2$ , there are five results: SAMPLE, PVA4, HAPPEX hydrogen, HAPPEX helium, and  $G^0$ . The measurements can be combined in a plot of  $G_E^s$  versus  $G_M^s$  as shown in Figure 1.15. This Figure uses the first HAPPEX

results. The experiments are in good agreement and the combined results are [50]

$$G_E^s = -0.013 \pm 0.028 \quad (1.110)$$

$$G_M^s = 0.62 \pm 0.31. \quad (1.111)$$

The electric form factor is consistent with zero within precision while the magnetic form factor is non-zero at the two-sigma level. If the true value of the strange magnetic form factor is near the central value, then the effect of the strange quark is not small. Therefore, experiment has not yet ruled out the potentially large strange quark sea contributions to the nucleon's magnetic properties. The HAPPEX and PVA4 programs are continuing and will allow a separation of  $G_E^s$  and  $G_M^s$  at different values of  $Q^2$  in the near future.

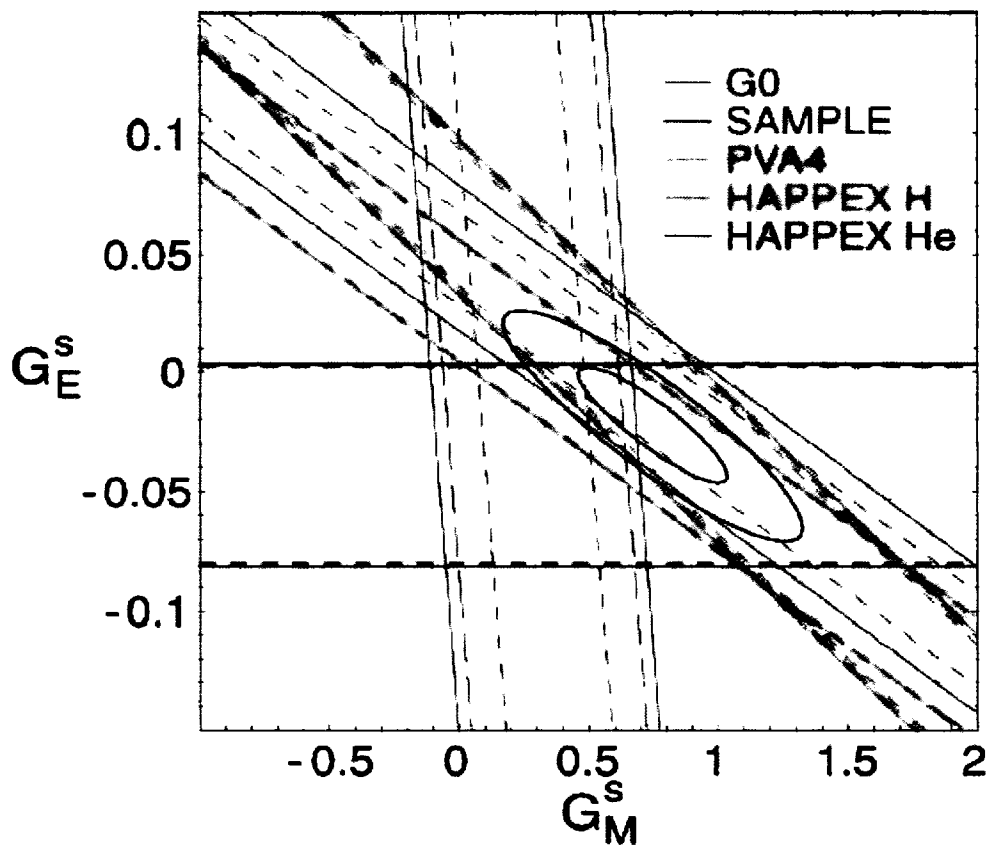


FIG. 1.15: World data on strange form factors at  $Q^2 = 0.1 \text{ GeV}^2$  [50]. Results are from *SAMPLE*, *PVA4*, *HAPPEX* hydrogen, *HAPPEX* helium, and *G0*. The bands for each experiment represent statistical, quadrature sums of statistical and systematic, and statistical + systematic + model uncertainties. The large ellipse indicates the 96% confidence region while the small ellipse indicates the 68% confidence region.

# CHAPTER 2

## $G^0$ Experimental Equipment

### 2.1 Experimental Overview

The  $G^0$  experiment studies the collisions between a beam of polarized electrons and target particles. Specifically, it measures the interference of the electromagnetic interaction, in which a photon is exchanged, and the neutral weak interaction, which involves the exchange of a  $Z^0$  boson. The apparatus consists of a beam of polarized electrons from the Jefferson Lab accelerator, a liquid hydrogen or deuterium target which provides the protons or complex nuclei for the scattering and a spectrometer to measure the scattering products. Figure 2.1 is a schematic of the  $G^0$  apparatus used in the forward angle experiment. Figure 2.2 is a floor plan of Hall C with the  $G^0$  apparatus installed in the backward-angle mode. A discussion of CEBAF itself and the electron source is deferred to Chapter 3.

The actual measurement is performed in two experiments. In the forward angle experiment, a proton recoiling from its interaction with an electron was bent in the magnetic field produced by the superconducting coils according to its momentum. Protons of different momenta, bending by different amounts in the magnetic field,

struck the array of particle detectors in different places. In the backward angle experiment, the whole apparatus was reversed relative to the beam direction and scattered electrons rather than protons were detected.

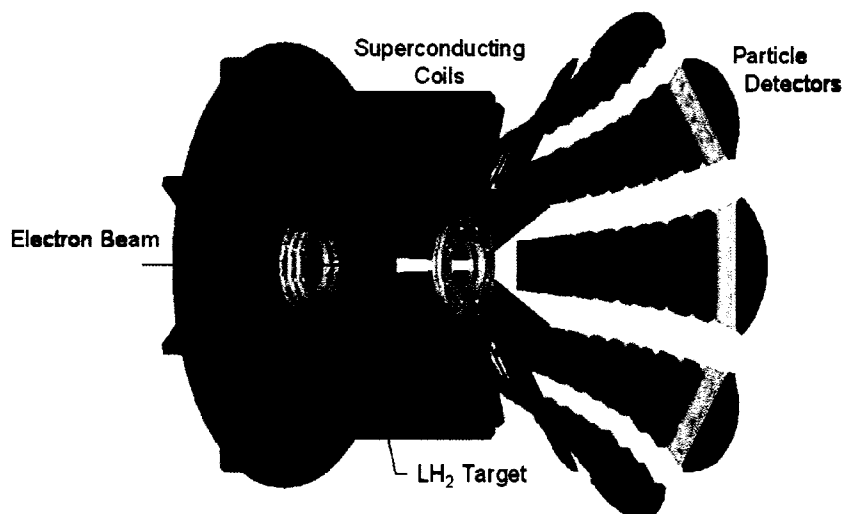


FIG. 2.1: Schematic view of the  $G^0$  Experiment showing the spectrometer in the forward angle configuration. Two of the eight coils of the magnet and one sector of the detectors have been removed for clarity. The spectrometer is comprised of an eight sector superconducting toroidal magnet that focuses recoil protons (forward scattering measurement) or electrons (backward measurement) from a 20 cm long liquid target to detectors.

The challenge of the experiment stems from the fact that the electromagnetic force is much stronger than the weak force. Consequently, the experimental asymmetry is very small (less than 50 ppm). The difficulty is not in making the measurement but controlling the systematics. Careful attention has to be paid to the possibility of false asymmetries disguised as the true asymmetry.



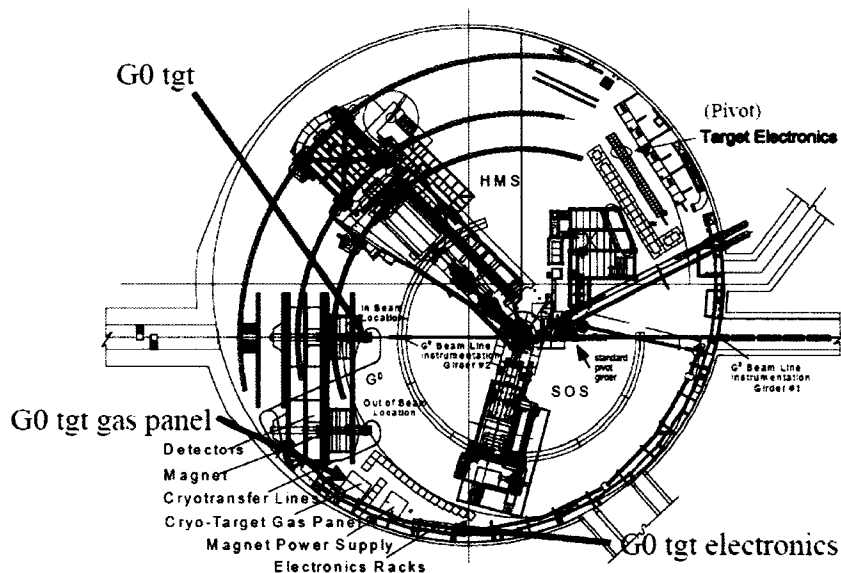


FIG. 2.2:

*Floor plan of Hall C with the  $G^0$  apparatus installed in the backward-angle mode.*

## 2.2 Magnet

The function of the superconducting magnet system [52] is to focus elastically charged particles of the same momentum and scattering angle from the length of the target to a single point in each of the eight octants of the spectrometer. The superconducting magnet system is a toroidal magnet made up of eight superconducting coils in a single cryostat. The coils supply the toroidal fields, with a nominal coil current of 3500 A. Each coil is made of 144 turns of integrated superconductor. The coil cable becomes superconducting at temperatures below 8 K. The coils are arranged aximuthally around a central bore region and are interleaved between eight collimator modules made of aluminum and lead. The collimators define the spectrometer acceptance and provide shielding between the target and detectors. They block direct view from the target to the Focal Plane Detectors (see Section 2.4.1), thereby shielding against neutral particles. The coils are cooled by liquid

helium flowing in four parallel paths. Each path includes two coils in series. Two additional parallel cooling paths are used to cool the superconducting electrical bus. The electrical bus supplies power to the coils in series. The coils, electrical bus, and collimators comprise what is called the cold mass. The cold mass and cryostat shell are shown in Figure 2.3.

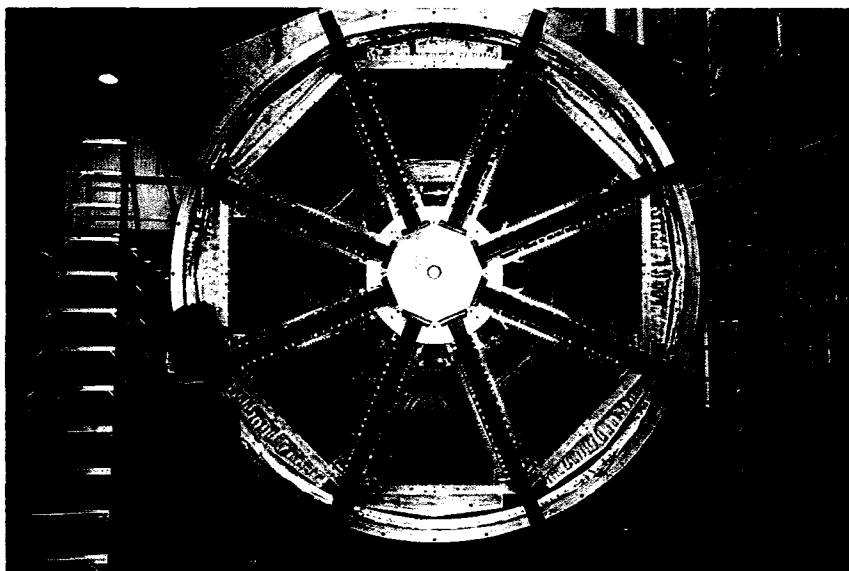


FIG. 2.3: *The SMS cold mass and cryostat shell.*

A liquid nitrogen shield surrounds the cold mass to intercept heat due to radiation and conduction. The shield consists of an external aluminum cylinder, fastened to a frame made of thin extruded aluminum. The cold mass and shield are contained in a vacuum vessel comprised of a 4 m diameter, 2 m long cylindrical shell and two aluminum end-caps. In the downstream vacuum endcap, there are eight thin titanium windows,  $0.51 \text{ m}^2$  in area. These windows provide a path of low energy loss for particles emanating from the target to the detectors.

## 2.3 Target

This section describes the main features of the  $G^0$  target system. A complete description is given in [51]. The backward angle experiment employed two unpolarized cryogenic liquid targets: hydrogen and deuterium. The primary components of the target system include a “wind sock” to direct the fluid flow down the center of the target cell and back along the cell walls, a heat exchanger to cool the fluid, and a pump to recirculate the target fluid. A schematic of the liquid hydrogen target, which is centered inside the liquid nitrogen shield of the superconducting magnet, is shown in Figure 2.4.

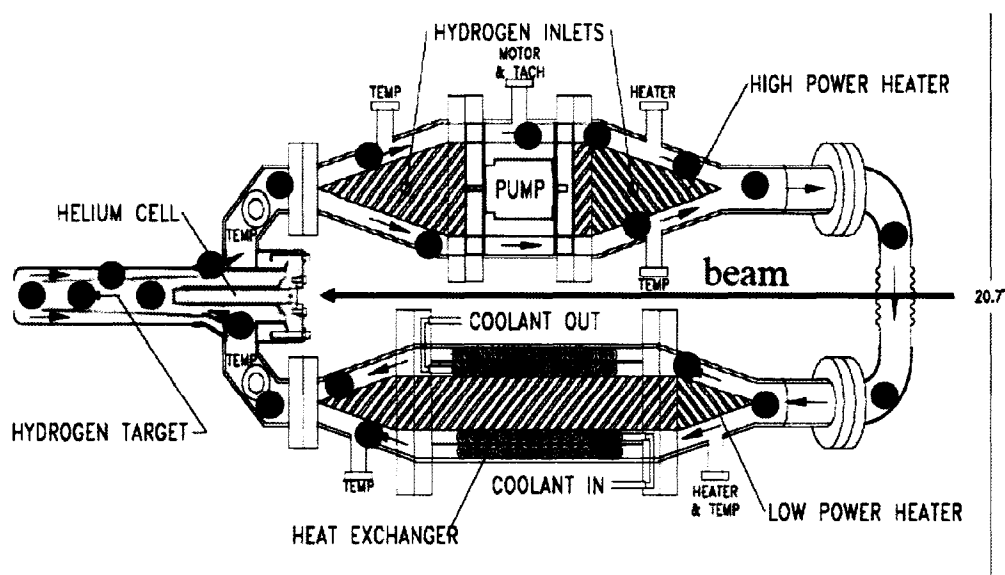


FIG. 2.4: Schematic of the liquid hydrogen target, centered inside the liquid nitrogen shield of the superconducting target. The electron beam enters from the right.

The target manifold, as shown in Figure 2.5, houses two cells, a hydrogen cell and a helium cell. The hydrogen cell is a 5 cm diameter aluminum tube with a rounded endcap. It is 23 cm long and has a shell thickness of 0.178 mm. The downstream wall of the cell serves as the exit window of the target and is 0.0762 mm

thick with a diameter of 8 mm. The helium cell is a 16 cm long cylinder with a inner diameter of 1.27 cm. It is located upstream of the hydrogen cell. The downstream window of the helium cell, with a thickness of 0.228 mm, served as the entrance window of the hydrogen cell. The length of the liquid hydrogen target is 20 cm and is defined by the distance between the entrance and exit window of the hydrogen cell. The upstream end of the helium cell is shielded from the vacuum by an aluminum window of 0.178 mm thicknes. The helium cell serves two primary functions. First, it eliminates first-order variations in target thickness with beam position by matching the radius of curvature of the entrance and exit windows. Second, the entrance window of the hydrogen cell is azimuthally symmetric. The asymmetric joints of the vacuum window of the manifold are pushed further upstream, outside of the detector acceptance.

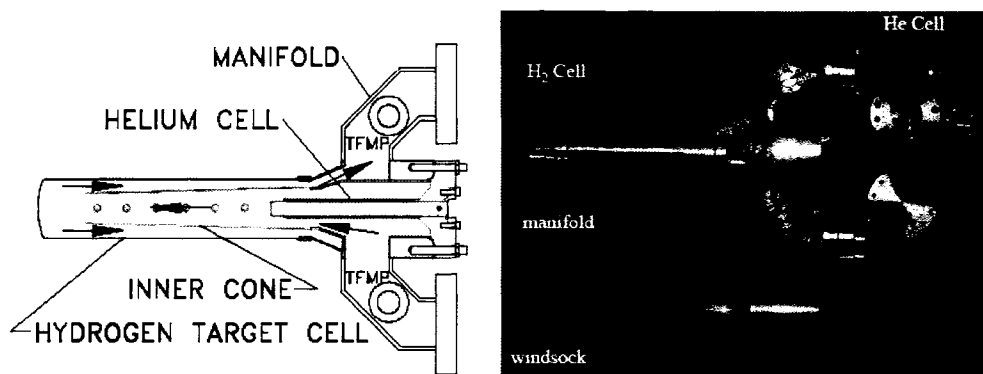


FIG. 2.5: *The target cell and manifold.*

The function of the heat exchanger is to cool the cryogenic fluid. It is located in the bottom leg of the target loop in Figure 2.4. Compressed helium gas (15 K, 12 atm) is provided by the end station refrigerator and circulated through the heat exchanger, with a flow rate of the helium of 6 g/s. The heat exchanger removes about 50 W per g/s of coolant flow. In addition, the heat exchanger has two heaters. One heater is low power and one heater is high power. The maximum operating power

of the high power heater is 1000 W. Its primary purpose is to compensate for large reductions in beam current. The main function of the low power heater is to make small adjustments to maintain the fluid temperature. It is controlled automatically by a commercial temperature controller in a feedback loop.

The cryogenic fluid is recirculated in the cryogenic loop by a high torque cryogenic pump. The pump is located in the upper leg of the target loop in Figure 2.4. It is a vane-axial design with two impellers in series. Each impeller has three blades and is attached to a motor shaft that is immersed in the cryogenic fluid. The pump can displace 4.8 L/s of cryogenic fluid. During pumping, the fluid flows longitudinally in the direction of downstream beam. It flows through the inner cone and back through the area between the walls of the hydrogen cell and the inner cone.

To study the background contribution originating from the aluminum cell windows, two additional targets were instrumented: the aluminum frame and flyswatter. The aluminum frame mimics the entrance window of the hydrogen cell whereas the flyswatter mimics the exit window of the hydrogen cell. The aluminum frame is located 1.7 cm upstream of the entrance window and has a thickness of 0.307 cm. The flyswatter is located 1.0 cm downstream of the exit window and has a thickness of 0.076 cm. A tungsten radiator is used to study the contribution of inelastic electrons due to photo-production and electro-production from the exit window. The tungsten radiator is located 38.5 cm upstream of the flyswatter and has a thickness of 0.00085 cm.

The electron beam heats the target and therefore causes expected boiling and density fluctuations in the liquid. Target boiling can be controlled by the raster. The raster is a two-magnet system which steers the beam with high frequency in a uniform square pattern on the target. The nominal raster size for the backward angle experiment is 1.8 mm x 1.8 mm.

## 2.4 Detectors

For the backward angle measurements, the detector system consists of two arrays of plastic scintillators and an aerogel Cherenkov detector for each of the eight  $G^0$  octants. The two scintillator arrays are a Focal Plane Detector (FPD), which was also used for the forward angle measurements, and a Cryostat Exit Detector (CED). Both the FPD and CED are necessary to determine the electron scattering angle and momentum, thereby providing an adequate separation between elastically and inelastically scattered electrons. The Cherenkov detector is required to reduce the contribution of  $\pi^-$ s, particularly important during running with the deuterium target.

### 2.4.1 Focal Plane Detector

The FPD is composed of eight octants arranged symmetrically around the beamline axis. Four octants were built by a North American collaboration and four were built by a French collaboration. Each octant consists of 16 pairs of arc-shaped plastic scintillators. Each scintillator pair is composed of two identical scintillators, one in front and one in back. Scintillators exploit the molecular excitation produced by the passage of a charged particle. Without a wavelength shifter (WLS), each electron would fall back to its unexcited level, emitting a photon (corresponding to ultra-violet wavelengths) of exactly the correct energy to cause another excitation. The photon would be rapidly reabsorbed by the material. In contrast, when the material is doped with a low concentration of WLS, the ultra-violet photons are converted to longer wavelengths (lower energy) light in the visible, where absorption is significantly reduced.

Each scintillator has two acrylic lightguides, one attached at each end. Coupled to the ends of each light guide is a photomultiplier tube. The lightguide transmits

the light from the scintillator to the photomultiplier tube. It is shaped like a “fish tail” such that it connects from the long thin edge of the scintillator to the circular end of the photomultiplier. The photomultiplier converts the optical signal to an electrical one. It provides a large amount of amplification. Figure 2.6 shows a French FPD octant.

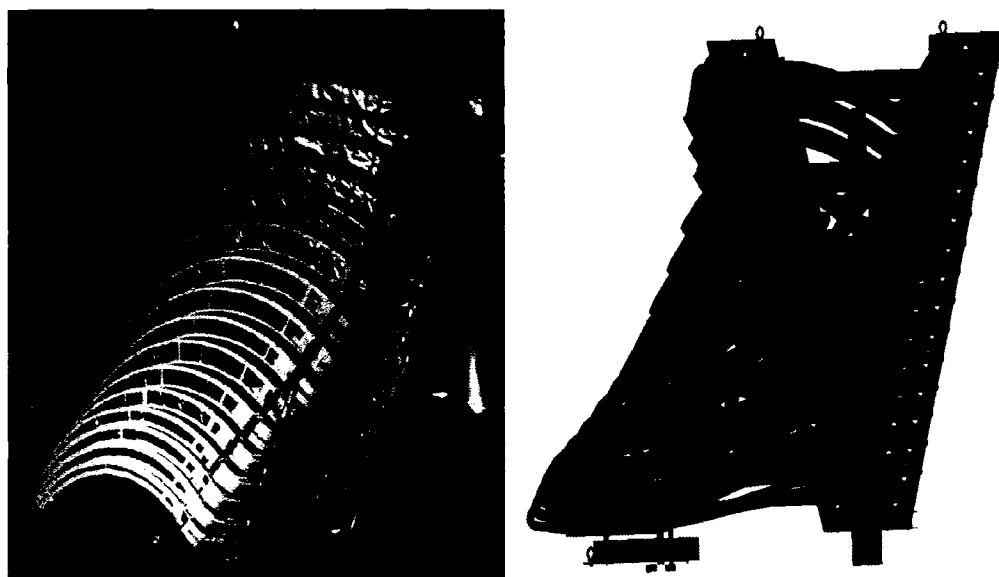


FIG. 2.6: *Pictured on the left is a French FPD octant. Pictured on the right is a schematic of a French FPD octant. The North American octants are similar.*

Within an octant, the scintillator pairs are labeled 1 to 16. Each scintillator has a curved shape, roughly 60-120 cm in length. Scintillator pair 1 is the shortest and is located closest to the target. Scintillator 16 is the longest and is located furthest from the target. Scintillator thickness varies from pair to pair as well. The first four scintillator pairs are 5 mm thick; the remainder have a thickness of 1 cm.

The octants are mounted in a support structure called the Ferris Wheel. Figure 2.7 shows the FPD octants mounted in the Ferris Wheel. The North American octants are located at the 12 o'clock, 3 o'clock, 6 o'clock, and 9 o'clock positions. The French octants are located inbetween the North American octants. The highest

point of the ferris wheel is 7 m above the floor and the symmetry axis is 4 m above the floor.

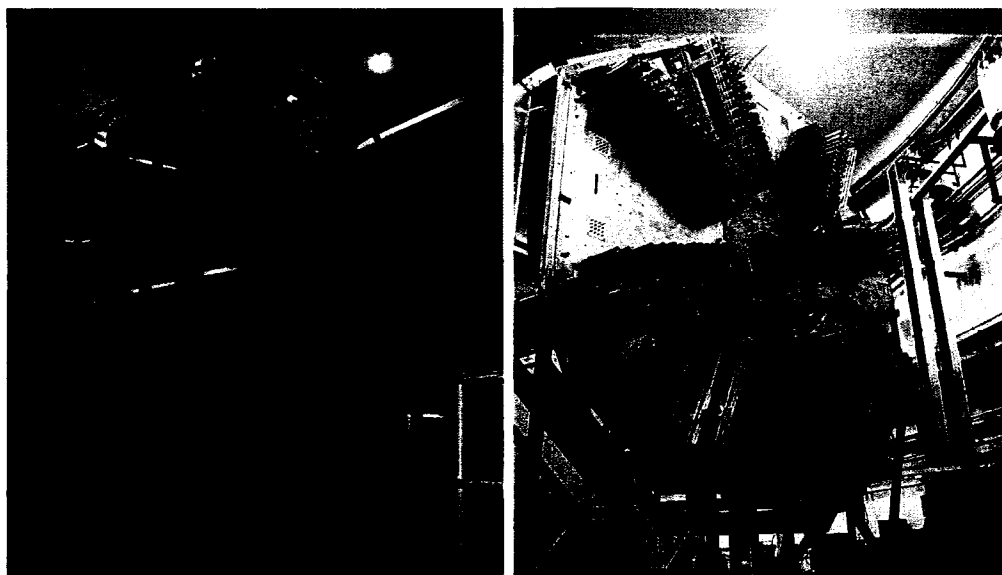


FIG. 2.7:

*The Focal Plane Detector. Pictured on the left is the downstream view. Pictured on the right is the upstream view. In the forward angle experiment, the apparatus is reversed.*

## 2.4.2 Cryostat Exit Detectors

The CED is composed of eight octants, each consisting of nine arc-shaped plastic scintillators, arranged symmetrically around the beamline axis. Like the FPD, each scintillator has two acrylic lightguides, one attached at each end. Coupled to the ends of each light guide is a photomultiplier tube. Figure 2.8 shows the CED octant support structure. It shows the locations of the scintillators, light guides, and PMTs. Also shown is the position of a Cherenkov detector.

Each octant is attached to the outer ring of the ferris wheel at points near the PMTs, where the bulk of the weight of the assembly resides. The octants are





FIG. 2.8:

*The CED octant support structure. Pictured on the left is a schematic of the CED octant support structure. The arc-shaped objects of varying colors are the plastic scintillators. The long blue objects extending from the scintillators are lightguides. The red objects at the ends of the lightguides are photomultiplier tubes. Pictured on the right is an actual CED octant.*

positioned according to cantilevered struts extending from the ferris wheel. The octant support design is integrated with the support structure for the Cherenkov detectors. Figure 2.9 shows the full eight-sectors of the  $G^0$  backward angle setup.

The CED and FPD work in combination to define the momentum and scattering angle of the detected electrons thus allowing for separation of elastic and inelastic events. We record events for every pair of CED/FPD combination and thereby measure asymmetries for both elastic and inelastic events. The construction and assembly of the CEDs is described in Appendix B.

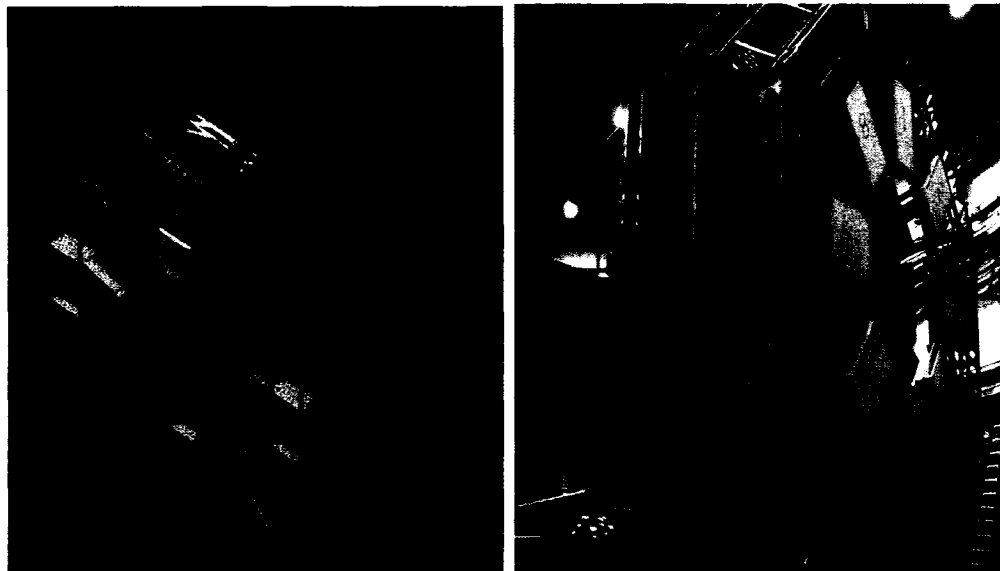


FIG. 2.9:

*The full eight-sectored  $G^0$  backward angle setup. Pictured on the left is a schematic. The top octant shows the full detector arrangement, including the CED, Cherenkov, and FPD. The other octants show only the Cherenkov detectors. Pictured on the right is the actual full detector arrangement.*

### 2.4.3 Aerogel Cherenkov Detectors

Negatively charged pions produce a significant background to the elastic and quasielastic rates detected by the spectrometer. The pions are produced mainly by photoproduction near the Delta resonance. Photoproduction is any reaction initiated by a photon that creates a new particle. The photons that initiate photoproduction primarily come from bremsstrahlung of the beam electrons. Beam electrons passing through material such as target walls, target hydrogen, even beam-line residual gas can undergo bremsstrahlung. Bremsstrahlung is the process by which photons are emitted by an electron or other charged particle slowing down. When an electron interacts with the strong electric field of the atomic nucleus and is consequently accelerated, the electron will radiate electromagnetic energy and lose kinetic

energy. For the case of hydrogen, three photoproduction reactions are possible at our beam energies

$$\gamma + p \rightarrow \pi^+ + n \quad (2.1)$$

$$\gamma + p \rightarrow \pi^0 + p \quad (2.2)$$

$$\gamma + p \rightarrow \pi^- + \Delta^{++} \rightarrow \pi^- + (p + \pi^+). \quad (2.3)$$

A high enough energy photon can produce a  $\pi^-$  via the third reaction. However, this requires that the photon have enough energy to create the rest mass of the pion (135 MeV) plus the extra mass for the  $\Delta^{++}$  (1232 MeV - 938 MeV) = 294 MeV. So the photon would need at least  $135 + 294 = 429$  MeV to produce a  $\pi^-$  at rest. Actually, the photon would need much more energy for the pion to even get out of the target and make its way through the magnetic field and get detected. At our low beam energies at back angles, this is forbidden. However, negatively charged pions are produced due to the presence of neutrons in the aluminum target windows. This reaction is described below.

In the case of the deuterium target, four reactions are possible. Single  $\pi^-$  photoproduction occurs due to the presence of neutrons. The four reactions are

$$\gamma + d \rightarrow \pi^- + p + p \quad (2.4)$$

$$\gamma + d \rightarrow \pi^+ + n + n \quad (2.5)$$

$$\gamma + d \rightarrow \pi^0 + n + p \quad (2.6)$$

$$\gamma + d \rightarrow \pi^- + \Delta^{++} + n \rightarrow \pi^- + (p + \pi^+) + n. \quad (2.7)$$

To eliminate pions across the full momentum range, an aerogel Cherenkov detector was designed. Like both the FPD and CED, the Cherenkov detector is an

eight-sectored array. Its sectors are mounted in conjunction with the CED sectors. Figure 2.10 shows a single Cherenkov detector.

Cherenkov radiation is emitted when a charged particles passes through matter with a velocity  $\nu$  exceeding the velocity of light in the medium,

$$\nu > \nu_t = \frac{c}{n}, \quad (2.8)$$

where  $n$  is the refractive index of the medium,  $c$  is the velocity of light in vacuum, and  $\nu_t$  is threshold velocity. Inside the medium, a charged particle polarizes molecules along its path. The molecules rapidly decay to their ground state, emitting prompt radiation. The emitted light forms a coherent wavefront if  $\nu > \nu_t$ . Cherenkov light is emitted under a constant angle  $\delta$ , with the particle trajectory, given by

$$\cos \delta = \frac{\nu_t}{\nu} = \frac{c}{n\nu} = \frac{1}{\beta n} \quad (2.9)$$

where  $\beta = \nu/c$ . Equation 2.9 has the following two implications. First, for a medium of a given refractive index  $n$ , there is a threshold velocity  $\beta_{min} = \frac{1}{n}$ , below which no radiation takes place. Second, for an ultra-relativistic particle, for which  $\beta = 1$ , there is a maximum angle of emission, given by,

$$\cos \delta_{max} = \frac{1}{n}. \quad (2.10)$$

The Cherenkov medium used in this experiment is an Aerogel. Aerogels were first produced in 1931 from silicon dioxide. They consist of tangled, fractal-like chains of spherical clusters of molecules, each 3-4 nm in diameter. The chains form a structure surrounding air-filled pores that average about 30-40 nm across. Although aerogels are highly porous, the chains are rigid, which gives aerogels considerable mechanical strength. In the 1990s, researchers developed aerogels made from pure carbon. Now, they are made from a variety of materials. The combination of high porosity and extremely small pores provides aerogels with their extreme properties.

Aerogels can have densities as low as  $3 \text{ mg/cm}^3$ . This leads to indexes of refraction as low as 1.01.

The aerogel Cherenkov is comprised of 5 cm of aerogel, through which negatively charged particles must pass through. The aerogel has an index of refraction  $n = 1.03$  such that only particles with a speed where  $\beta > \frac{1}{1.03}$  or  $v > \frac{c}{1.03}$  will produce Cherenkov light. The momentum of a charged pion with this speed is

$$p = \gamma mv = \frac{mv}{\sqrt{1 - \frac{v^2}{c^2}}} = 570 \text{ MeV}/c. \quad (2.11)$$

Hence, pions up to a momentum of 570 MeV/c will not produce any light. In contrast, all primary scattered electrons will produce light.

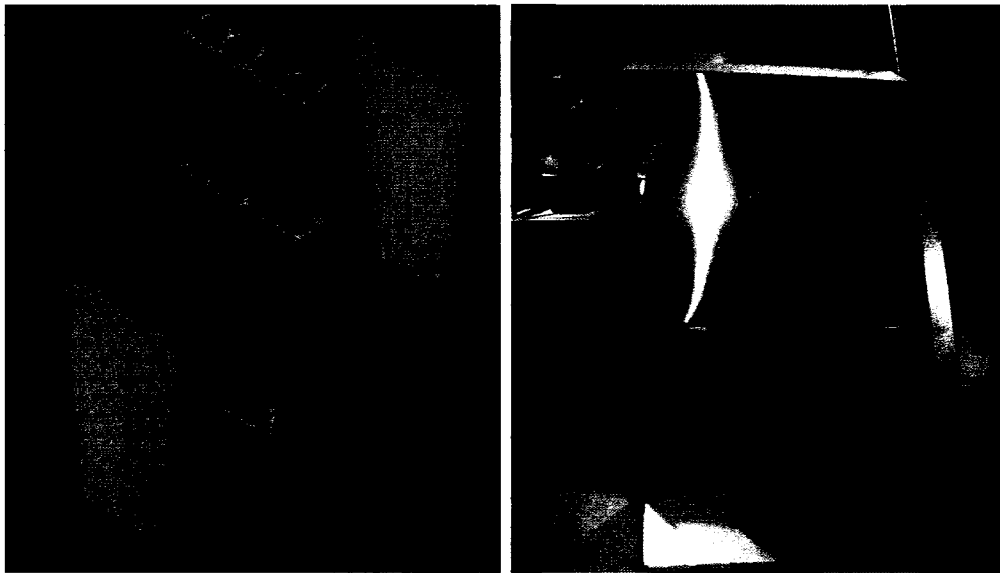


FIG. 2.10:

*The Cherenkov Detector. Pictured on the left is a schematic of a Cherenkov Detector. The pink colored objects are the photomultiplier tubes. Pictured on the right is an actual Cherenkov octant.*

## 2.5 Electronics

A schematic of the North American electronics chain is shown in Figure 2.11. The following is a description of the schematic [53]. The logic of the French electronics is identical. This logic is applicable only for electrons. A similar logic applies for pions except that the Cerenkov logic reversed. In the beginning, each CED is ANDed with the trigger pulse and each FPD is ANDed with the trigger pulse. The trigger pulse provides a small time window to enable the CED-FPD coincidences at the correct time of electron arrival at these detectors and is formed by an OR of all CED's ANDed with an OR of all FPD's. This may seem redundant since the CED and FPD signals generate the trigger. But it is advantageous for the reason that it eliminates some multiple hits by requiring that the CED and FPD signals arrive at the same time as the signals that generated the trigger. Next, a copy of each (CED<sub>in</sub> and FPD<sub>in</sub>, meaning in-time) is sent to two logic functions: MH and 8-bit word encoder. The MH or Multiple Hit function determines if there is a multiple hit event (meaning more than one CED or more than one FPD fires on a given beam pulse). The 8-bit word encoder generates an 8-bit word. Four bits correspond to the CED information and four bits correspond to the FPD information. The first four bits contain the FPD while the second four bits contain the CED. If there is no multiple hit event, then the 8-bit word is allowed to proceed through the electronics chain to the decoding boards. The LATCH function takes each of the 8-bits in the 8-bit word and stores them in when the AND of the Cerenkov and trigger pulse sets the latch. This ensures that it was in fact an electron which fired both the CED and FPD involved in the coincidence. When the LATCH is set, the 8-bit word is sent to a DECODING function, which “unpacks” the 8-bit word into individual CED-FPD coincidence signals. A delayed version of the trigger pulse then clears the LATCH to make it ready to accept the next event. The MH bit is also sent to another logic

board, the MHIT board, which takes the CEDin and FPDin and forms ANDs with the MH bit to count how many times each CED and/or FPD were involved in a MHIT event.

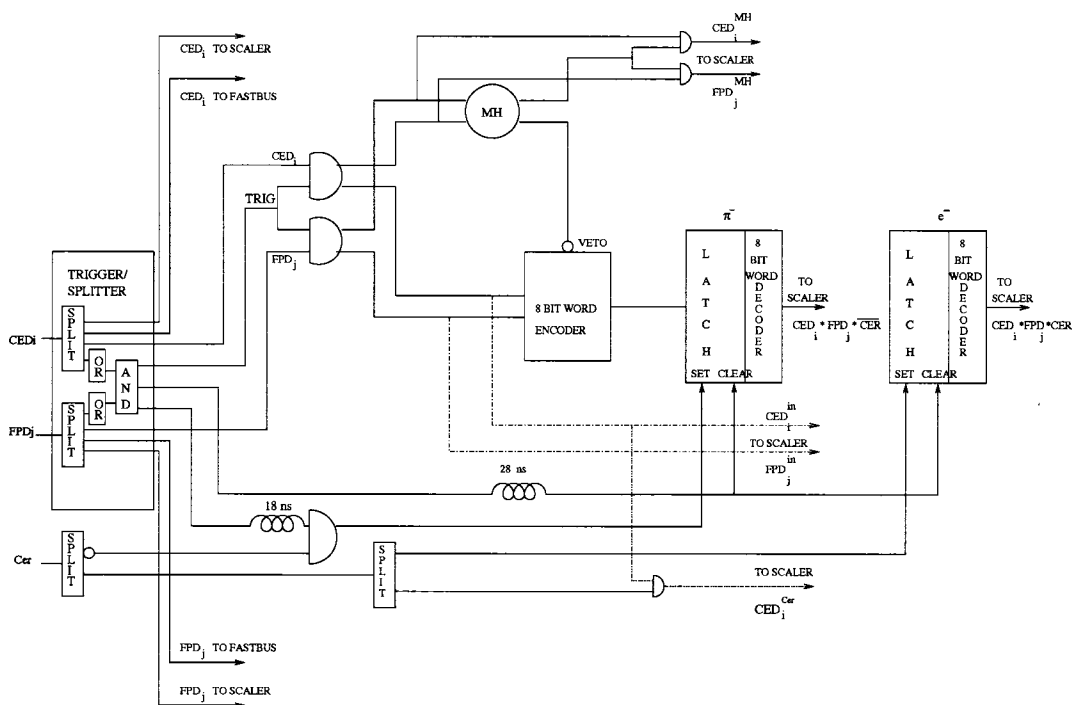


FIG. 2.11:  
*North American electronics chain [53].*

## 2.6 Beam Instrumentation

As will be discussed later, the parity-violating asymmetry is sensitive to helicity-correlated fluctuations in the beam parameters. Therefore, the helicity-correlated fluctuations of the electron beam must be minimized to reduce false asymmetries. Herein, we describe the various devices used to monitor the helicity-correlated properties of the electron beam.

### 2.6.1 Beam Current Monitors

The Beam Current Monitor (BCM) [54] is designed for stable, low noise beam current measurement. It consists of a Parametric Current Transformer called an Unser monitor, two resonant cavities, the associated electronics and a data acquisition system. The two cavities are positioned before and after the Unser and are called downstream and upstream cavities, respectively. The downstream cavity is closest to the target. The cavities and the Unser monitor are enclosed in a box to improve magnetic shielding and temperature stabilization.

The Unser is an absolute monitor. It is a toroidal transformer designed to make a direct measurement of the actual intensity of the beam current. Though it is very accurate at high currents, it cannot be used during normal operations due to its unstable offset. In contrast, the cavities are relative monitors and are stable and linear over the entire dynamic range. The cavities are calibrated with the Unser at high currents and used continuously during the experiment.

The resonant frequency is adjusted to the 1497 MHz frequency of the CEBAF beam. This is done by a stub tuner mounted on a micrometer that is moved in and out of the cavity. A magnetic field probe is located inside the cavity body on the circumference, where the electrical field is minimum and the magnetic field is maximum. The probe is coupled to one of the resonant modes of the cavity and couples the beam signal out of the cavity. When the electron beam passes through the cavity, it excites a transverse electromagnetic mode. The probe loop provides an output signal proportional to the current. Figure 2.12a is a BCM in the beamline and Figure 2.12b is a diagram of a cavity, showing the micrometric screw and antenna.



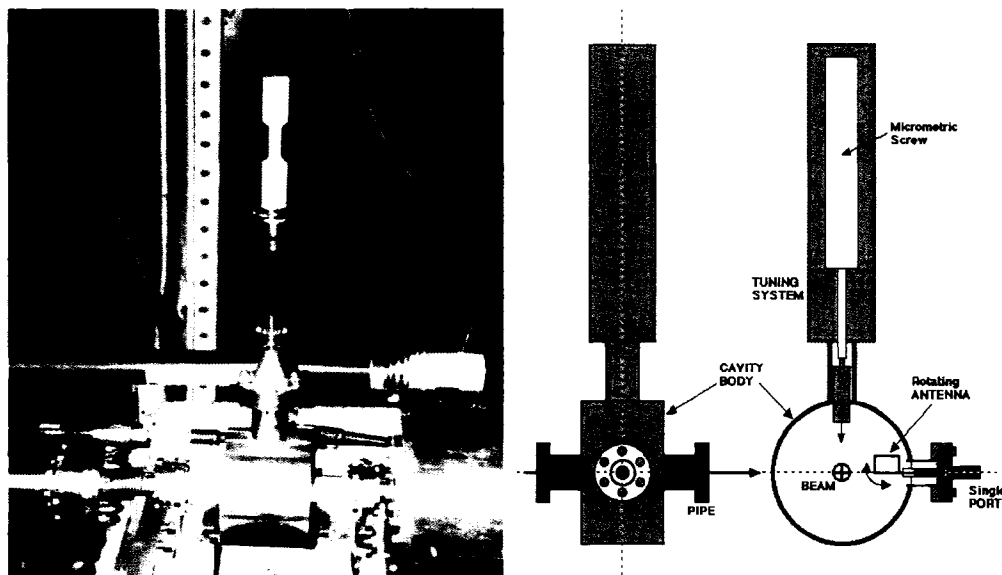


FIG. 2.12: Pictured on the left (a) is a BCM resonant cavity installed in the beamline. Pictured on the right (b) is a schematic of a BCM resonant cavity, showing the micrometric screw and antenna.

## 2.6.2 Beam Position Monitors

A stripline Beam Position Monitor (BPM) is a device used for measuring vertical and horizontal beam position (and intensity). It consists of a 4-wire antenna array of open-ended wire striplines tuned to the fundamental frequency 1497 MHz frequency of the CEBAF beam. The striplines run along the inside length of the cylinder. Figure 2.13 is a diagram of a BPM, showing the four striplines. As the beam passes through the center of the cylinder, it induces currents on each of the striplines. Signals from the top and bottom striplines determine vertical beam position while signals from the left and right striplines determine the horizontal beam position. If the beam is closer to one stripline than another, then more current will be induced on that stripline. The relative magnitude of the signals from the striplines is used to determine the position of the center of mass of the beam. A larger beam current will create a larger current on both striplines. For this reason

the position monitors can also be used to measure the beam intensity. Beam position monitors are permanently installed fixtures in the beam transport lines. Since the beam does not have to hit any part of the detector to create a signal, a BPM can be left in place all of the time.

For BPMs oriented at  $0^\circ$ , the  $X$  and  $Y$  beam positions are calculated according to

$$X = \frac{X_+ - X_-}{X_+ + X_-}, \quad (2.12)$$

where the subscript  $+(-)$  represents the plus(minus) antenna.

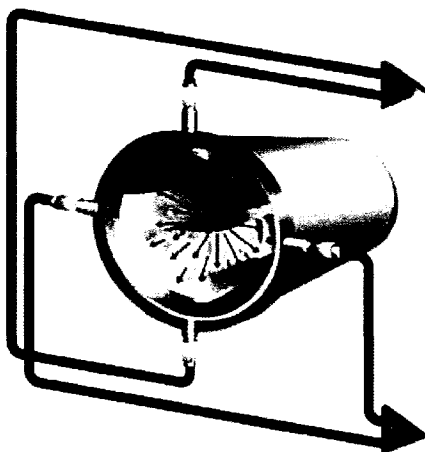


FIG. 2.13: *Diagram of a BPM, showing the four striplines along the inside length of the cylinder.*

A measurement of the position resolution of the BPMs was done according to the “three-BPM method” as explained in [78]. This technique assumes a linear correlation  $x_3 = ax_1 + bx_2 + c$  between three beam positions  $x_1$ ,  $x_2$ , and  $x_3$  at three neighboring BPMs, where  $a$ ,  $b$ , and  $c$  are constants. It applies a least-squares analysis to sets of  $(x_1, x_2, x_3)$  measured by these three BPMs to obtain  $a$ ,  $b$ , and  $c$ . The position resolution is the residual between the measured and calculated beam position at the third BPM. For this analysis, BPMs H00A, H00B, and H00C

were used. From the least-squares fit,  $a = -0.86$ ,  $b = 1.91$ , and  $c = -3.28$ . The correlation plot between the measured and calculated beam positions at H00C is shown in Figure 2.14. The data points are fitted to a line and the fit parameters are displayed in the statistics box. The parameters  $p0$  and  $p1$  are the intercept and slope, respectively. A histogram of the residual between the measured and calculated beam positions at H00C is shown in Figure 2.15. The histogram is fitted to a Gaussian which gives a sigma of about  $2.4 \mu\text{m}$ . This represents a convolution of the intrinsic resolution of the three monitors.

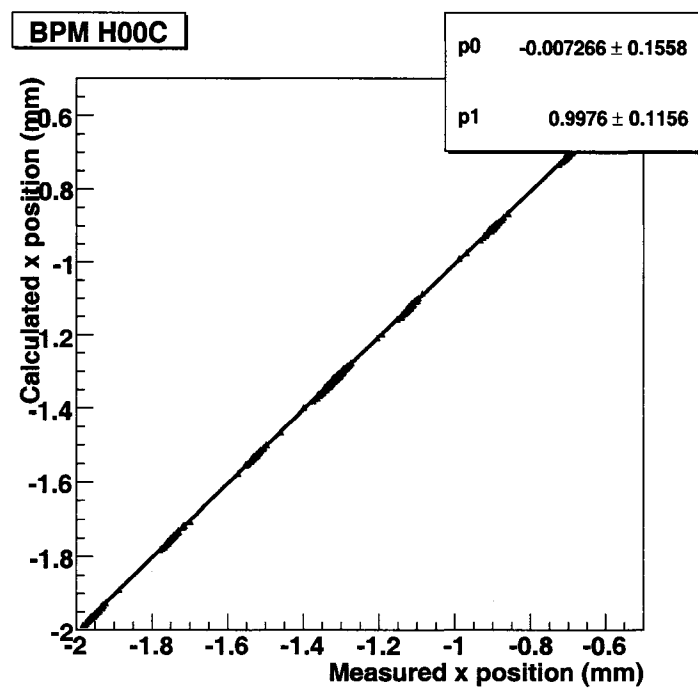


FIG. 2.14:

*The correlation plot between the measured and calculated beam positions at H00C, where the calculation is based on data from BPMs H00A and H00B (see text).*

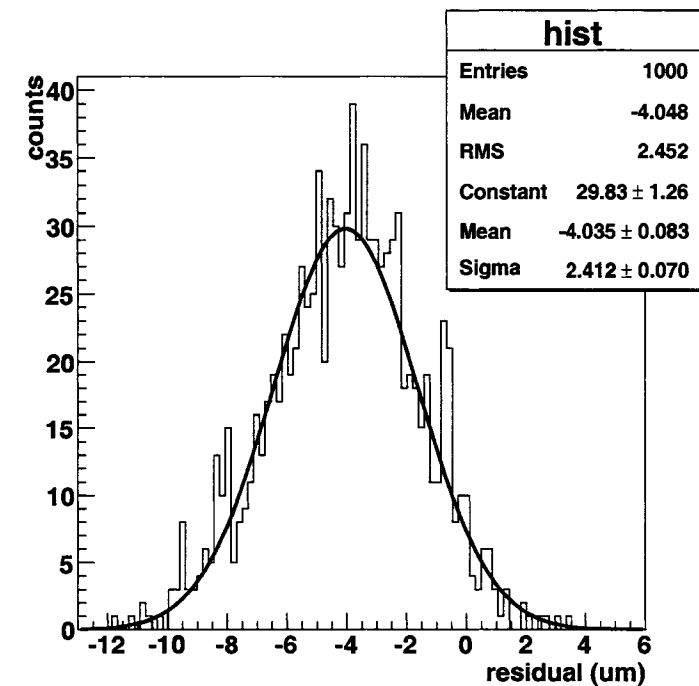


FIG. 2.15:

*A histogram of the residual between the measured and calculated beam positions at H00C.*

### 2.6.3 Halo Monitors

Electrons outside the core of the electron beam compose the beam halo. Beam halo is caused by a variety of processes [55]. These processes include scraping of the electron beam against the beam pipe, scattering of the electron beam against stray gas in the beam line enclosure, self-interaction of the electron beam, and scattering of the laser beam against the photocathode in the electron source. Beam halo interferes with the experiment in two primary ways. First, it increases the singles rates or background radiation in the detectors. Consequently, the lifetime of the photomultiplier tubes is decreased and the dead time in the detectors is increased. Second, it interacts with the target cell walls. As a result, the number of inelastic electrons measured is increased. We monitor beam halo to ensure that it stays

within the experiment's specifications and in order to actively minimize it. The requested limit for the halo is 1 part per million (ppm) of the main beam outside a 3 mm radius.

Beam halo is measured using a hole in a 2 mm thick sheet of carbon, called a halo target, through which the beam passes. If the main beam is steered correctly, it will pass unaffected through the center of the target. The halo surrounding the beam will scrape against the target sides and create a shower of particles to be detected. The target is mounted on an apparatus that enables easy transitions in and out of the beam. One halo target has a 3 mm radius and the other halo target has a 5.5 mm radius. The radius of the smaller target is at the requested halo limit so it serves as a spot check. The larger target is used to check the size of the halo on a continuing basis. The halo targets are shown in Figure 2.16a.



FIG. 2.16: Pictured on the left (a) are the halo targets. The top hole is the smaller target with a 3 mm radius. The bottom hole is the larger target with a 5.5 mm radius. Pictured on the right (b) is halo 4 installed on the halo girder in Hall C. It is shielded from the beam line with blue lead blocks.

There are two halo monitors in the alcove at the entrance to Hall C, Halo 1 and

Halo 2. There are two halo monitors immediately after the halo target at about a  $15^\circ$  angle, Halo 3 and Halo 4, and four more downstream at very forward angles: Halo 5, Halo 6, Halo 7, and Halo 8. The locations of these monitors on the beamline are shown in Figures 2.17 and 2.18. The halo monitors are bare photomultiplier tubes (PMTs) or PMTs attached to scintillator or lucite. Halo 1 and Halo 2 are bare photomultiplier tubes. Halo 3, Halo 4, Halo 7, and Halo 8 are Lucite detectors. Halo 5 and Halo 6 are scintillator detectors. Each halo is shielded with lead. Figure 2.16b shows halo 4 installed on the halo girder in Hall C.

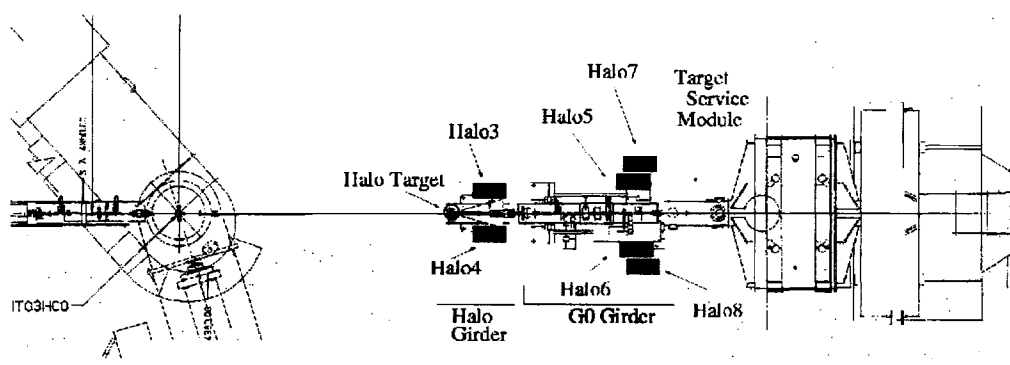


FIG. 2.17: An overhead schematic of the location of the halo monitors on the girder.

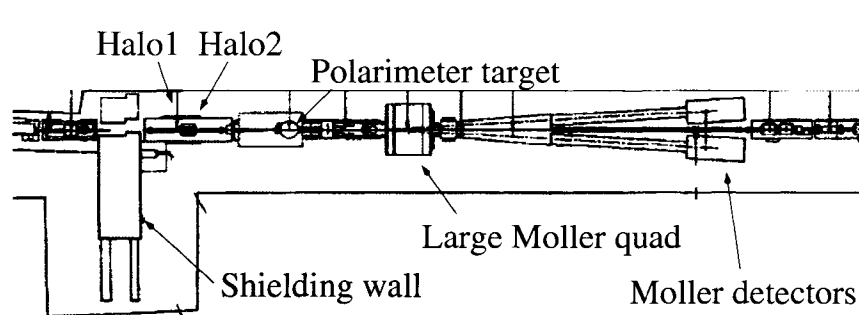


FIG. 2.18: A side schematic of the location of the halo monitors in the alcove.

The normalized halo yields are plotted as a function of run number and fitted

to a flat line in Figure 2.19. The parameter  $p_0$  is the mean and is displayed in a statistics box at the top of each plot. The smaller rates in Halos 7 and 8 stem from the fact that they are made of lucite while the other halo monitors are made of scintillator. In scintillators, the production of light is governed by molecular excitation (see Section 2.4.1). In contrast, the production of light in lucite relies on Cerenkov radiation (see Section 2.4.3). For the same charged particle going through a scintillator, much more light is produced.

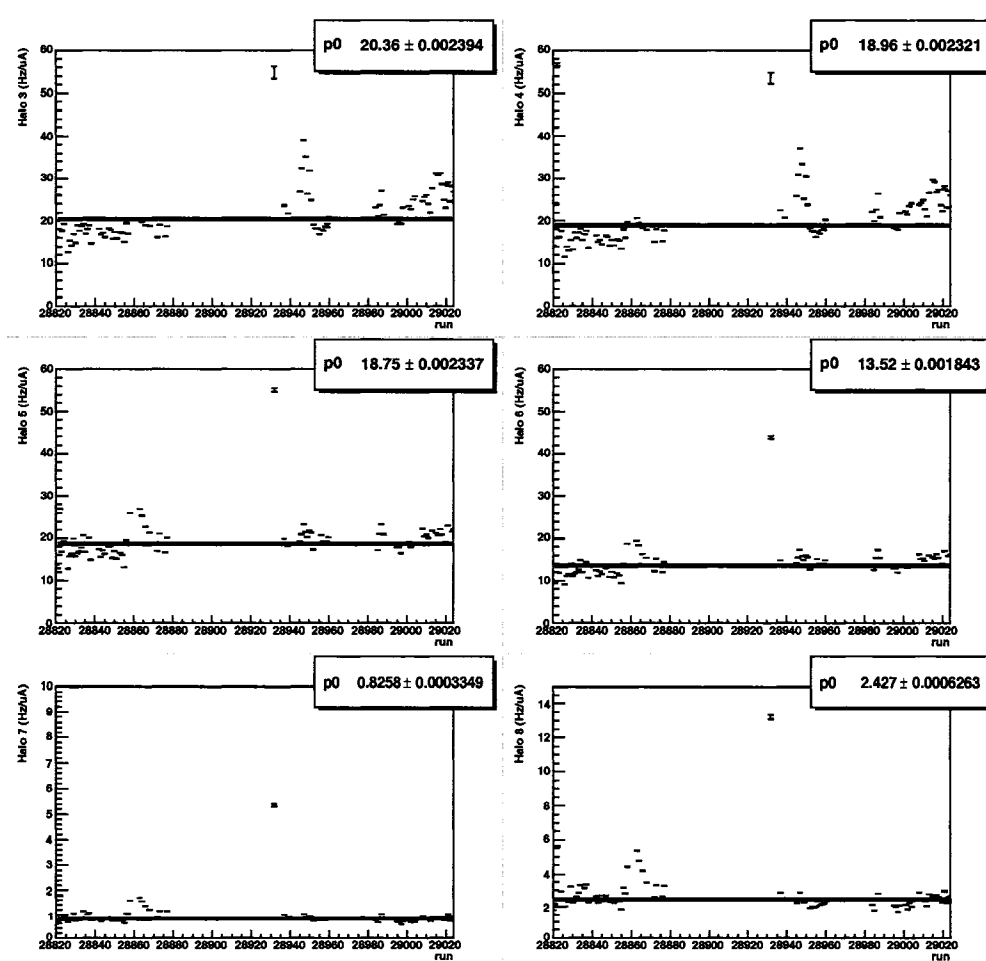


FIG. 2.19: Halo yields over the duration of the run. Some periods of poor beam quality (large halo) are apparent.

Condition	halo 3	halo 4	halo 5	halo 6	halo 7	halo 8
5.8 nA on frame	450 kHz	430 kHz	2.7 MHz	2.4 MHz	1.8 MHz	3.1 MHz
No halo targ (40 $\mu$ A)	190 Hz	150 Hz	185 Hz	120 Hz	3 Hz	12 Hz
3 mm targ (40 $\mu$ A)	1000 Hz	1017 Hz	3600 Hz	2700 Hz	360 Hz	1020 Hz
Halo Fraction	0.26	0.29	0.18	0.16	0.029	0.047

TABLE 2.1: Halo measurements to determine if the halo specification is 1 ppm of the main beam, outside a 3 mm radius, is achieved. Measurements include putting 5.8 nA of beam directly into the 2 mm thick part of the carbon halo target frame, sending 40  $\mu$ A of beam through halo target with a 3 mm radius, and sending 40  $\mu$ A of beam unobstructed (no halo target) through the beamline. The halo fraction is the fraction of main electron beam that is outside a 3 mm radius. Fractions are given in ppm.

We measured a halo that is less than 0.29 ppm of the main beam outside a 3 mm radius. This is less than our specification limit of 1 ppm. To calculate this halo, we performed three tests. First, we put 5.8 nA of beam directly into the 2 mm thick part of the carbon halo target frame. Second, we sent 40  $\mu$ A of beam through the smaller halo target with a 3 mm radius. Third, we sent 40  $\mu$ A of beam unobstructed (no halo target) through the beamline. For each test, we measured the rate of each halo monitor. Table 2.1 lists the rate of each halo monitor at the three beam conditions as well as the halo fractions. The halo fractions are determined according to

$$fraction = \frac{rate_{3\text{ mm}} - rate_{no\text{ target}}}{rate_{5.8\text{ nA}}} \times \frac{5.8\text{ nA}}{40\ \mu\text{A}}. \quad (2.13)$$

#### 2.6.4 Lumi Monitors

The physics of target density fluctuations in high-power cryotargets is complex [56]. Inside the target, the flow is expected to be highly turbulent and spatially dependent along the length of the target cell. When the liquid phase warms, the local density changes. Boiling is associated with a large local density change and is inhomogeneous across the cell. It likely starts at the surfaces of the heated target windows. The rate by which heat is conducted away from the windows depends



on whether the boiling is nucleate (bubbles) or makes a transition to film boiling (where the window is in contact with vapor rather than liquid).

Luminosity detectors (LUMIs), downstream of the  $G^0$  target, are used to monitor target density fluctuations and helicity-correlated beam properties. The LUMIs are quartz Cherenkov detectors and have PMTs to amplify their signals. Lumis 1-4 were put at  $45^\circ$  with respect to the vertical and horizontal axes while Lumis 5-8 were placed horizontally and vertically as shown in Figure 2.20. The LUMIs were placed in 0.159 cm thick aluminum cups which intrude radially into the downstream beam pipe as illustrated in Figure 2.21.

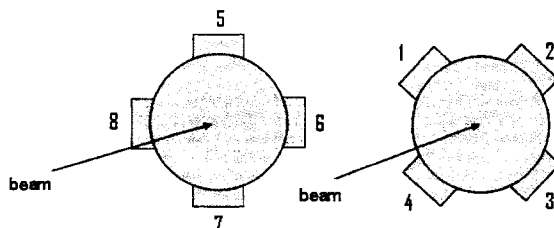


FIG. 2.20: *Cross-section schematic of lumis in downstream beam pipe. Lumis 1-4 were put at  $45^\circ$  with respect to the vertical and horizontal axes while Lumis 5-8 were placed horizontally and vertical [57].*

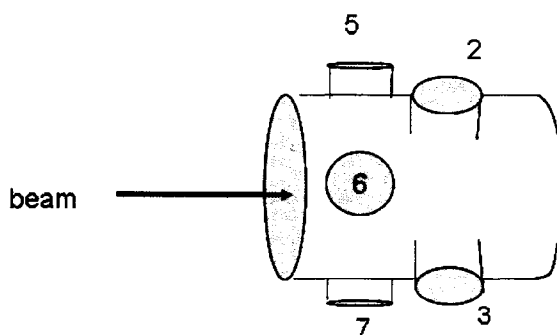


FIG. 2.21: *Side view schematic of lumis in downstream beam pipe [57].*

The LUMIs detect scattered electrons which originate from elastic electron-

proton scattering and polarized Moller (electron-electron) scattering. Both processes contribute about half of the total electron rate. The LUMIs have three advantages. First, because of their smaller scattering angle, the LUMIs have a higher counting rate than the FPDs and CEDs. Therefore, they measure asymmetries with higher precision than the FPDs and CEDs. Second, the LUMIs can detect electron scattering rates from small beam currents that BPMs and BCMs cannot detect. Hence, the LUMIs can be used to measure leakage of electron beam intended for the other halls. Third, the physics asymmetry is smaller, making the LUMIs more sensitive to false asymmetries.

### 2.6.5 Polarimetry

Consider scattering where the scattering probability is dependent upon the spin orientation of the incident electron. The scattering probability consists of a spin independent piece  $S_0$  and a spin dependent piece  $AS_0$ , where  $A$  is the spin sensitivity of the scattering process, which is called the analyzing power. The probability of scattering an electron with positive spin is  $S_+ = S_0(1 + A)$  while the probability of scattering an electron with negative spin is  $S_- = S_0(1 - A)$ . Next, consider scattering of an electron beam with polarization

$$P = \frac{n_+ - n_-}{n_+ + n_-}, \quad (2.14)$$

where  $n_+$  and  $n_-$  are the number of electrons with positive and negative spin projections, respectively. Solving Equation 2.14 for the  $n_+$  and  $n_-$  gives

$$n_+ = \frac{n_0}{2} (1 + P) \quad (2.15)$$

$$n_- = \frac{n_0}{2} (1 - P), \quad (2.16)$$

where  $n_0 = n_+ + n_-$ . When the beam polarization is positive, the counting rate of scattered electrons is

$$R_+ = S_+n_+ + S_-n_- = S_0(1+A)(1+P)\frac{n_0}{2} + S_0(1-A)(1-P)\frac{n_0}{2}. \quad (2.17)$$

Similarly, when the beam polarization is negative, the counting rate of scattered electrons is

$$R_- = S_+n_- + S_-n_+ = S_0(1+A)(1-P)\frac{n_0}{2} + S_0(1-A)(1+P)\frac{n_0}{2}. \quad (2.18)$$

It follows that the counting rate asymmetry is

$$\frac{R_+ - R_-}{R_+ + R_-} = AP. \quad (2.19)$$

This is a key equation. By measuring the difference in the counting rates (and with knowledge of the analyzing power of the scattering process), one can measure the magnitude of the polarization.

### Moller Polarimeter

The polarization of the electron beam arriving in Hall C is measured by the Hall C Moller polarimeter [58]. Moller polarimeters are based on  $\vec{e} + \vec{e} \rightarrow e + e$  scattering. For both longitudinally polarized beam and target electrons, the cross-section in the center of mass frame is

$$\frac{d\sigma}{d\Omega} = \frac{d\sigma_o}{d\Omega} [1 + P_t P_b A_{zz}(\theta)], \quad (2.20)$$

where  $P_b$  and  $P_t$  are the longitudinal polarization of the beam and target, respectively,  $A_{zz}$  is the analyzing power, and  $\frac{d\sigma_o}{d\Omega}$  is the unpolarized cross-section. The unpolarized cross-section is

$$\frac{d\sigma_o}{d\Omega} = \frac{\alpha(4 - \sin^2 \theta)}{2m_e \gamma \sin^2 \theta}, \quad (2.21)$$

where  $\theta$  is the scattering angle in the center-of-mass frame. The analyzing power is given by

$$A_{zz}(\theta) = -\sin^2\theta \frac{8 - \sin^2\theta}{(4 - \sin^2\theta)}. \quad (2.22)$$

The beam polarization can be measured by comparing the cross-section asymmetry for beam and target spins aligned parallel and anti-parallel

$$A_{Moller} = \frac{\frac{d\sigma^{\uparrow\uparrow}}{d\Omega} - \frac{d\sigma^{\uparrow\downarrow}}{d\Omega}}{\frac{d\sigma^{\uparrow\uparrow}}{d\Omega} + \frac{d\sigma^{\uparrow\downarrow}}{d\Omega}} = P_t P_b A_{zz}(\theta). \quad (2.23)$$

At  $\theta = 90^\circ$ , the analyzing power is a maximum ( $A_{zz} = -7/9$ ). Therefore, the kinematics are chosen such that  $\theta = 90^\circ$ . The electrons in the Moller target are polarized upstream so  $P_t$  is a positive number. Therefore, since the Moller asymmetry  $A_{Moller}$  is negative, the beam polarization  $P_b$  must be positive.

There are three primary sources of error in the measurement. These include achievable statistics, uncertainties due to background from Mott scattering, and the error in determining the target electron polarization.

The layout of the polarimeter is shown in Figure 2.22. The incoming electron beam is directed onto the Moller target, a thin foil of pure iron. Pure iron was selected for the reason that its electron polarization is known with great accuracy in saturation. The foil is oriented perpendicular to the beam and magnetized using a superconducting solenoid producing a 4T field in the direction of the beam. Both the scattered and recoiling target electrons emerge in the horizontal plane and are focused by a quadrupole magnet Q1. Collimators are used to select the desired scattering angles. A second quadrupole magnet Q2 defocuses the electrons. The electrons are detected in coincidence using two symmetrically placed hodoscope counters and lead-glass detectors.

The Moller measurement is an invasive measurement since it requires beam current less than  $2 \mu\text{A}$ . Under high beam current, the iron target will heat up and the electrons will depolarize.

The Moller Polarimeter was designed to operate at beam energies ranging from 1 GeV to 6 GeV. In this range, the Moller provides an absolute polarization measurement with accuracy better than 0.5%. In order to accommodate lower energies for this experiment, the optics of the Moller Polarimeter had to be adjusted.

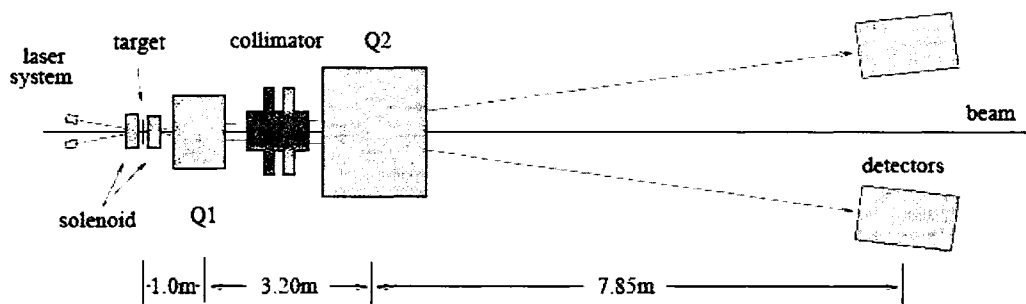


FIG. 2.22: *The layout of the Hall C Moller Polarimeter [58].*

### Mott Polarimeter

The polarization of the electron beam is also measured by the Mott Polarimeter in the Injector. Mott polarimetry is based on the scattering of polarized electrons from an unpolarized high-Z nucleus [59]. The analyzing power for Mott scattering from single free-atoms is called the Sherman function and is calculated from QED. It depends upon the laboratory scattering angle and electron energy. The kinetic energy of the electron beam at the Mott polarimeter is between 2 and 8 MeV [60]. To prevent any spread of the electron beam in air, the scattering target is enclosed in a vacuum vessel. The polarimeter's stainless steel chamber is connected directly to the beam line and can be operated by opening a metal valve. During a polarization measurement, a 12.5 degree dipole bend magnet is energized to guide the electron beam to the polarimeter target. The electrons enter the chamber from the left side of Figure 2.23 and hit the center of the target with a precision of 0.5 mm and an

angle of less than 2 mr. The target is mounted on a moving ladder that allows the selection of 17 different targets. The standard target is a 1  $\mu\text{m}$  gold foil. The polarimeter has four electron detector arms, two in the horizontal plane and two in the vertical plane. Each member of a pair is separated by  $180^\circ$  in the azimuth. An adjustable aluminum collimator inside the vacuum chamber defines the acceptance of the individual detector arms and assures that each detector sees only the central area of the target.

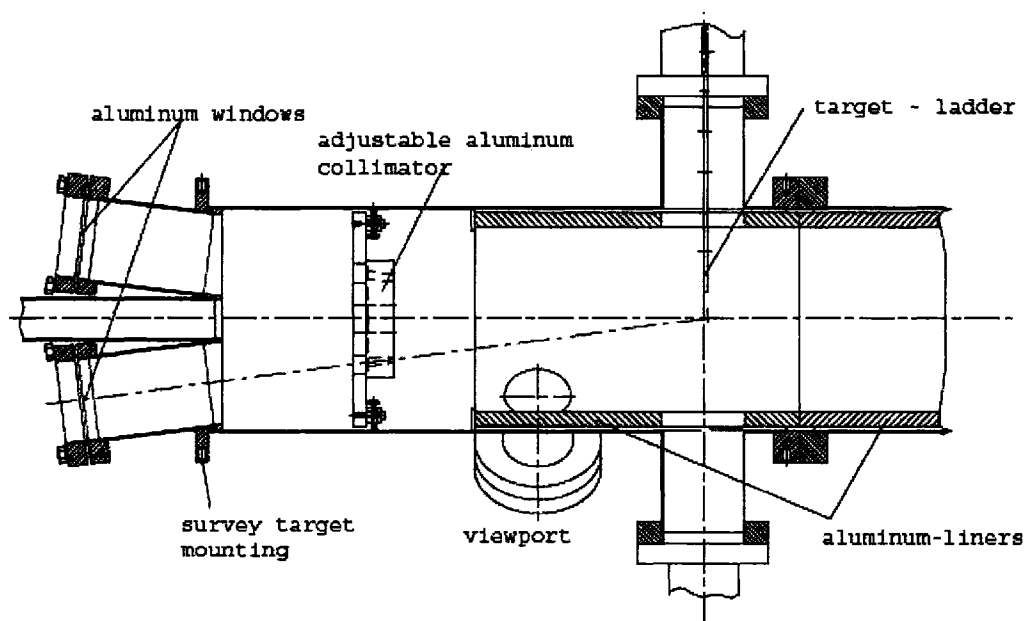


FIG. 2.23: *Cross section through the MeV Mott polarimeter [60].*

### 2.6.6 Coil Modulation

To measure and correct for systematic errors associated with helicity correlated changes in beam position, angle, energy, and intensity, a beam modulation (a.k.a “coil pulsing”) system was used to intentionally dither the beam by large amounts [43]. The beam position and angle are varied by corrector coils in the beam line

leading to the hydrogen target and the energy is driven by a cavity in the South Linac. The measurements are performed concurrently with experimental data taking during the first three minutes of a run. The amplitude of the modulation needs to be large enough to permit accurate measurements but small enough not to steer the beam beyond safe limits. If the beam is steered beyond safe limits, it could trip the accelerator and beam pipe or other equipment can be damaged. Figure 2.24 shows a typical dither cycle. During the three minutes of coil modulation, there are eleven cycles: 3  $x$ , 3  $y$ , 4 energy, and 1 empty. Each cycle is made up of 9 different settings. Therefore, a coil sits at one setting for about 2 seconds.

The change of the beam energy is calculated based on the  $x$  position of the beam measured by BPM 3C12 at the dispersive point in the Hall C arc. This BPM has a calibration of 1%/4 mm.

Table 2.2 summarizes the approximate ranges of motion for a typical run in both natural beam motion and coil modulation. The  $x$  range for coil modulation is more than two times bigger than the  $x$  range for natural beam motion. In contrast, the  $y$  range for coil modulation is more than three times smaller than the  $y$  range for normal beam motion. Since coil modulation is an intentional dithering of the beam by large amounts, both the  $x$  and  $y$  ranges for coil modulation should be larger than (or at least equal to) the  $x$  and  $y$  ranges for natural beam motion. During the  $y$  cycle, there is significant scraping at both lower and upper limits. This is clearly a mistake on our part and may be the result of incorrect coil modulation settings or improper placement of the coils in the Hall C line. To eliminate scraping, a halo cut ( $< 60 \text{ Hz}/\mu\text{A}$ ) was implemented only during coil modulation. Also, it should be noted that charge is not deliberately modulated during coil modulation. One advantage of coil modulation is that it can be used to decouple charge from the other beam properties.

	natural beam motion	coil modulation
$x$ (mm)	0.3	0.5
$y$ (mm)	0.6	0.2
$\theta_x$ (mrad)	0.016	0.03
$\theta_y$ (mrad)	0.03	0.01
$Q$ (nC)	200	35
$\Delta E$ (MeV)	0.06	0.2

TABLE 2.2:

*Range of motion for a typical run (29023) for both natural beam motion and coil modulation.*

## 2.7 DAQ

The data stream consisted of two different types of events: high statistics data counting and low statistics monitoring data (Fastbus). The high statistics data counted all particles detected within each  $\frac{1}{30}$  s macropulse period. The low statistics monitoring data included ADC and TDC spectra for each PMT on each detector with a maximum event rate of 1 kHz. A Time to Digital Converter (TDC) module records the time difference between a start and stop signal. An Analog to Digital Converter (ADC) module produces a digital code at its output that is proportional to an analog charge supplied accumulated at its input.

The data acquisition system (DAQ) used by the  $G^0$  experiment was CODA (CEBAF Online Data Acquisition system) [61]. CODA was developed at JLab and ran on a Linux computer in the counting house. The DAQ computer communicated with crates containing the electronics modules for different sub-systems. Each crate had a single board computer called the readout controller (ROC) by which the DAQ computer communicated. In total, there were 11 ROCs. Table 2.3 summarizes the function of the ROCs.

There were two types of triggers: 30 Hz and Fastbus. For the 30 Hz trigger, all of the ROCs are read out at the end of each macro-pulse trigger (see Section 3.3). This formed the data stream for asymmetry computation. The Fastbus trigger is



ROC	Function
ROC0	trigger supervisor and beamline scalers
ROC1	NA scaler data
ROC2	NA scaler data, NA ARS
ROC3	French DMCH-16X modules
ROC4	NA scaler data
ROC5	fastbus monitoring electronics
ROC7	French CED-FPD board
ROC8	French Cerenkov modules, French ARS
ROC9	NA singles
ROC31	injector electronics

TABLE 2.3: *ROCS and their functions [62].*

controlled by a fast-clear. When the fast-clear is enabled, the Fastbus trigger checks for two mean-timer hits. It requires that a CED and FPD both fire within the coincidence window during the “fast-clear gate”. The signal used to indicate that there has been a valid CED and FPD hit is identical to the trigger signal used by the coincidence electronics. If an event is empty or has only one mean-time hit, the ADC/TDC are cleared and reset. The DAQ only reads out events that are filled. When the fast-clear is disabled, the Fastbus trigger is “free-running”. In other words, most of the time, events are empty. Consequently, the DAQ takes time to digitize and readout empty events and statistics are poor.

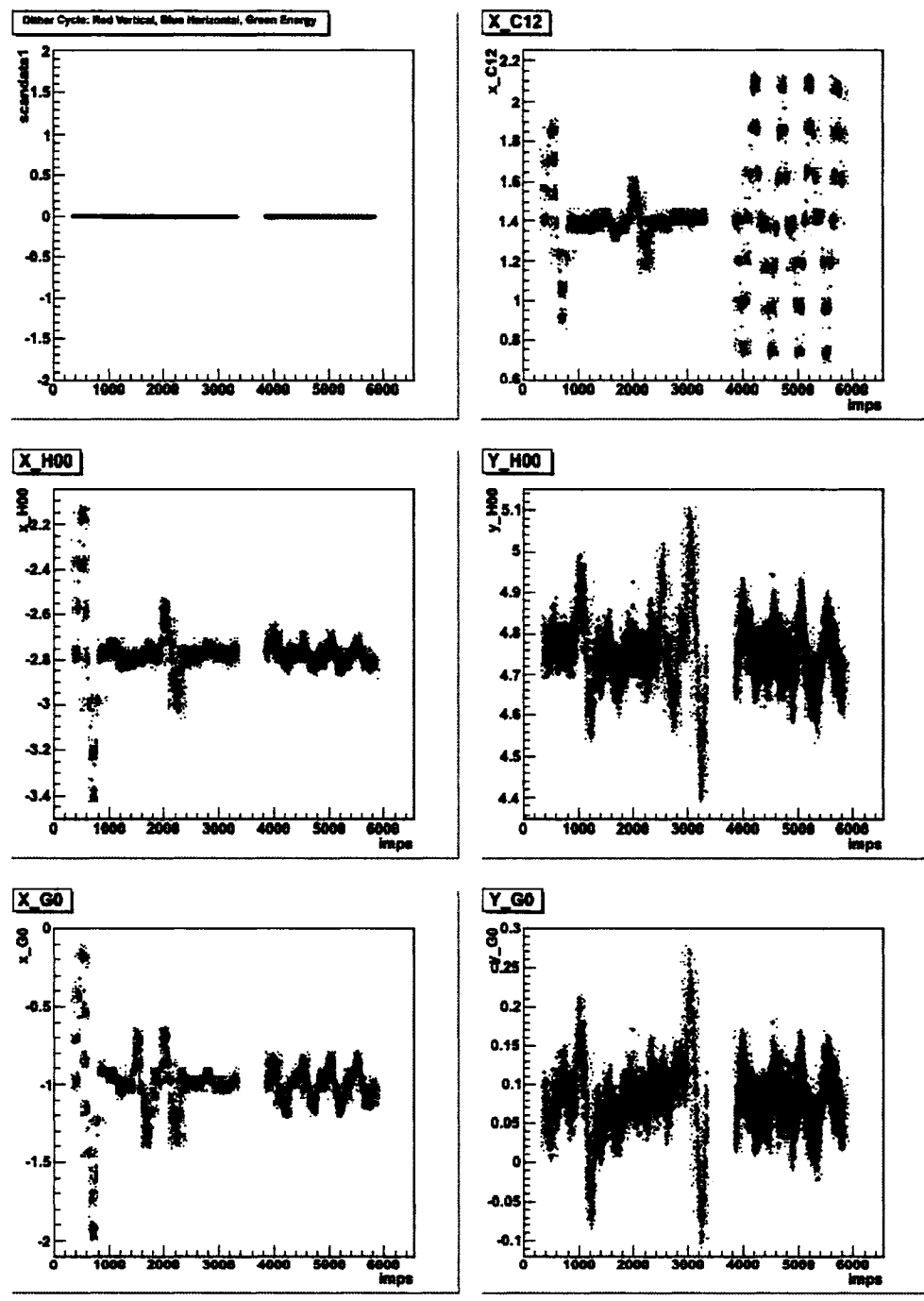


FIG. 2.24: A coil modulation cycle from run 29015. The red line corresponds to a vertical pulse, the blue line corresponds to a horizontal pulse, and the green line corresponds to an energy pulse. BPM C12 is located at the dispersive point in the Hall C arc (point of maximum dispersion in the arc). The change of the beam energy is calculated according to the  $x$  position of this BPM. BPMs H00 and G0 are located upstream and downstream, respectively, of the standard pivot center of the hall.

# CHAPTER 3

## The Polarized Electron Source

The polarized electron source plays a critical role in the experiment, being the origin of helicity-correlations in beam parameters which contribute to systematic errors in the measurement of the parity-violating asymmetry. To control these effects, helicity-correlations in the polarized electron source are minimized according to experimental techniques described in this Chapter.

### 3.1 CEBAF Accelerator

The CEBAF accelerator is a five-pass recirculating linac capable of simultaneous delivery of continuous-wave beams to three end stations. A schematic of the CEBAF accelerator is shown in Figure 3.1. It consists of an Injector, two linear accelerators connected by recirculation arcs, and an Extractor. The Injector region houses the polarized electron source. The recirculation arcs enable the beams to make up to five passes through each linear accelerator. Each beam is separately extracted and sent to its experimental hall. Each linear accelerator can provide a maximum of about 600 MeV per pass.

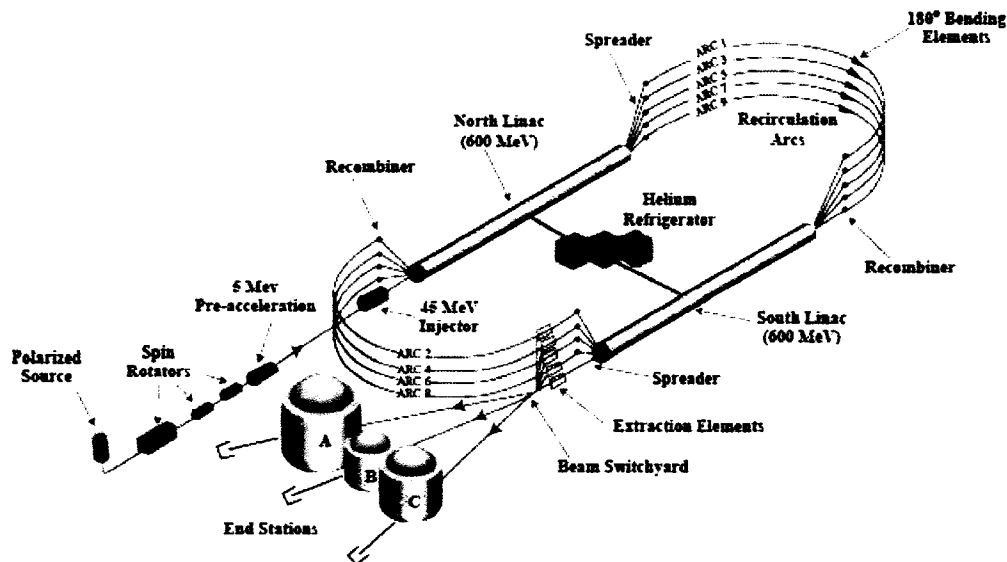


FIG. 3.1: A schematic of the CEBAF accelerator.

## 3.2 Polarized Electron Source

At Jefferson Lab, polarized electrons are generated by a 100 kV GaAs photoemission electron gun. To deliver beam to the three physics halls simultaneously, two separate laser systems are used which illuminate a common area of the photocathode. During the present experiment, Halls A and B share a laser and Hall C had its own. A beam splitter splits the single beam for Halls A and B into two separate beams. Each beam sends an optical pulse train or a series of pulses at 499 MHz which together make up 1497 MHz, the CEBAF fundamental frequency.

The laser produces linearly polarized light which is converted into a circularly polarized beam by a Pockels cell (see Section 3.2.3). The circularly polarized laser light is directed onto a photocathode and electrons are produced via photoemission. A schematic of the injector laser table is shown in Figure 3.2. The sign and degree of the electron beam polarization is determined by the sign and degree of the circular



The photoemission of electrons from a semiconductor into the vacuum consists of three steps: the photoexcitation of electrons into the conduction band (the energy region at which electrons can move freely through the material), the transport of electrons to the surface, and emission of electrons into the vacuum (the energy at which an electron becomes free from its host ion).

The addition of a small percentage of foreign atoms in the regular crystal lattice of a semiconductor produces n-type and p-type semiconductors. In a n-type semiconductor, the impurity contributes free electrons. The surface states of the semiconductor gain extra electrons and the surface becomes negatively charged. In a p-type semiconductor, the impurity creates deficiencies of valence electrons called holes. The surface states donate electrons to the valence band and the surface becomes positively charged. The most valuable property of p-type III-V semiconductors is their ability to obtain Negative Electron Affinity (NEA). NEA occurs when the vacuum level lies below the conduction band minimum so that electrons can escape practically unscathed. The vacuum level lowering occurs when monolayer quantities of alkali metals, e.g. cesium, of electropositive nature and low ionization potential are deposited on the semiconductor surface. GaAs is the most widely used photoemitter because it has the largest direct bandgap (the region between the vacuum level and bottom of the conduction band). This property creates a larger NEA level because the conduction band minimum is farther removed from the vacuum level of the cesium-oxide layer.

### **Types of GaAs Photocathodes**

There are three types of GaAs photocathodes used in electron accelerators to date: bulk, strained and superlattice GaAs. When 100% circularly-polarized photons are incident on bulk GaAs, the photoemitted electrons can be emitted with a theoretical maximum of 50% polarization. In practice, typical polarizations of

35-40% are achieved. The strained-layer GaAs photocathode consists of a 100 nm active layer of p-doped GaAs grown atop a layer of GaAsP, with phosphorus content of 28%. Strained layer GaAs photocathodes break an energy level degeneracy in the valence band. As a result, emitted electron polarizations of 100% are theoretically possible. Typical polarizations of 70-85% are achieved. Figure 3.3 illustrates the electromagnetic transmissions of bulk and strained GaAs. The superlattice photocathode consists of a heavily p-doped 5 nm GaAs surface layer grown atop 14 pairs of alternating layers of GaAsP and GaAs. A maximum polarization of 87% has been achieved at JLab.

The most common method to quantify the effectiveness of a photocathode is by measuring its quantum efficiency (QE). The QE of a photocathode is defined as the ratio of emitted electrons to incident photons. It depends on the wavelength of illumination, the temperature of the material, and the doping concentration. Bulk GaAs crystals can have QEs greater than 1%, while strained and superlattice GaAs crystals have much a lower QE.

From 1998 to 2003, JLab used strained layer GaAs photocathodes from Bandwidth Semiconductor for production beam delivery. After a short exposure to atomic hydrogen, the semiconductor is activated to build a negative electron affinity. This activation is performed in the gun chamber by applying successive doses of Cesium and Nitrogen Trifluoride. The negative electron affinity surface allows the electrons optically excited to the conduction band to escape the cathode. Typical quantum efficiency is 0.2% at 840 nm and 1% at 780 nm. The polarization of the photoemitted electron beam from the cathode material is typically 70-80% as measured in the injector and in the halls via Moller and Mott scattering.

In March 2004, a superlattice GaAs photocathode was successfully installed and activated in Gun 3. Typical quantum efficiency is 0.4% at 780 nm. For the present experiment, a superlattice GaAs photocathode was used.

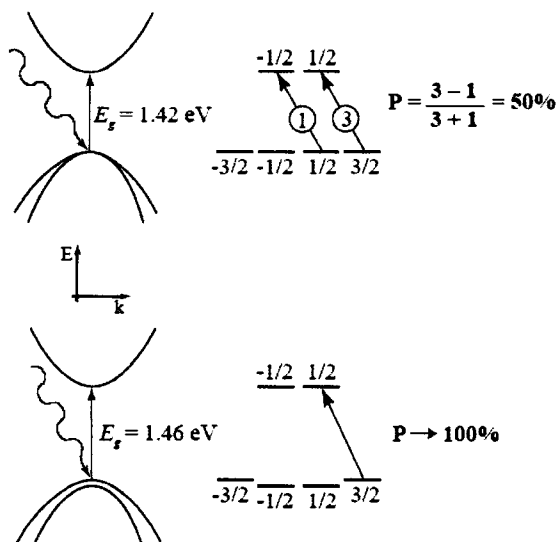


FIG. 3.3: Electromagnetic transitions in bulk and strained GaAs. The upper figure shows the transitions in bulk GaAs. The numbers in circles indicate the relative strength of the transitions. By illuminating the crystal with polarized light, the resulting electromagnetic transitions can yield electron beam polarizations of 50%. The bottom figure shows the transitions in strained GaAs. By breaking an energy level degeneracy, transitions of only one type of spin state are allowed. Therefore, the theoretical polarization approaches 100%.

### Activation and Lifetime

After the activation of the photocathode, the QE decreases gradually with time [64]. As the QE decreases, the charge-limited current density decreases. The laser power must then be increased to maintain the desired electron beam intensity from the source. At some point, the charge limit drops to a level in which the photocathode cannot deliver the desired beam intensity and the photocathode must be refreshed. This is achieved by a brief deposition of additional cesium on the surface of the photocathode. With each reactivation, there is a small decrease in the photocathode performance. After multiple reactivations, the photocathode must be heat cleaned and reactivated.

The operational lifetime of a source is the amount of charge emitted before the quantum efficiency has decreased to  $1/e$  of its initial value. The lifetime determines



the frequency at which the cathode has to be treated during operation. Lifetime depends on vacuum quality, high voltage design, and the active surface area of the photocathode. During low beam current delivery ( $< 100 \mu\text{A}$  from the cathode), the lifetime is as high as 600 C. During higher current operation (200  $\mu\text{A}$ ), the lifetime is reduced to approximately 300 C.

### 3.2.2 The Laser System

This section summarizes the history and current status of the lasers used to drive the polarized electron source. For a complete discussion, see [65]. A robust laser system is necessary to drive the electron source. In the early days of CEBAF, diode lasers were used for the majority of experiments. Diode lasers are stable, reliable, easy to use, require little maintenance, and have small noise at the frequency of the helicity reversal (0.1 % at 30 Hz). For low current and high polarization experiments, the laser wavelength was matched to the cathode bandgap (840 nm). For high current experiments where polarization was not needed, the laser wavelength was reduced to 780 nm to take advantage of the higher quantum efficiency.

Some experiments (such as the present one) require both high current and high polarization. Diode lasers are inadequate because of their power limitation. They produce less than 100 mW and limit the available electron beam current to 100  $\mu\text{A}$  at 780 nm. Titanium Sapphire (Ti:Sap) lasers obtain higher output power, about 500 mW, at high polarization wavelengths. In 2001, experiments requiring high current and high polarization were driven by a homebuilt Ti:Sap system, pumped by a high power DC Nd:YVO<sub>4</sub> and mode-locked using seed light from a gain-switched diode laser. Pumping is a process to create a population inversion, a stable state of a medium where the upper energy level is more populated than the lower energy level. This is a necessary condition for a laser. Seed light is light from one laser

that is injected into another laser. Gain switching is a technique by which a laser can be made to produce pulses of light of extremely short duration, on the order of picoseconds. Mode-locked means that there is a fixed phase relationship between the modes or frequencies of the laser's resonant cavity. The homebuilt Ti:Sap lasers exhibit more noise than diode lasers (1% at 30 Hz) and require a higher level of maintenance. The  $G^0$  forward angle experiment used a Ti:Sap system.

In March 2006, a fiber laser [66] was installed for the  $G^0$  backward angle experiment. The 499 MHz frequency of the beam from the main machine directly pulses a laser seed. The laser seed is fiber coupled and will never lose lock from the machine like a Ti-Sapphire laser sometimes does. The wavelength of the laser seed is 1560 nm. The laser seed is a common cable TV communications laser diode. The laser seed is fed into a commercial fiber laser amplifier that takes the 1 mW seed pulsing at 499 MHz and turns it into 5 Watts of light pulsing at the same rate. The commercial fiber laser amplifier is designed for TV type applications. Up to this point, all of the light is contained within glass fibers and there is no need for alignment. The output of the fiber from the amplifier is placed on the laser table where the 5 W beam at 1560 nm is launched through free space through a collimating lens. The beam is directed through a second harmonic generator (SHG) that converts a portion of the power from 1560 nm down to 780 nm. This wavelength is ideal for our superlattice cathode because it is at the peak polarization wavelength. The alignment of the SHG crystal is simple. The residual 1560 nm light is dumped away with a dichroic mirror. The 780 nm output of the SHG is collimated and taken to the cathode through all the normal optics that were used with the Ti-Sapphire laser. The beam is perfectly round when it leaves the SHG because the fiber laser itself is a single mode laser.

The fiber laser has several advantages over the Ti-Sapphire laser. It has higher power capability. In addition, the beam diameter can be changed without affecting

operation of the device. It also has a nicer beam profile as it can only support a single transverse electromagnetic (TEM) mode. A transverse mode of a beam of electromagnetic radiation is a particular intensity pattern of radiation measured in a plane perpendicular to the propagation direction of the beam. A TEM mode is a mode whose electric and magnetic field vectors are both normal to the direction of propagation. The fiber laser has no laser cavity to align, there is no chance of losing lock, and the rf phase can be quickly shifted. In addition, there is no drifting of the output beam over time so the Pockels cell alignment should hold indefinitely.

### 3.2.3 Optical Elements in Source

There are four primary optical elements in the source: a linear polarizer, a waveplate, a Pockels cell, and a quadrant photodiode. In order to understand the functions of these elements, as explained in the following sections, it is necessary to be familiar with birefringence and the scientific terms associated with it.

Birefringence is the division of light into two components (an “ordinary” and an “extraordinary” ray), found in materials that have two different indices of refraction in different directions. Birefringence is associated with uniaxial crystals, which belong to the hexagonal, tetragonal, and trigonal crystal systems. In a uniaxial crystal, there is one direction such that any light in that direction in the crystal has the same speed, regardless of its state of polarization. This direction is called the optic axis. Light with linear polarization perpendicular to the optic axis comprises the ordinary ray. Light with linear polarization parallel to the optic axis comprises the extraordinary ray. The birefringence is quantified by  $\Delta n = n_e - n_o$ , where  $n_o$  is the refractive index for the ordinary ray and  $n_e$  is the refractive index for the extraordinary ray. The direction of the lesser index is called the fast axis because the speed of light is faster in that direction. Similarly, the other is called the slow

axis.

### Linear Polarizer

The polarization of an electromagnetic wave refers to the orientation of its electric field  $\vec{E}$ . Unpolarized light is comprised of a mixture of wave vibrations lying in all possible directions perpendicular to the direction of travel. The direction of  $\vec{E}$  is randomly varying with time. A Linear Polarizer (LP) is a device that only allows electric field components parallel to a certain direction, called the polarization axis, to pass through. Any light that comes through such a polarizer is polarized in the direction of the polarization axis.

### Waveplate

A waveplate is a birefringent optical device that alters the polarization state of a light wave travelling through it. It divides an incident, polarized beam into two components and changes the phase of one relative to the other while passing through the wave plate. Then, it recombines them as they leave the wave plate. The thickness of the wave plate determines the amount of phase shift.

A quarter-wave plate introduces a relative phase difference of  $\pi/2$  radians or  $90^\circ$  between the ordinary and extraordinary waves. Quarter-wave plates are used to turn plane-polarized light into elliptical polarized light and vice-versa. When linear light at  $45^\circ$  to either principal axis is incident on a quarter-wave plate, its ordinary and extraordinary components have equal amplitudes. Under these special circumstances, a  $90^\circ$  phase shift converts the wave into circular light. Similarly, an incoming circular beam will emerge linearly polarized.

A half-waveplate introduces a relative phase difference of  $\pi$  radians or  $180^\circ$  between the ordinary and extraordinary waves. It rotates linear polarization by an angle  $2\theta$ , where  $\theta$  is the angle between the fast axis of the half-waveplate and the

incoming linear polarization axis. It also changes right circularly polarized light to left circularly polarized light and vice-versa.

Parity-violating experiments two half-waveplates: an insertable half-wave plate (IHWP) and a rotatable half-wave plate (RHWP). THE IHWP is used to achieve a slow reversal of the beam helicity. It is inserted into or removed from the laser beam approximately every other day. When interchanging the IHWP, the physics asymmetry flips sign but false asymmetries due to electronics do not. If there are no electronic asymmetries, then the sum of the asymmetries measured in the two states should be zero. The RHWP nulls any helicity-correlated intensity asymmetry (see Section 3.5.1).

### **Pockels Cell**

A Pockels Cell (PC) is a voltage-controlled birefringent crystal. It alters the polarization of a laser beam when voltage is applied to the cell by causing a phase retardation between orthogonal polarization components of the beam. Figure 3.4 shows a Pockels Cell between two linear polarizers. An applied electric field creates fast and slow axes at  $90^\circ$  to one another. The difference in velocity for beams with polarization components along these two directions, with voltage applied, retards the phase of one polarization component relative to the other thereby changing the polarization state of the emerging beam. In the absence of an applied field, the refractive index is the same for both polarization directions. There is no phase retardation between orthogonal polarization components of the light beam and hence there is no polarization change.

In our setup, vertically polarized light enters the birefringent material. The PC is rotationally oriented such that the fast and slow axes that are induced by the application of a voltage to the PC are at  $\pm 45^\circ$  to the polarization direction of the input light beam, as shown in Figure 3.5. The two components, in phase as they



FIG. 3.4: A Pockels Cell between two linear polarizers.

enter the crystal, emerge with different phases. As they traverse the crystal, they accumulate a phase difference, which depends on the distance traveled and on the applied voltage. When the beams emerge from the crystal, the polarization of the combined single beam depends on the accumulated phase difference.

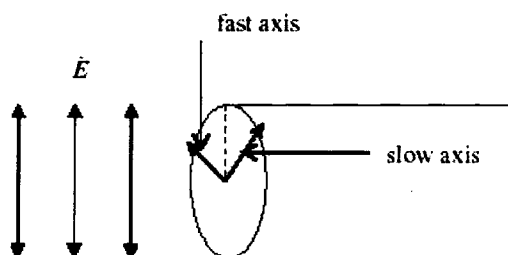


FIG. 3.5: The orientation of the PC with respect to the polarization direction of the input light beam.

The polarization of the beam is determined by both the Pockels Cell and a Linear Polarizer upstream of the PC. The LP is a cleanup polarizer and is used to produce vertically polarized light free of any ellipticity that may have crept into the polarization. The PC acts as a quarter-wave plate with its fast axis at  $45^\circ$  from the vertical whose retardation flips sign pseudorandomly on a pulse-by-pulse basis,

generating circularly-polarized light of either helicity.

### Quadrant Photodiode

A Quadrant Photodiode (QPD) is used to measure helicity-correlated position differences and charge asymmetry of the laser light during the PC installation. It is used only in testing and not during production. It functions as both a Beam Current Monitor (BCM) and a Beam Position Monitor (BPM). A QPD consists of four photodiodes arranged in four quadrants of a circular structure, as shown in Figure 3.6. These photodiodes are used to compare the intensity in each half of the beam, both horizontally and vertically. Sensor output is proportional to the beam energy hitting the sensor. The disadvantage of the device is that accurate results depend on the beam hitting all sensors simultaneously. If it hits only two sensors, position can be determined in only one dimension. If it hits only one sensor, all positional information is lost.



FIG. 3.6: *A Quadrant Photodiode.*

### 3.3 Beam Structure

This section describes the helicity control and timing scheme of the experiment. A more thorough description is given in [67]. The helicity flip at the Pockels cell occurs at the transitions of the 30 Hz clock signal. The  $G^0$  analogue of this signal is the MPS or macro-pulse trigger. The signal consists of a low period of length  $T_{\text{settle}}$  and a high period of length  $T_{\text{stable}}$ . The  $T_{\text{settle}}$  period is 200  $\mu\text{s}$  and allows time for the Pockels cell to stabilize and time for the experiment to read out data. The  $T_{\text{stable}}$  period is 33.333 ms exactly and is the time when the Pockels cell is stable and also the time when the experiment takes data. The  $T_{\text{stable}}$  interval is equal to  $2T_{\text{line}}$ , where  $T_{\text{line}}$  is the period of the power line cycle.

The dominant source of noise in all electronics comes from the power lines at 60 Hz. Therefore, cables and electronics are likely to have some noise that oscillates at 60 Hz. To average over this noise, one counts over an integer multiple of one period, in this case  $2 \times (1/60 \text{ Hz}) = 33.33 \text{ ms}$ .

The helicity signals are generated in quartets:  $+--+$  or  $-+-$ , where the first element in the quartet is chosen pseudo-randomly. The helicity signal transitions at the instant the Pockels cell is set to a new state. The quartet trigger defines when a new random sequence of four helicity states has started.

The 120 Hz signal is a signal at 120 Hz that is produced at 4 times the MPS (30 Hz) frequency. It subdivides the MPS high period into 4 so the experiment can monitor the data for 60 Hz components. The timing signals from the polarized source is shown in Figure 3.7.



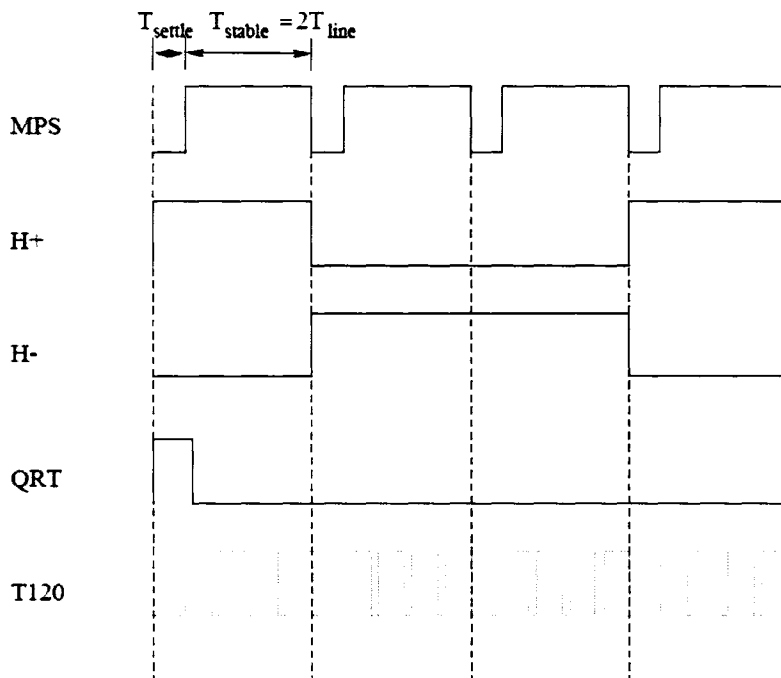


FIG. 3.7: Polarized source signal timing for  $G^0$ .

## 3.4 Types of Laser Systematics

This section briefly describes the systematic effects that stem from the laser beam and optics system that is used in the polarized electron source to produce the polarized electron beam. A more complete description of the sources of systematics and strategies for their minimization is given in [68].

### 3.4.1 Charge Asymmetry

Charge asymmetries result when the average electron beam current corresponding to one helicity state is different from the average current corresponding to the other helicity state. The asymmetries arise from the fact that when making circularly polarized light, there are always small imperfections or admixtures of linear

polarization that cause a small degree of ellipticity. Imperfections in the laser beam's circular polarization stem primarily from imperfect alignment of the PC axes with respect to the incoming linear polarization.

When the helicity of the light is flipped, the major axis of the polarization ellipse will rotate by  $90^\circ$ . Most optics systems have elements (for example mirrors) that transport one linear polarization better than the other. This property is referred to as a transport asymmetry or analyzing power. Therefore, flipping the helicity causes a change in the efficiency with which the light is delivered to the cathode. This type of effect is called the PITA effect, where PITA is an acronym standing for Polarization Induced Transport Asymmetry.

The PITA effect can be characterized quantitatively. The phases introduced by the PC can be written in the form

$$\delta^\pm = \pm \left( \frac{\pi}{2} + \alpha \right) - \Delta, \quad (3.1)$$

where the superscript  $\pm$  indicates the two helicities,  $\alpha$  is the symmetric piece of the imperfect phase shift, and  $\Delta$  is the antisymmetric piece of the imperfect phase shift. If  $\Delta = \alpha = 0$ , the phases introduced by the PC are  $\pm \pi/2$  and the light will have perfect circular polarization. If either  $\Delta$  or  $\alpha$  are nonzero, elliptical polarization will result. The charge or current asymmetry can be written as

$$A_I = \frac{I^R - I^L}{I^R + I^L} \propto \Delta, \quad (3.2)$$

where  $I^R$  ( $I^L$ ) are the electron beam intensities associated with the PC phases  $\delta^+$  ( $\delta^-$ ). The equation for  $A_I$  depends linearly on  $\Delta$  but not at all on  $\alpha$ . Hence, when a laser beam is transmitted through an analyzing power, an intensity asymmetry results that depends only on the antisymmetric phase shifts. This can be

explained as follows. For example, if  $\alpha = \pi/4$ , the phases introduced by the PC are

$$\delta^+ = +\left(\frac{\pi}{2} + \alpha\right) = +\left(\frac{\pi}{2} + \frac{\pi}{4}\right) = +\frac{3\pi}{4} \quad (3.3)$$

$$\delta^- = -\left(\frac{\pi}{2} + \alpha\right) = -\left(\frac{\pi}{2} + \frac{\pi}{4}\right) = -\frac{3\pi}{4}, \quad (3.4)$$

and the polarization ellipses for the two helicity states will be coincident with one another. Only the direction that the electric vector travels around the ellipse will change. A nonzero  $\alpha$  phase shift is shown in Figures 3.8a and 3.8b.

If  $\Delta = \pi/4$ , the phases introduced by the PC are

$$\begin{aligned} \delta^+ &= +\frac{\pi}{2} - \Delta = +\frac{\pi}{2} - \frac{\pi}{4} = +\frac{\pi}{4} \\ \delta^- &= -\frac{\pi}{2} - \Delta = -\frac{\pi}{2} - \frac{\pi}{4} = -\frac{3\pi}{4}, \end{aligned} \quad (3.5)$$

and polarization ellipses result whose major axes will rotate by  $90^\circ$  when the helicity is flipped. In other words, the two polarization ellipses will have their major and minor axes interchanged, an antisymmetric behavior. The plus sign indicates that the electric vector travels counter-clockwise around the ellipse. The negative sign indicates that the electric vector travels clockwise around the ellipse. A nonzero  $\Delta$  phase shift is shown in Figures 3.8c and 3.8d. If the polarization ellipses in Figure 3.8 are propagated through an asymmetric transport element with greater transmission along the vertical element than the horizontal, the ellipses with symmetric phase shifts are transmitted with equal intensity whereas the ellipses with antisymmetric phase shifts are not.

### 3.4.2 Position Differences

Position differences result when the average position corresponding to one helicity state is different from the average position corresponding to the other helicity state. Position differences stem primarily from two sources: phase gradients and steering effects.

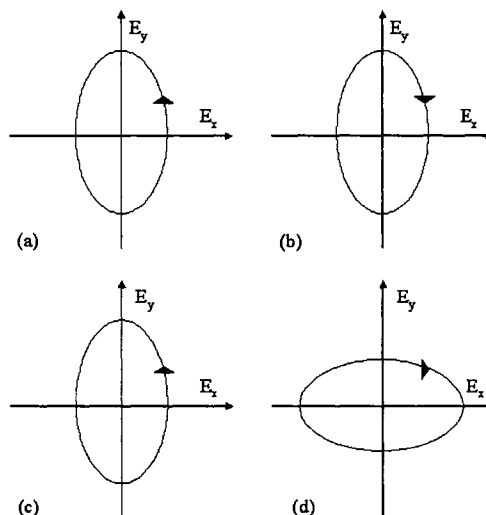


FIG. 3.8: *Polarization ellipses for non-zero  $\alpha$  and  $\Delta$  phase shifts. (a) and (b) are polarization ellipses for right- and left-helicity light where  $\alpha$  is non-zero. (c) and (d) are polarization ellipses for right- and left-helicity light where  $\Delta$  is non-zero.*

### Phase Gradients

As explained above, a charge asymmetry can result from a nonzero value of the phase  $\Delta$ . The phase  $\Delta$  and hence the associated charge asymmetry can vary in some way across the laser spot as shown in Figure 3.9. If the charge asymmetry changes from the left of the crystal to the right, the beam profiles for the two helicity states will have centroids that are shifted horizontally with respect to one another. These shifts are seen as helicity-correlated position differences, as shown in Figure 3.10.

### Steering Effects

Another source of helicity-correlated position differences is steering caused by the PC. The PC is alternately pulsed to positive and negative high voltage in order to introduce phases. This results in the PC behaving alternately as a diverging and converging lens as shown in Figure 3.11. If a laser beam is small enough in diameter and goes through the center of the PC, the steering effects are small. As one goes

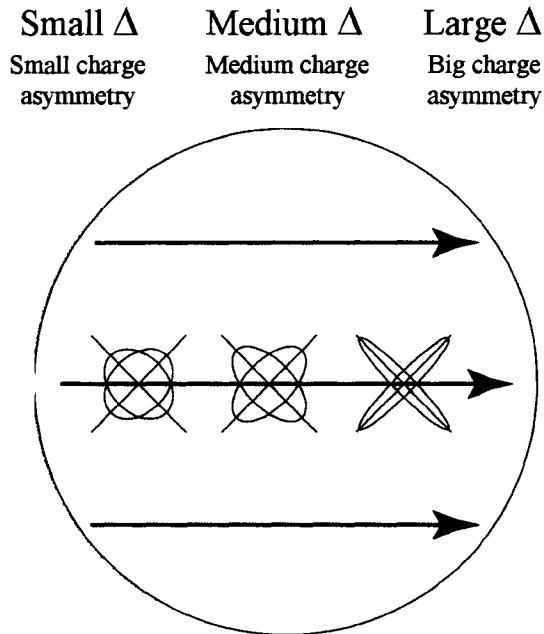


FIG. 3.9:

*Illustration of a GaAs crystal being irradiated by light. The residual linear polarization varies from a minimum at the left of the crystal to a maximum at the right of the crystal [68].*

off center, some steering occurs. This effect can be big.

## 3.5 Controlling Laser Systematics

### 3.5.1 Controlling Charge Asymmetries

#### Phase Adjustments

The phase  $\Delta$  can be controlled using the PC. The nominal voltage at which a PC is pulsed is  $\pm 2,700$  V. If a fixed voltage is added to the voltage associated with each polarity, one can introduce an arbitrary  $\Delta$ . For example, one could run at  $+2,900$  V and  $-2,500$  V. The voltage difference between the two states remains the same. As indicated in Equation 3.1, the sign of the antisymmetric phase for the two

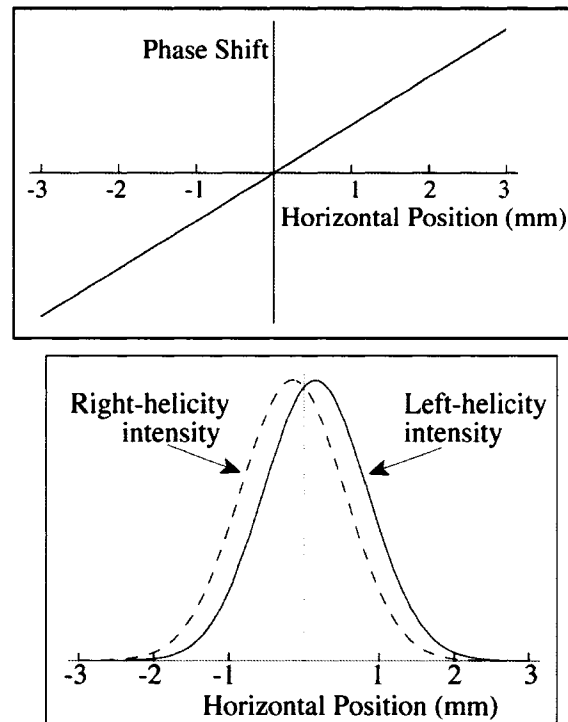


FIG. 3.10: *The effect of a linear gradient in the phase across the face of the laser beam on the spatial intensity profile of the electron beam. The top figure shows the linear gradient in phase. The bottom figure shows the corresponding intensity profile for right- and left- helicity electron beams. The gradient shifts the centroids of the right- and left- helicity electron beams in opposite directions, thereby producing a helicity-correlated position difference [68].*

states is the same.

### Intensity Asymmetry Cell

An Intensity Asymmetry (IA) cell is used to control charge asymmetries. It operates at low voltages (0-200 V) and artificially induces charge asymmetry. It consists of an upstream linear polarizer, a waveplate, a Pockels Cell, and a downstream linear polarizer. The charge asymmetry can be carefully measured, and the IA cell pulsed to a slightly different voltage for each helicity to achieve balance.

In September 2005, IA studies were performed to determine the waveplate and

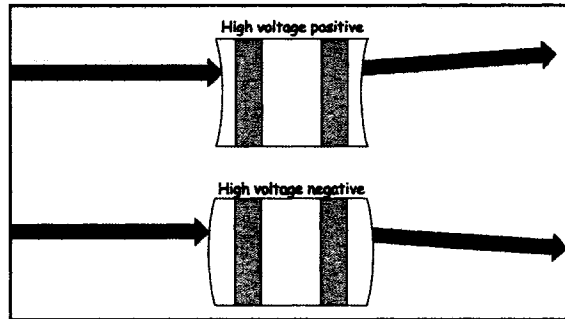


FIG. 3.11:

*Illustration of steering due to a Pockels Cell having lens-like properties when it is pulsed at high voltages [68].*

waveplate angle to be used in the IA cell. Two types of IA studies were done: IA voltage scans and IA angle scans. The purpose of an IA voltage scan is to measure the linear dependence of intensity asymmetry on voltage. A large slope is critical to correct a large intensity asymmetry. In an IA voltage scan, the waveplate angle is fixed, and the IA voltage is varied from 0 V to 120 V. At each voltage setting, the intensity asymmetry is measured and recorded. This scan was performed on three waveplates:  $\lambda/10$ ,  $\lambda/4$  and  $\lambda/2$ . The results of these scans are shown in Table 3.1. According to the data, the  $\lambda/4$  waveplate has larger slopes compared to the  $\lambda/10$  waveplate.

The purpose of an IA angle scan is to measure the dependence of transmitted intensity on angle. In an IA angle scan, the voltage difference is fixed and the waveplate angle is varied from  $0^\circ$  to  $36^\circ$ . At each angle setting, the transmitted intensity is measured and recorded. This scan was performed on three waveplates:  $\lambda/10$ ,  $\lambda/4$  and  $\lambda/2$ . Table 3.2 summarizes the results of the IA angle scans. According to the data, the intensity loss of the  $\lambda/2$  waveplate is significant and the transmission falls to zero over the range of  $\theta$  ( $2.9\%/\circ \times 36^\circ$ ). The intensity loss of the  $\lambda/4$  waveplate is about half that of the  $\lambda/2$  waveplate. Over the range of  $\theta$ , the transmitted intensity

waveplate	angle (°)	Asym/Voltage (ppm/V)
$\lambda/10$	0	4.22
	10	34.83
	20	61.21
$\lambda/4$	0	3.72
	10	-48.24
	20	-112.74
	-10	54.47
	-20	114.45
$\lambda/2$	0	12.66
	-10	8.88
	-20	-2.34

TABLE 3.1: *IA Voltage Scans. The waveplate is fixed at a given angle and the voltage is varied from 0 V to 120 V.*

falls to about 50%. The intensity loss of the  $\lambda/10$  waveplate is about 10%. Based on the findings of both the IA voltage and angle scans, we decided to use the  $\lambda/4$  waveplate at about  $20^\circ$  in the IA cell.

### Rotatable Half Waveplate

Since the fast axis of the Pockels Cell is oriented at  $\pm 45^\circ$  to the polarization direction of the input light beam, the major axes of the ellipses are either vertical or horizontal when the laser light emerges from the Pockels cell. By rotating the half waveplate, the orientation of the ellipses can be rotated. The basic setup for using a rotating half waveplate is shown in Figure 3.12. To minimize charge asymmetry, major axes of the ellipses are oriented at  $\pm 45^\circ$  with respect to the analyzing-power axis.

The charge asymmetry should vary sinusoidally with  $4\theta$ . This is because a  $90^\circ$  rotation of the half-wave plate will rotate the polarization ellipses by  $180^\circ$ , at which point the pattern should repeat. We see both  $4\theta$  and  $2\theta$  components because the half-wave plate has imperfections and therefore introduces a  $\Delta$ -like phase (see



waveplate	+HV	-HV	Transmitted Intensity(%/°)	Asym (ppm) /°
$\lambda/10$	0	0	-0.30	0.38
	0	30	-0.28	84.59
	30	30	-0.30	163.03
	0	60	-0.23	166.79
$\lambda/4$	0	0	-1.44	-0.18
	0	30	-1.48	-252.33
	30	30	-1.37	-443.04
$\lambda/2$	0	0	-2.83	-0.38
	0	30	-2.92	-111.49
	30	0	-2.74	123.07
	30	30	-2.73	-188.55

TABLE 3.2: *IA Angle Scans. The voltage difference is fixed and the waveplate angle is varied from 0° to 36°.*

Figure 3.12). This figure also shows that  $x$  and  $y$  position differences vary with the RHWP angle.

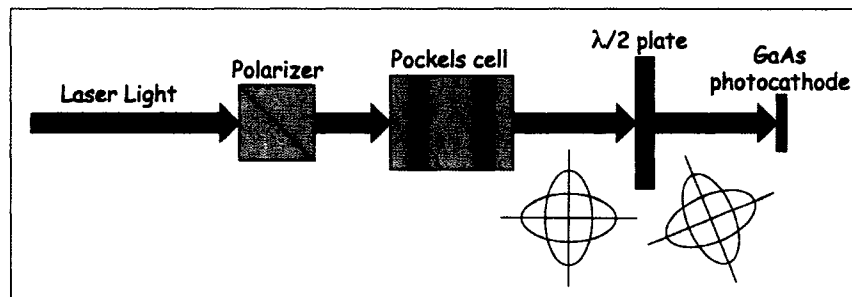


FIG. 3.12:

*The basic setup for using a rotatable half-wave plate to minimize charge asymmetry [68]. The polarizer is a linear polarizer and the  $\lambda/2$  is the rotatable half-wave plate.*

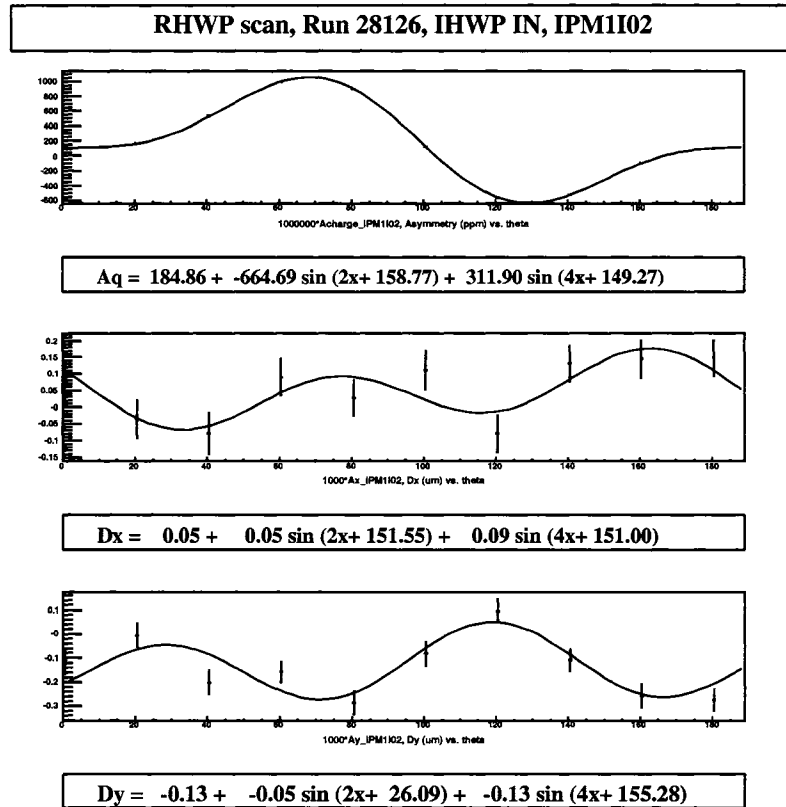


FIG. 3.13:

*A RHWP scan. The upper plot is charge asymmetry versus RHWP angle. The fit includes a constant, a  $2\theta$  term and a  $4\theta$  term. The middle plot is  $x$  position difference versus RHWP angle. The bottom plot is  $y$  position difference versus RHWP angle.*

### 3.5.2 Controlling Position Differences

#### Minimize Steering

Steering is minimized by centering the laser beam on the Pockels cell. The PC is translated in two dimensions while monitoring the position differences. The dependence of position differences on steering are shown in Figure 3.14. The charge asymmetry always shows no dependence on position. In a steering scan where the PC is translated in  $x$ , the  $y$  position difference varies linearly with  $x$ . Similarly,

in a steering scan where the PC is translated in  $y$ , the  $x$  position difference varies linearly in  $y$ .

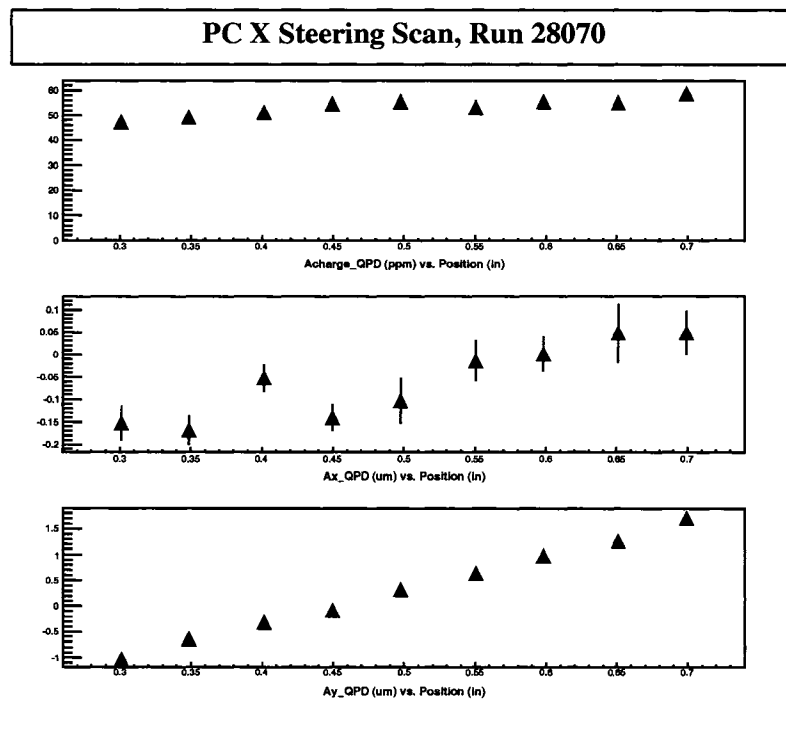


FIG. 3.14:

*A steering scan. The upper plot shows charge asymmetry versus beam position on the Pockels cell. The middle and bottom plots show  $x$  position and  $y$  position differences versus beam position on the Pockels cell, respectively.*

### Minimize the Effects of Phase Gradients

A primary source of phase gradients is the Pockels cell. The phase  $\Delta$  and hence the associated charge asymmetry can vary across the aperture of the cell. Like steering, these phase gradients are minimized by translating the Pockels cell in two dimensions while monitoring the position differences. The one difference is that a LP is inserted after the Pockels cell and before the QPD to introduce an analyzing power. The dependence of position differences on phase gradients are

shown in Figure 3.15. The charge asymmetry and position differences always show a sine-like variation with position. In fact, the curves seem to be a characteristic of the PC. In every installation we performed, the curves were identical for the same PC (with the exception of different offsets).

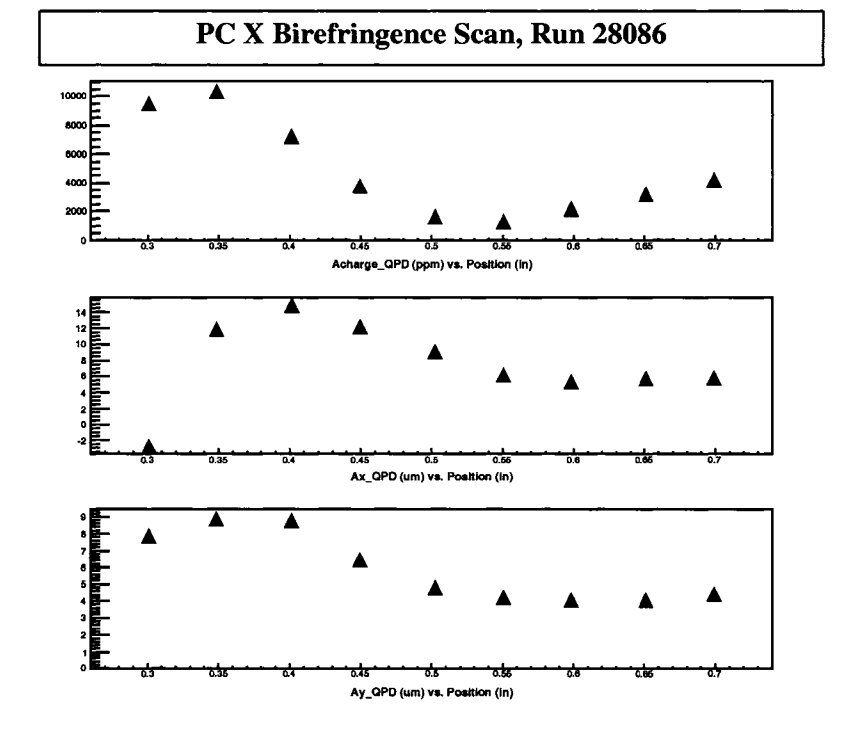


FIG. 3.15:

*A phase gradient scan. The upper plot shows charge asymmetry versus beam position on the Pockels cell. The middle and bottom plots show x position and y position differences versus beam position on the Pockels cell, respectively.*

### 3.6 PC Installation Procedure

This section summarizes the PC installation procedure. For a detailed explanation, see [69]. We begin the PC installation by first checking that the laser spot at the PC is a fine point. Next, we measure the degree of linear polarization. In order to

make position and charge measurements on the QPD, it is necessary to determine the QPD pedestals, center the QPD, and calibrate the QPD. Afterwards, electronic noise measurements are performed to confirm that differences/asymmetries are consistent with zero. First, both the IA and PC are unplugged and differences/asymmetries are measured. Next, the IA is plugged back in but the PC is left unplugged and differences/asymmetries are measured. Following the noise measurements, IA voltage and angle scans are done to determine the optimal operating angle and the intensity dependence on voltage. Based on the IA scans, the IA charge asymmetry is zeroed. Next, the PC is plugged back in and differences/asymmetries are measured for both states of the half-wave plate. This is followed by  $x$  and  $y$  steering scans for both states of the half-wave plate. According to the steering scans, position differences are then minimized. Different states of the half-wave plate yield different  $x$  and  $y$  positions. Differences/asymmetries are measured for both states of the half-wave plate to verify that they are minimized. The LP is inserted, followed by QPD centering and calibration scans. Differences/asymmetries are measured for both states of the half-wave plate. They are not minimized as doing so would compromise the differences/asymmetries obtained with the LP out (steering). Experience has shown that steering effects dominate the beam quality rather than phase gradient effects (LP in).

# CHAPTER 4

## Analysis

This chapter presents the details of the analysis for data taken during the first part of the 687 MeV run, beginning in March 2006 and ending in May 2006. A description of raw data management and processing is provided in Section 4.1, followed by a summary of nominal running conditions in Section 4.2. The measured asymmetry is defined in Section 4.3 and a discussion of the Cerenkov electron and pion efficiencies is provided in Section 4.4. The remainder of the Chapter is a detailed summary of the cuts and corrections that transform the raw asymmetries to physics asymmetries. In chronological order, these cuts/corrections include CED-FPD matrix space cuts, deadtime, linear regression, background, and polarization corrections.

### 4.1 Raw Data Management and Processing

The DAQ acquires the raw data and stores it to disk. During data-taking, shift leaders start and stop the DAQ every 60 minutes to segment the raw data into runs. Each run is processed by a replay engine (`g0analysis`) to extract physics quantities. `G0analysis` is analysis software customized specifically for the  $G^0$  experiment. It is

written in C++ and uses the ROOT package to organize data in the form of ntuples (MPS and quartet). Detector and beam data are calculated MPS by MPS while helicity-correlated differences/asymmetries are calculated quartet by quartet. At the end of the replay, the ntuples are stored in rootfiles according to run number.

At the beginning of a replay, instrument calibrations (pedestals and gains) are loaded from a MySQL database. At the end of a replay, the analysis results (yields, asymmetries, linear regression slopes, and beam parameter averages) are written to the database. The MySQL database manages a large set of structured data and runs operations on the data requested by multiple users. It presents the data as a collection of tables with each table consisting of a set of rows and columns and provides relational operators to manipulate the data in tabular form.

During the replay, a cut is applied to data acquired during a beam trip. The beam is regarded as unstable if the beam current varies by more than 100 nC/mps ( $100 \text{ nC/mps} \times 1 \text{ mps}/33.33 \text{ ms} = 3 \mu\text{A}$ ) between an MPS and the MPS four events prior. In other words, the beam is considered unstable if the beam current in the first and last MPS of a quartet vary by more than 100 nC/mps. The liquid hydrogen target requires time to thermally stabilize after the beam current is ramped back up to  $60 \mu\text{A}$ , so the first 500 mps ( $500 \text{ mps} \times 33.33 \text{ ms}/1 \text{ mps} = 17 \text{ seconds}$ ) after the beam starts to ramp up are removed. An additional cut is made on any data where the beam current is less than 20 nC or  $0.6 \mu\text{A}$ . This cut serves as the “beam off .”

In order to prevent interpretation of the form factors until all of the corrections have been applied to the raw asymmetries and to avoid any possible unconscious bias affecting the result, the raw asymmetries are disguised by a blinding factor. The blinding factor is a multiplicative factor between 0.75 and 1.25.

Beam current	60 $\mu\text{A}$
Herbert's paddle	1.2 $\mu\text{A}$
Cerenkov PMT yield	40-60 kHz/ $\mu\text{A}$
(CED,FPD) cell yield	0.01 - 0.06 kHz/ $\mu\text{A}$
Charge asymmetry RMS	500 ppm
Lumi RMS	300 ppm
Halo	0-20 Hz/ $\mu\text{A}$

TABLE 4.1: *Nominal running conditions.*

## 4.2 Nominal Running Conditions

The nominal running conditions are summarized in Table 4.1. Herbert's paddle is a scintillation counter paddle located on the ferris wheel platform. It provides a rate measurement in the vicinity of the detectors from beam-target interactions. Herbert's paddle should read about 3% of the beam current for good beam conditions.

## 4.3 The Measured Asymmetry

The definition of the measured parity-violating asymmetry is given by

$$A_{meas} = \frac{Y_{meas}^+ - Y_{meas}^-}{Y_{meas}^+ + Y_{meas}^-}, \quad (4.1)$$

where  $Y_{meas}$  is the measured normalized yield and the superscripts  $\pm$  refer to positive and negative helicity states of the beam.  $Y_{meas}$  is defined as the ratio of the measured rate  $r$  and the beam charge  $Q$

$$Y_{meas} = \frac{r}{Q}. \quad (4.2)$$

As explained in section 3.3, the helicity signals are generated in quartets:  $+- -+$  or  $-+ +-$ . Since a quartet contains two states of positive helicity and two states



of negative helicity, the parity-violating asymmetry in one quartet is

$$A_{QRT} = \frac{Y_1^+ + Y_2^+ - Y_1^- - Y_2^-}{Y_1^+ + Y_2^+ + Y_1^- + Y_2^-}, \quad (4.3)$$

where  $Y_{1,2}^+$  are the measured yields in the macro-pulses with positive helicity and  $Y_{1,2}^-$  are the measured yields in the macro-pulses with negative helicity. The asymmetry in the measured particle detection rate over one quartet is given by

$$A(r) = \frac{r^+ - r^-}{r^+ + r^-}, \quad (4.4)$$

and the asymmetry in the electron beam charge over one quartet is

$$A(Q) = \frac{Q^+ - Q^-}{Q^+ + Q^-}. \quad (4.5)$$

Using Equation 4.2, we can write the parity-violating asymmetry carried by the measured yield as the difference between the asymmetry in the particle detection rate and the charge asymmetry

$$\begin{aligned} A(Y_{meas}) &= A\left(\frac{r}{Q}\right) \\ &\simeq A(r) - A(Q), \end{aligned} \quad (4.6)$$

where we make use of the mathematical identities in Appendix A. This approximation is only true if  $A(r)A(Q) \ll 1$ .

## 4.4 Cerenkov Efficiencies

To prevent contamination of the parity-violating signal, it is crucial to have good identification of electrons. The most important parameters for electron identification are the efficiency for identification of electrons and the contamination from pions. One method to determine the electron and pion efficiencies of the Cerenkov is to use a 31 MHz beam structure (32 ns pulsed-beam). This beam structure enables one to

separate the electrons from the pions based on their time of flight. The time of flight of pions from the target to the FPDs is a few ns longer (depending on FPD) than the time of flight of electrons since pions of the same momentum have a smaller velocity. This time difference is explained below. We can obtain the relativistic energy of the scattered electron by combining Equations 1.55 and 1.61

$$E_c = \frac{m_b E_a}{m_b + 2E_a \sin^2 \theta / 2} \quad (4.7)$$

At full backscatter ( $\theta = 180^\circ$ ),  $E = 278$  MeV. This energy has a  $\beta$  of about 1. For pions, we can take the central momentum (350 MeV/c) and calculate the relativistic total energy

$$E = \sqrt{p^2 c^2 + m^2 c^4} = 377 \text{ MeV}. \quad (4.8)$$

This energy yields a  $\beta$  of about 0.9. Therefore, the pions have a smaller velocity than the electrons.

The remainder of this section summarizes the method to determine the Cerenkov efficiencies. The original work can be found here [81]. From scatter plots of the Cerenkov ADC signal versus FPD timing (see Figure 4.1), a separation of the pion and electron loci can be observed. Using only FPD timing cuts, clean electron and pion regions were defined. The Cerenkov electron efficiency is defined as the ratio of the number of particles that fired the Cerenkov and also passed the electron timing cut to the number of particles that passed the electron timing cut. Similarly, the Cerenkov pion efficiency is defined as the ratio of the number of particles that fired the Cerenkov and also passed the pion timing cut to the number of particles that passed the pion timing cut. The rejection ratio is defined as the ratio of the electron efficiency to the pion efficiency.

On the carbon target, the electron efficiencies of octant 1 range from 70-86% (depending on FPD) and the average electron efficiency of octant 1 is 79.0%. The pion

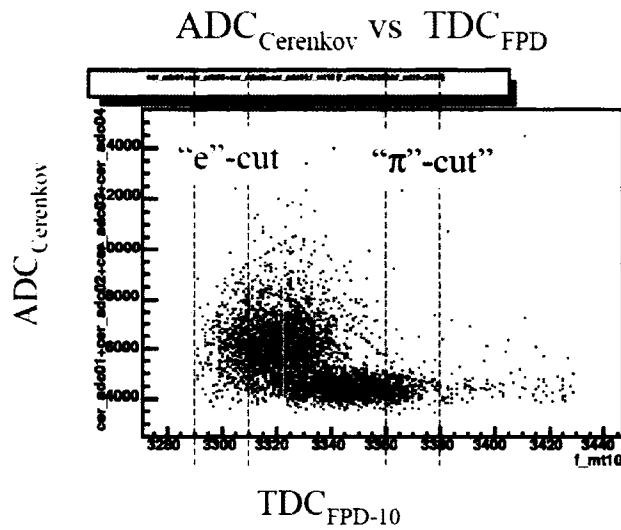


FIG. 4.1:

*Cerenkov ADC (sum of all 4 tubes) versus mean time of FPD 10 of the the elastic locus in Octant 1 on LH2 [81].*

efficiencies of octant 1 range from 0.5-3.5% and the average pion efficiency of octant 1 is 1.2%. The carbon target is better than the hydrogen target for extracting the pion efficiency since the carbon atom has more neutrons than the hydrogen atom and therefore gives a better pion yield and lower sensitivity to electron contamination. The rejection ratio is 68.2.

On the hydrogen target, the pion cuts were not as clean as for the carbon target. As a result there may be some electron leakage in the “pion” cut region. The electron efficiencies of octant 1 range from 70-86% (depending on FPD) and the average electron efficiency of octant 1 is 78.6%. The pion efficiencies of octant 1 range from 3-30% and the average pion efficiency of octant 1 is 7.7%. The rejection ratio is 10.2. As noted, there may be electron leakage, causing this to be an underestimate.

## 4.5 CED-FPD Matrix Space Cuts

The CED-FPD matrix space is a two-dimensional representation of CED-FPD coincidence rates (events which fire both a CED and FPD). CED detector numbers are incremented on the vertical axis, beginning with one at the lower end and extending to nine at the upper end. Similarly, FPD detector numbers are incremented on the horizontal axis, beginning with one at the left end and extending to 16 at the right end. In total, the CED-FPD matrix space contains 144 cells. Each cell contains a rate corresponding to its CED-FPD coincidence. There are 16 CED-FPD matrix spaces, two associated with each octant: “electron” and “pion”. CED-FPD coincidences which fire the Cerenkov compose the CED-FPD electron matrix space while CED-FPD coincidences which do not fire the Cerenkov compose the CED-FPD pion matrix space. The Cerenkov is “fired” when at least two of the four PMTs in a Cerenkov octant are hit. This is the definition that was assigned to the “Majority Logic”.

The CED-FPD matrix space has four loci defined: elastic, inelastic, background, and super-elastic. The elastic locus primarily includes particles scattered elastically in the electron-proton collision. In the elastic collision, the momentum of the electron and proton changes but no energy is lost to other processes. The electron’s kinetic energy is shared between itself and the target proton after the collision. The inelastic locus consists primarily of particles scattered inelastically in the electron-proton collision. In the inelastic collision, part of the kinetic energy of the incident electron is lost to other processes. Sometimes, this energy transforms the proton into a resonance. Other times, the energy creates additional particles such as pions. The background locus is mainly comprised of beam halo and particles produced via very inelastic scattering processes (for example, a scattered electron produced by pion production). The super-elastic locus consists of beam halo and

particles which are classically forbidden (more energetic than elastic particles). An example of a classically forbidden particle is one which skips the magnet and passes directly from the target to the detectors.

The elastic and inelastic space cuts to define these loci of the CED-FPD matrix are defined according to dilution factors extracted from SMS field scan data. In a field scan, the SMS current is varied from 1900 A to 4900 A, in steps of 200 A. This has the effect of moving the scattered particles across the CED-FPD matrix and is explained below. The magnetic field and radius of curvature are inversely proportional to each other. Therefore, an increase in magnetic field will result in a smaller radius of curvature. Similarly, a decrease in magnetic field will result in a larger radius of curvature. Since the FPD is located further from the magnet than the CED, a charged particle which passes through a given CED and FPD under the nominal magnetic field will pass through approximately the same CED and a different FPD under a different magnetic field. Hence, the scattered particles move across the CED-FPD matrix space.

The remainder of the section summarizes the technique employed to extract the dilution factors [70]. For each cell in the electron and pion matrices, a plot of yield versus SMS current is produced. Figure 4.2 is an example of two such plots in the electron matrix. The data points are fitted according to a sum of four functions (2 gaussians, 1 exponential, and 1 linear). According to a  $G^0$  GEANT simulation, the elastic and inelastic contributions to the yield are Gaussian. The exponential fit accounts for low-energy backgrounds such as  $\pi^0$  decay, and the linear fit accounts for randoms.

Based on these fits, elastic and inelastic dilution factors were calculated for each cell in the electron matrix. The elastic dilution factor represents the degree of contamination of the elastic yield at the nominal SMS current. The vertical line in Figure 4.2 represents the nominal SMS current (3500 A) where the total elastic yield

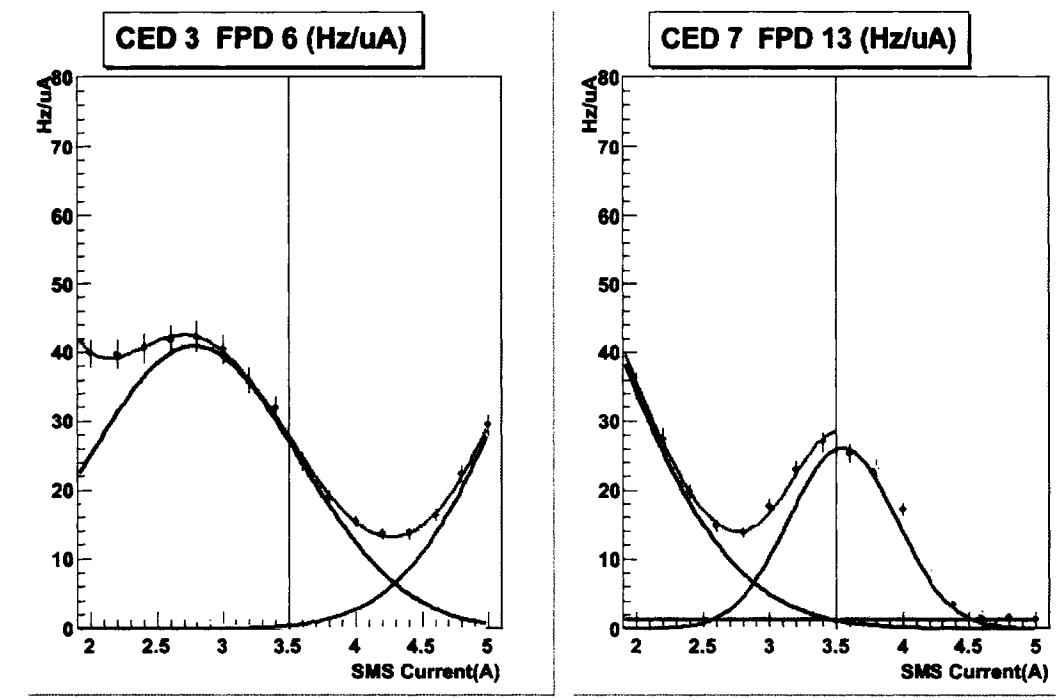


FIG. 4.2:

Measured yield versus SMS current for two representative cells in the CED-FPD electron matrix. The left plot corresponds to cell CED 3/FPD 6 in the inelastic locus and the right plot corresponds to cell CED 7/FPD 13 in the elastic locus. The data points are indicated by black circles. The dark green line over the black circles is a fit to the data, the red line is the elastic contribution to the yield, the blue line is the inelastic contribution to the yield, the yellow line accounts for background and the light green line accounts for randoms [70].

is maximized and the inelastic yield is minimized. Similarly, the inelastic dilution factor represents the degree of contamination of the inelastic yield at the nominal SMS current. The elastic dilution factor is the ratio of the sum of the inelastic, background, and random yields to the total yield

$$d_{elastic}|_{3500A} = \left[ \frac{Y_{gausinelastic} + Y_{exp} + Y_{pol0}}{Y_{total}} \right]_{3500A} \quad (4.9)$$

whereas the inelastic dilution factor is the ratio of the sum of the elastic, background,

and random yields to the total yield

$$d_{inelastic}|_{3500A} = \left[ \frac{Y_{gauselastic} + Y_{exp} + Y_{pol0}}{Y_{total}} \right]_{3500A}. \quad (4.10)$$

Cells having an elastic dilution factor less than 0.2 are defined to be part of the elastic space cut while cells having an inelastic dilution factor less than 0.2 are defined to be part of the inelastic space cut. Figure 4.3 shows the CED-FPD matrix space cuts for hydrogen. The errors on the dilution factors are not established yet as the functional forms of the inelastic, background, background, and random yields are not final. However, looking at the consistency of the dilution factor with various fits and fitting ranges indicate that the error will be better than 20% [71]. Conservatively, this thesis takes the error of an individual dilution factor to be 20%. The average dilution factor of the elastic locus (weighted by the yield) is  $0.121 \pm 0.014$ .

By the same technique, the elastic and inelastic dilution factors of the pion matrix are obtained. Figure 4.4 shows the measured yield versus SMS current for two representative cells in the CED-FPD pion matrix. The left plot corresponds to cell CED 2/FPD 7 and the right plot corresponds to cell CED 6/FPD 12. The data points are fitted according to a sum of three functions (2 gaussians and 1 linear). According to a  $G^0$  Geant simulation, the elastic and inelastic contributions to the yield are Gaussian. The linear fit accounts for randoms. The particles which comprise the elastic Gaussian are actually misidentified elastic electrons [71].

## 4.6 Deadtime

A major correction to the measured number of counts come from data acquisition dead times. Electronic deadtime is caused when an event that should generate a trigger comes in and is missed because the hardware is busy. When a logic gate

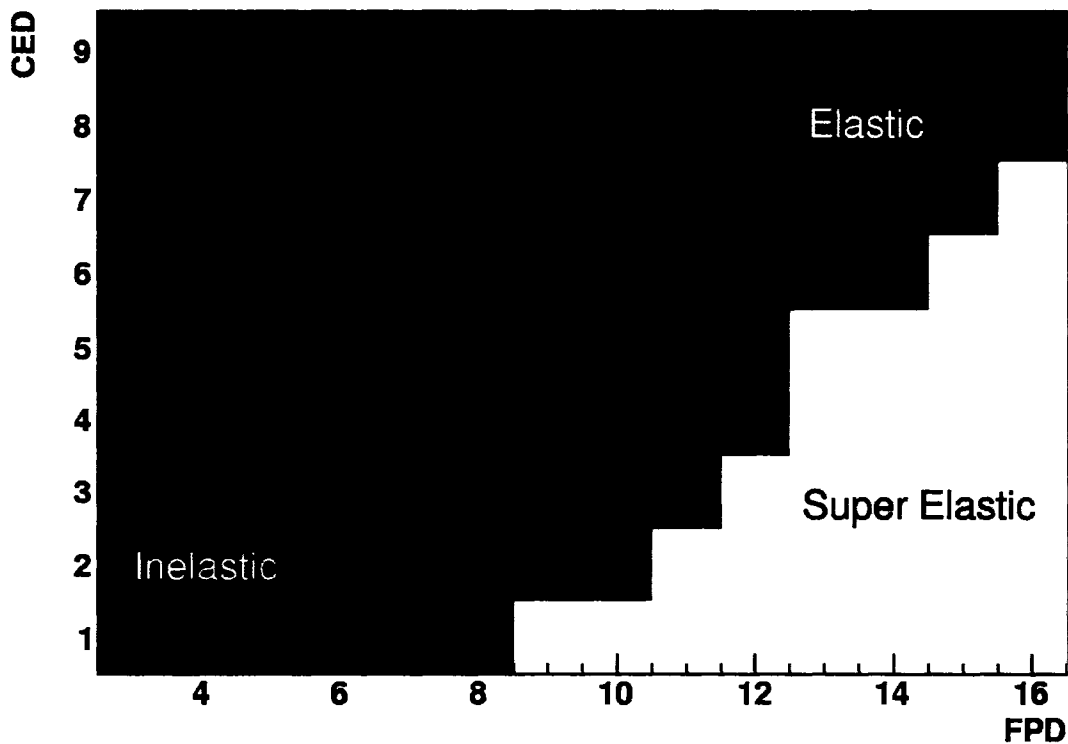


FIG. 4.3: *CED-FPD matrix space cuts for hydrogen. The space cuts are determined according to dilution factors (see text).*

in the trigger is activated, the output signal stays high for a fixed time. If another event tries to activate the gate during the time the output signal is high, the event is ignored. In other words, a hit that occurs too close in time with the previous hit will be missed and the rate will be undercounted. For low rate detectors, this effect is negligible. For detectors firing at 1 MHz, this effect is significant.

The time between adjacent hits in a detector firing at a given rate from unrelated events is governed by an exponential probability function. Suppose a hit triggers the electronics. For a time period  $\tau$  following that hit, the electronics will not respond. The time  $\tau$  is a characteristic deadtime of the electronics. The average “dead” probability of the electronics or the average probability of at least one hit



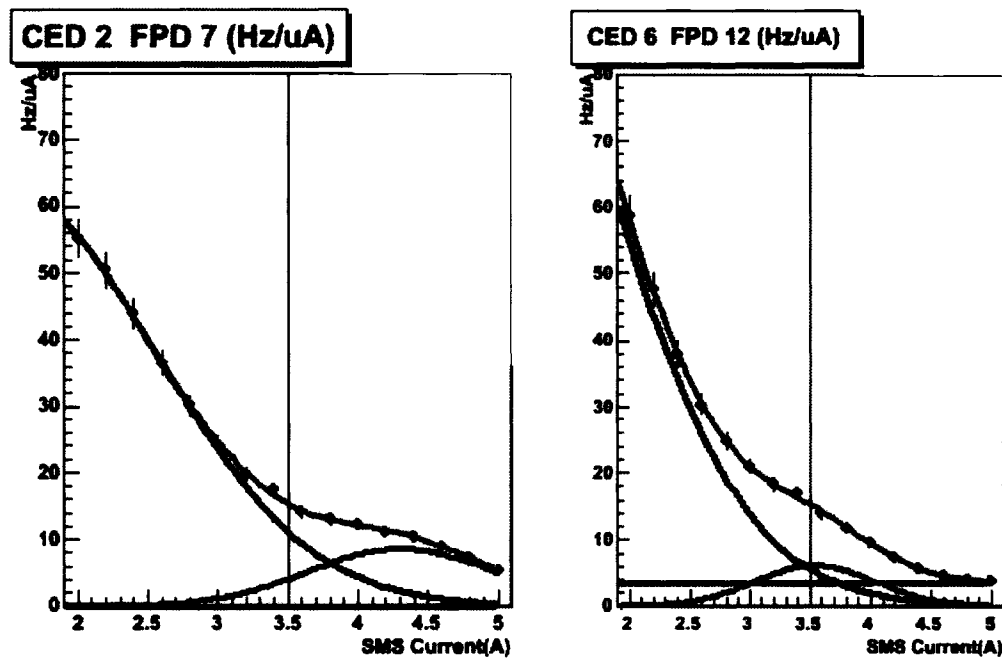


FIG. 4.4:

*Measured yield versus SMS current for two representative cells in the CED-FPD pion matrix. The data points are indicated by black circles. The dark green line over the black circles is a fit to the data, the red line is the elastic contribution to the yield, the blue line is the inelastic contribution to the yield and the light green line accounts for randoms [70].*

occurring during the time window  $\tau$  is

$$f_{dead} = 1 - e^{-R\tau}, \quad (4.11)$$

where  $R$  is the true particle detection rate. For  $R\tau \ll 1$ , the deadtime can be approximated as

$$f_{dead} \simeq R\tau. \quad (4.12)$$

The measured rate  $r$  is proportional to the probability that the detector does not fire during the deadtime

$$r = (1 - f_{dead}) R. \quad (4.13)$$

Normalizing both the measured and true particle detection rates in Equation 4.13 to the beam current, we have

$$Y_{meas} = (1 - f_{dead}) Y_t, \quad (4.14)$$

where  $Y_{meas} = r/Q$  and  $Y_t = R/Q$  are the normalized measured and true detector yields, respectively. Substituting Equation 4.12 into Equation 4.14 gives

$$Y_{meas} = (1 - R\tau) Y_t = (1 - Y_t Q\tau) Y_t = Y_t - Y_t^2 Q\tau. \quad (4.15)$$

So the parity-violating asymmetry  $A(Y_{meas})$  carried by the measured yield  $Y_{meas}$  is related to the parity-violating asymmetry  $A(Y_t)$  carried by the true yield  $Y_t$  and the asymmetry  $A(Q)$  carried by the charge [72] by

$$\begin{aligned} A(Y_{meas}) &= A(Y_t - Y_t^2 Q\tau) \\ &= \frac{Y_t}{Y_t - Y_t^2 Q\tau} A(Y_t) - \frac{Y_t^2 Q\tau}{Y_t - Y_t^2 Q\tau} A(Y_t^2 Q\tau) \\ &= \frac{1}{1 - f_{dead}} A(Y_t) - \frac{f_{dead}}{1 - f_{dead}} A(Y_t^2 Q\tau) \\ &= \frac{1}{1 - f_{dead}} A(Y_t) - \frac{f_{dead}}{1 - f_{dead}} (2A(Y_t) + A(Q)) \\ &= A(Y_t) - \frac{f_{dead}}{1 - f_{dead}} (A(Y_t) + A(Q)), \end{aligned} \quad (4.16)$$

where we make use of the mathematical identities in Appendix A. Equation 4.16 is an important result. It shows that the false asymmetry associated with deadtime

$$A_{false} = \frac{f_{dead}}{1 - f_{dead}} (A(Y_t) + A(Q)), \quad (4.17)$$

is made up of both the true asymmetry and the charge asymmetry. A simple rearrangement of Equation 4.16 gives the parity-violating asymmetry carried by the true yield  $Y_t$

$$A(Y_t) = \frac{A(Y_{meas})(1 - f_{dead}) + f_{dead} A(Q)}{1 - 2f_{dead}}. \quad (4.18)$$

As shown here, the deadtime correction depends on the the raw asymmetry, the dilution factor, and the charge asymmetry. Therefore, the error associated with the deadtime correction has both statistical and systematic components. The statistical part of the error is added in quadrature to the main statistical error.

One approach to determine  $f_{dead}$  is to plot the normalized yield versus beam current (see Figure 4.5). This approach was used to perform a crude deadtime correction for the purpose of studying linear regression slopes (see Section 4.7). The term “crude” refers to the fact that the technique does not separate the sources of the deadtime. The derivation that follows is adapted from [74]. The CED-FPD coincidence rate is a combination of the real and random (accidental) coincidence rates

$$r = r_{real} - r_{random}, \quad (4.19)$$

where  $r_{real}$  is proportional the the beam current

$$r_{real} = p_0 I \quad (4.20)$$

and  $r_{random}$  is proportional to the square of the beam current

$$\begin{aligned} r_{random} &= r_{CED} r_{FPD} \Delta t \\ &= (p_{CED} I) (p_{FPD} I) \Delta t \\ &= (p_{CED} p_{FPD} \Delta t) I^2 \\ &= p_1 I^2. \end{aligned} \quad (4.21)$$

The quantity  $\Delta t$  is expected to be the sum of the widths of the CED and FPD timing gates. Substituting Equations 4.20 and 4.21 into Equation 4.19 yields

$$r = p_0 I - p_1 I^2. \quad (4.22)$$

Dividing Equation 4.22 by the beam currents gives

$$Y_{meas} = p_0 - p_1 I. \quad (4.23)$$

Equation 4.23 is a straight line, where the y-intercept is the normalized rate of real coincidences and the deadtime is

$$f_{dead} = -p_1 \frac{I}{p_0}. \quad (4.24)$$

Substituting Equation 4.24 into Equation 4.14 gives the normalized true detector yield

$$Y_t = \frac{Y_{meas}}{1 - f_{dead}} = \frac{Y_{meas}}{1 + p_1 I / p_0}. \quad (4.25)$$

The results of the deadtime correction are summarized in Tables 4.2 and 4.3. The systematic difference between the deadtime slopes for NA and French octants is not unexpected, given their somewhat different electronics.

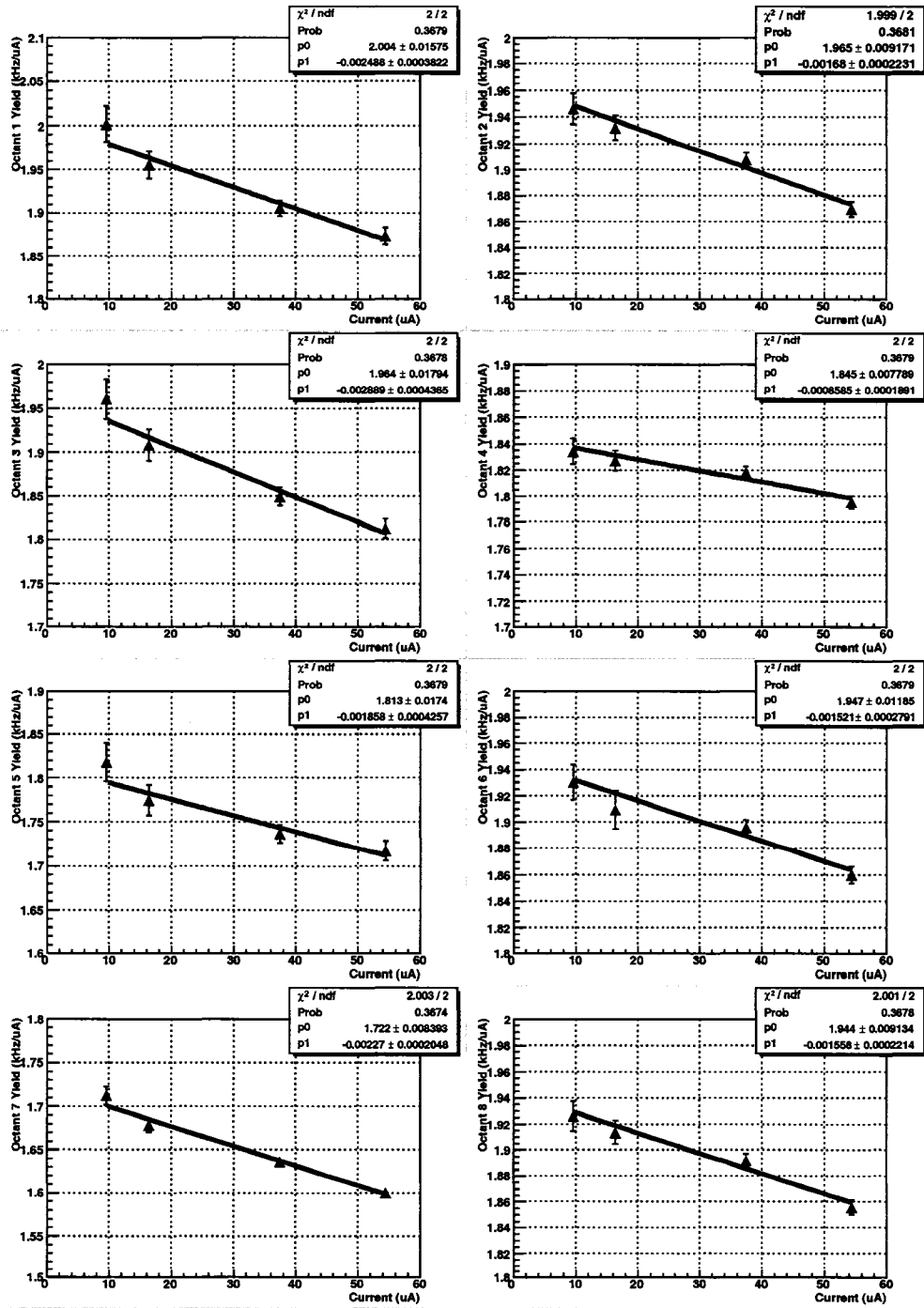


FIG. 4.5: Normalized yield versus beam current for each octant. North American octants are in the left column and French octants are in the right column. The plots are fitted to a line and the parameters are displayed in a statistics box at the top of each plot. The errors on the normalized yield are scaled by a factor, the square root of the reduced  $\chi^2$ . The parameter  $p_0$  is the intercept and  $p_1$  is the slope. The data are from current scans 28988-28991.

Octant	$p_0$ (KHz/ $\mu$ A)	$p_1$ (KHz/ $(\mu$ A) $^2$ )	$f_{dead}$ (%)	$A_{false}$ (ppm)
1	$2.00 \pm 0.02$	$-0.0025 \pm 4E-4$	$7.50 \pm 1.15$	$3.77 \pm 1.46$
2	$1.97 \pm 0.01$	$-0.0017 \pm 2E-4$	$5.18 \pm 0.68$	$2.42 \pm 0.89$
3	$1.96 \pm 0.02$	$-0.0029 \pm 4E-4$	$8.88 \pm 1.34$	$4.58 \pm 1.79$
4	$1.85 \pm 0.01$	$-0.0008 \pm 2E-4$	$2.59 \pm 0.61$	$1.40 \pm 0.59$
5	$1.81 \pm 0.02$	$-0.0019 \pm 4E-4$	$6.30 \pm 1.41$	$2.44 \pm 1.27$
6	$1.95 \pm 0.01$	$-0.0015 \pm 3E-4$	$4.62 \pm 0.86$	$1.23 \pm 0.74$
7	$1.72 \pm 0.01$	$-0.0023 \pm 2E-4$	$8.02 \pm 0.72$	$0.94 \pm 1.42$
8	$1.94 \pm 0.01$	$-0.0016 \pm 2E-4$	$4.95 \pm 0.69$	$2.58 \pm 0.90$

TABLE 4.2: Results of the deadtime correction.  $p_0$  and  $p_1$  are the intercept and slope of normalized yield versus beam current, respectively. The deadtime  $f_{dead}$  and false asymmetry  $A_{false}$  are calculated at the nominal beam current  $60 \mu$ A.

NA	French
1.24	0.855
1.47	0.465
1.02	0.781
1.32	0.801

TABLE 4.3: Deadtime slopes presented as  $p_1/p_0$  in units of  $\%/ \mu$ A ( $10^{-3}$ ), where  $p_0$  is the intercept and  $p_1$  is the slope.

## 4.7 Linear Regression

If  $Y_{meas}^+$  or  $Y_{meas}^-$  in Equation 4.1 changes because of anything other than the spin physics of the interaction, then it is a false asymmetry. This results in the seemingly unattainable golden rule for parity experiments: no beam property other than the beam polarization should change when the beam polarization reverses sign. Anything that changes with helicity-reversal is said to be helicity-correlated. The beam parameters monitored for helicity-correlation are:

$$\text{charge asymmetry} = \frac{I_+ - I_-}{I_+ + I_-} \quad (4.26)$$

$$\text{x position difference} = x_+ - x_- \quad (4.27)$$

$$\text{y position difference} = y_+ - y_- \quad (4.28)$$

$$\text{x angle difference} = \theta_{x+} - \theta_{x-} \quad (4.29)$$

$$\text{y angle difference} = \theta_{y+} - \theta_{y-} \quad (4.30)$$

$$\text{energy difference} = E_+ - E_- \quad (4.31)$$

### 4.7.1 Formalism

The formalism and derivations that follow are taken from [75]. The measured yield  $Y_{meas}^\pm$  is a combination of the parity-violating yield  $Y_{pv}^\pm$  and the yield due to helicity-correlations in beam parameters  $Y_{hc}^\pm$

$$Y_{meas}^\pm = Y_{pv}^\pm + Y_{hc}^\pm, \quad (4.32)$$

where the superscript  $\pm$  indicates the positive or negative helicity state. If we assume a linear relationship between the helicity-correlated yield and the beam parameters  $P_m$ , then

$$Y_{hc}^\pm = \sum_m \frac{\partial Y_{hc}^\pm}{\partial P_m} P_m^\pm, \quad (4.33)$$

where  $\frac{\partial Y_{hc}^\pm}{\partial P_m}$  is the correlation slope or the detector response to the beam parameter. To simplify this notation, we rewrite the correlation slope as  $\frac{\partial Y_{hc}^\pm}{\partial P_m} \equiv C_m$ . Equation 4.33 then becomes

$$Y_{hc}^\pm = \sum_m C_m P_m^\pm, \quad (4.34)$$

and Equation 4.32 can be written as

$$Y_{meas}^\pm = Y_{pv}^\pm + \sum_m C_m P_m^\pm. \quad (4.35)$$

Making this substitution into the measured asymmetry

$$A_{meas} = \frac{Y_{meas}^+ - Y_{meas}^-}{Y_{meas}^+ + Y_{meas}^-} \quad (4.36)$$

gives

$$A_{meas} = \frac{Y_{pv}^+ - Y_{pv}^- + \sum_m C_m (P_m^+ - P_m^-)}{Y_{pv}^+ + Y_{pv}^- + \sum_m C_m (P_m^+ + P_m^-)}. \quad (4.37)$$

Assuming that  $Y_{pv}^\pm \gg \sum_m C_m P_m^\pm$ , then

$$\begin{aligned} A_{meas} &\simeq \frac{Y_{pv}^+ - Y_{pv}^- + \sum_m C_m \Delta P_m}{Y_{pv}^+ + Y_{pv}^-} \\ &\simeq \frac{Y_{pv}^+ - Y_{pv}^-}{Y_{pv}^+ + Y_{pv}^-} + \sum_m C_m \frac{\Delta P_m}{Y_{pv}^+ + Y_{pv}^-} \\ &\simeq A_{pv} + \sum_m C_m \frac{\Delta P_m}{2\langle Y \rangle}, \end{aligned} \quad (4.38)$$

where  $\Delta P_m$  is the beam parameter difference

$$\Delta P_m = P_m^+ - P_m^-, \quad (4.39)$$

and the average yield is given by  $\langle Y \rangle = \frac{1}{2}(Y_{pv}^+ + Y_{pv}^-)$ . Therefore, the false asymmetry due to helicity-correlations in beam parameters is

$$A_{false} = \sum_m C_m \frac{\Delta P_m}{2\langle Y \rangle} \quad (4.40)$$

and depends on the correlation slope, beam parameter difference, and average yield.

The net change of the yield  $\delta Y$  is

$$\delta Y = \sum_{m=1}^{m=n} C_m \delta P_m, \quad (4.41)$$

where  $n$  is the number of independent beam parameters, and  $\delta Y \equiv Y - \langle Y \rangle$  and  $\delta P_m \equiv P_m - \langle P_m \rangle$  are the deviations of the measured yield and beam parameter  $P_m$ , respectively, from the means of their parent distributions.  $C_m$  can be determined by the least-squares method, with  $\chi^2$  defined as

$$\chi^2 = \sum_i \frac{(\delta Y^i - \sum_m C_m \delta P_m^i)^2}{(\sigma^i)^2}, \quad (4.42)$$



where  $\sigma^i$  is the uncertainty of  $\delta Y - \sum_m C_m \delta P_m$  in measurement  $i$ . The best values for  $C_m$  are obtained by minimizing  $\chi^2$ . Therefore,  $C_m$  is determined by the constraint that

$$\frac{\partial \chi^2}{\partial C_m} = 0. \quad (4.43)$$

This leads to a set of  $n$  equations

$$\sum_i \frac{\delta P_k^i}{(\sigma^i)^2} \left( \delta Y^i - \sum_m C_m \delta P_m^i \right) = 0. \quad (4.44)$$

If we assume that all  $N$  measurements have the same statistical weight ( $\sigma^i = \sigma$ ), then Equation 4.44 becomes

$$\langle \delta P_k \delta Y \rangle = \sum_m C_m \langle \delta P_k \delta P_m \rangle, \quad (4.45)$$

where we have replaced  $\sum_i$  with the straight average of  $N$  measurements  $\langle \rangle$ . Here,  $\langle \delta P_k \delta Y \rangle$  is the average product of the deviations of  $P_k$  and  $Y$  and is the vector covariance between the yield and the beam parameters, while  $\langle \delta P_k \delta P_m \rangle$  is the average product of the deviations of  $P_k$  and  $P_m$  and is the covariance matrix of the beam parameters. Covariance provides a measure of how strong the correlation is between two different quantities. The covariance for two random variables  $x$  and  $y$  is defined as

$$\begin{aligned} \langle \delta x \delta y \rangle &\equiv \langle (x - \bar{x})(y - \bar{y}) \rangle \\ &= \langle xy - x\bar{y} - \bar{x}y + \bar{x}\bar{y} \rangle \\ &= \langle xy \rangle - \langle x \rangle \langle y \rangle. \end{aligned} \quad (4.46)$$

For uncorrelated variables, the covariance is zero. During event by event processing, we keep track of the running averages of  $x$ ,  $y$ , and  $xy$ . At the end of the replay,  $\langle \delta x \delta y \rangle$  is computed.

Equation 4.45 can be written in matrix form

$$\vec{\xi} = \vec{M} \vec{C}, \quad (4.47)$$

where

$$\vec{\xi} \equiv \begin{bmatrix} \langle \delta P_1 \delta Y \rangle \\ \langle \delta P_2 \delta Y \rangle \\ \cdot \\ \cdot \\ \cdot \\ \langle \delta P_n \delta Y \rangle \end{bmatrix}, \vec{\mathcal{M}} \equiv \begin{bmatrix} \langle \delta P_1 \delta P_1 \rangle & \delta P_1 \delta P_2 & \dots \\ \langle \delta P_2 \delta P_1 \rangle & \delta P_2 \delta P_2 & \dots \\ \cdot & \cdot & \cdot \\ \cdot & \cdot & \cdot \\ \cdot & \cdot & \cdot \\ \langle \delta P_n \delta P_1 \rangle & \delta P_n \delta P_2 & \dots \end{bmatrix}, \vec{c} \equiv \begin{bmatrix} C_1 \\ C_2 \\ \cdot \\ \cdot \\ \cdot \\ C_n \end{bmatrix}. \quad (4.48)$$

Equation 4.47 is a set of  $n$  linear equations with  $n$  unknowns ( $C_m$ ) and can be solved by inverting  $\vec{\mathcal{M}}$

$$\vec{c} = \vec{\mathcal{M}}^{-1} \vec{\xi}. \quad (4.49)$$

Computationally, it is more efficient to solve this system by LU decomposition. The details of this technique are given in [76]. Suppose we are able to write the matrix  $\vec{\mathcal{M}}$  as a product of two matrices

$$\vec{L} \vec{U} = \vec{\mathcal{M}}, \quad (4.50)$$

where  $\vec{L}$  is lower triangular (has elements only on the diagonal and below) and  $\vec{U}$  is upper triangular (has elements only on the diagonal and above). For the case of a  $4 \times 4$  matrix  $\vec{\mathcal{M}}$ , for example, Equation 4.50 would look like

$$\begin{bmatrix} \alpha_{11} & 0 & 0 & 0 \\ \alpha_{21} & \alpha_{22} & 0 & 0 \\ \alpha_{31} & \alpha_{32} & \alpha_{33} & 0 \\ \alpha_{41} & \alpha_{42} & \alpha_{43} & \alpha_{44} \end{bmatrix} \begin{bmatrix} \beta_{11} & \beta_{12} & \beta_{13} & \beta_{14} \\ 0 & \beta_{22} & \beta_{23} & \beta_{24} \\ 0 & 0 & \beta_{33} & \beta_{34} \\ 0 & 0 & 0 & \beta_{44} \end{bmatrix} = \begin{bmatrix} a_{11} & a_{12} & a_{13} & a_{14} \\ a_{21} & a_{22} & a_{23} & a_{24} \\ a_{31} & a_{32} & a_{33} & a_{34} \\ a_{41} & a_{42} & a_{43} & a_{44} \end{bmatrix} \quad (4.51)$$

We can use a decomposition such as Equation 4.51 to solve the linear set

$$\vec{\mathcal{M}} \vec{c} = (\vec{L} \vec{U}) \vec{c} = \vec{L} (\vec{U} \vec{c}) = \vec{\xi} \quad (4.52)$$

by first solving for the vector  $\vec{y}$  such that

$$\overleftarrow{L}\vec{y} = \vec{\xi} \quad (4.53)$$

and then solving

$$\overleftarrow{U}\vec{c} = \vec{y}. \quad (4.54)$$

The advantage of breaking up one linear set into two linear successive ones is that the solution of a triangular set of equations is quite trivial. Thus, Equation 4.53 can be solved by forward substitution as follows

$$\begin{aligned} y_1 &= \frac{\xi_1}{\alpha_{11}} \\ y_i &= \frac{1}{\alpha_{ii}} \left[ \xi_i - \sum_{j=1}^{i-1} \alpha_{ij} y_j \right], \end{aligned} \quad (4.55)$$

while Equation 4.54 can be solved by backward substitution

$$\begin{aligned} c_N &= \frac{y_N}{\beta_{NN}} \\ c_i &= \frac{1}{\beta_{ii}} \left[ y_i - \sum_{j=i+1}^N \beta_{ij} x_j \right]. \end{aligned} \quad (4.56)$$

The statistical uncertainty of  $C_m$  is determined according to the curvature matrix of  $\chi^2$ . The curvature matrix  $\alpha_{lk}$  is the second cross partial derivative of  $\chi^2$  with respect to two arbitrary correlation slopes  $C_l$  and  $C_k$

$$\alpha_{lk} \equiv \frac{1}{2} \frac{\partial^2 \chi^2}{\partial C_l \partial C_k} = \sum_i \frac{\delta P_l^i \delta P_k^i}{(\sigma^i)^2} = \frac{1}{\sigma^2/N} \langle \delta P_l \delta P_k \rangle = \frac{1}{\sigma^2/N} \mathcal{M}_{lk} \quad (4.57)$$

for all  $k$  and  $l$ . The inverse of the curvature matrix is the error matrix  $\epsilon$

$$\overleftarrow{\epsilon} \equiv \overleftarrow{\alpha}^{-1} = \frac{\sigma^2}{N} \overleftarrow{\mathcal{M}}^{-1}. \quad (4.58)$$

## 4.7.2 Slope Stability

To examine the stability of the slopes over time, the slopes of the six beam parameters determined using natural beam motion are plotted versus run number

over the duration of the run for all eight octants. The  $x$  slopes are shown in Figure 4.6. It is interesting to note that the slopes in every octant are correlated with each other. For example, a run which has a big  $x$  slope in octant 1 also has big slopes in every other octant. The run-by-run fluctuations are much larger than their corresponding statistical uncertainties. An initial hypothesis was that systematic effects such as beam halo could change the sensitivities of the detectors. A study of the run-by-run fluctuations, as will be discussed later, revealed that the large and unphysical slopes are the result of a sometimes ineffectual beam trip cut. The other five beam parameters exhibit strikingly similar behavior. Figure 4.7 shows the slopes of the six beam parameter versus run number for a typical octant.

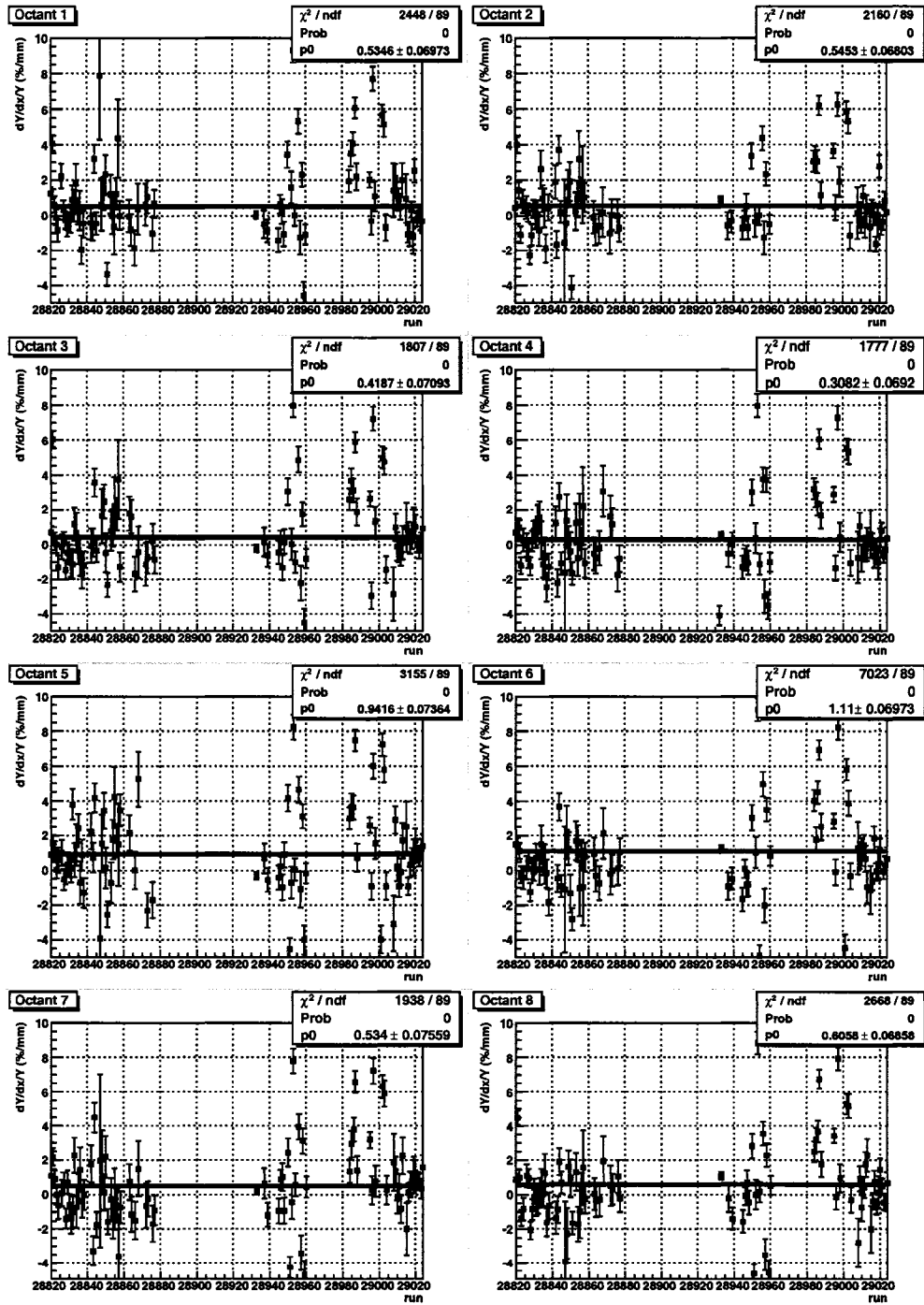


FIG. 4.6: Run-by-run fluctuations of the  $x$  slopes as determined using natural beam motion over the duration of the run for all eight octants. The absence of slopes during the middle of the run period corresponds to a time when the 4K helium supply was lost. The slopes are fitted to a constant,  $p_0$ . Results for the other beam parameters are similar.

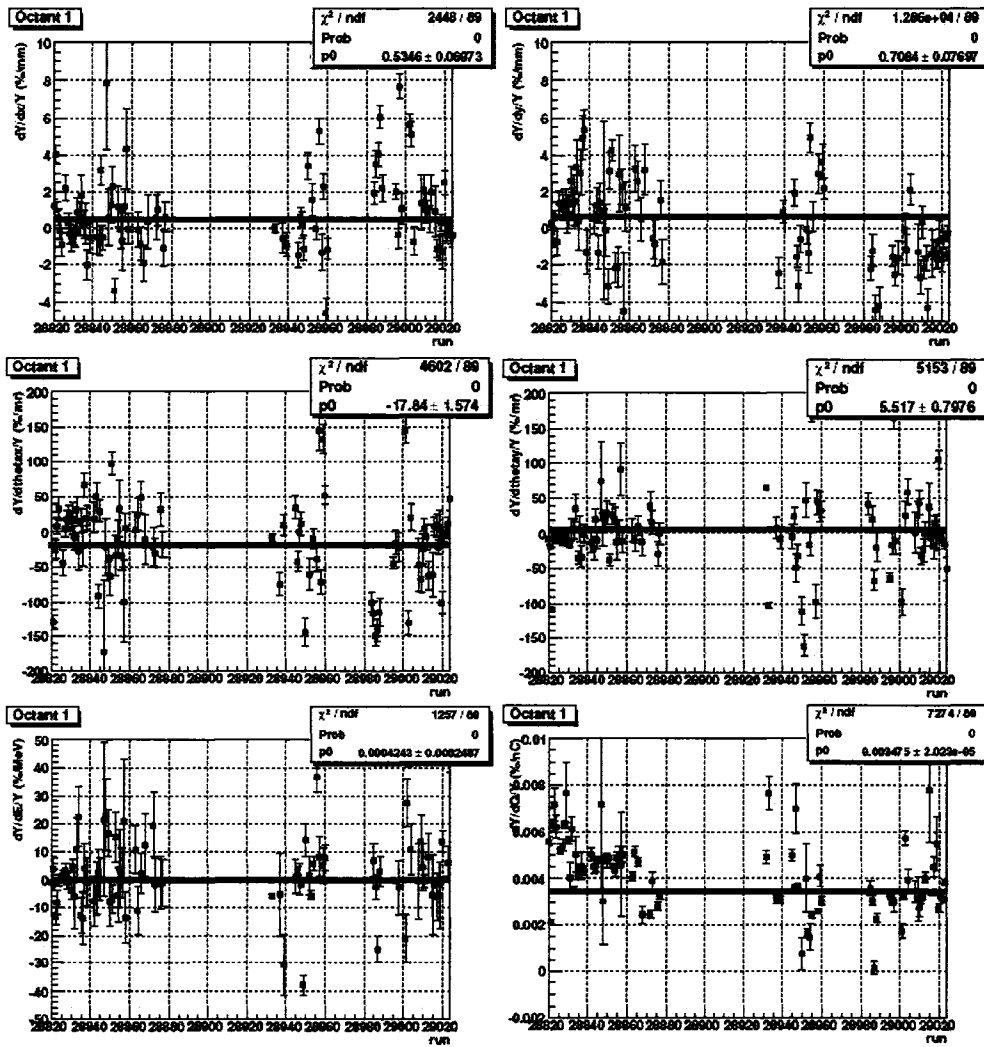


FIG. 4.7: Run-by-run fluctuations of the slopes of the six beam parameter as determined using natural beam motion over the duration of the run for octant 1. The absence of slopes during the middle of the run period corresponds to a time when the 4K helium supply was lost. The slopes are fitted to a constant,  $p_0$ . Results for other octants are similar.

### 4.7.3 Slopes Before and After Deadtime

To investigate the geometrical sensitivity of individual octant to the beam positions and angles, the average slopes of the spatial beam parameters of the production run determined by natural beam motion are plotted against the average  $\Phi$  of each octant. The average slope of an octant is calculated by weighing each individual slope by the inverse of the square of its corresponding error. The error of an individual slope represents a combination of factors: the statistical error (the number of mps), beam noise or jitter, and BPM noise. The error associated with the average slope of an octant is the standard deviation of the individual slopes divided by the square root of the number of runs which yielded slopes. The reason for taking the standard deviation of the individual slopes versus a simple propagation of errors is because of the large run-by-run fluctuations discussed in Section 4.7.2. Consequently, the error associated with the average slope of an octant completely ignores the errors of the individual slopes of that octant calculated from the linear regression. Since the spectrometer is azimuthally symmetric, octants that are located opposite of each other should ideally have sensitivities to beam position and angle that are equal in magnitude and opposite in sign. Octants 3 and 7 are located on the x-axis so one would expect their  $x$  and  $\theta_x$  slopes to be greatest. Since octants 1 and 5 are located on the y-axis, one would expect their  $x$  and  $\theta_x$  slopes to be smallest. Hence, the  $x$  and  $\theta_x$  slopes should vary like cosine with the average  $\Phi$  of each octant. By similar logic, the  $y$  and  $\theta_y$  slopes should vary sinusoidally with the average  $\Phi$  of each octant.

Ideally, linear regression is performed after the deadtime correction. However, since deadtime is not well understood at this time, a complete deadtime correction has not yet been implemented. Therefore, linear regression was performed first. In Figure 4.8, the average slopes (not corrected for deadtime) determined by natural beam motion are plotted against the average  $\Phi$  of each octant. To see how the slopes

behave after the bulk of the charge dependence (much of which presumably arises due to deadtime) is removed, a crude deadtime correction was performed followed by a re-calculation of the linear regression slopes. The technique and results of the crude deadtime correction are provided in Section 4.6. For comparison, the average deadtime corrected slopes determined by natural beam motion are plotted against the average  $\Phi$  of each octant and overlaid in the same Figure as the average slopes not corrected for deadtime (see Figure 4.8). The octant number and average  $\Phi$  are related according to Figure 4.9. All of the spatial parameters ( $x$ ,  $y$ ,  $\theta_x$ , and  $\theta_y$ ) appear to be unaffected by the deadtime correction. This is the result of large error bars derived from the large run-by-run fluctuations shown in Figure 4.6. Note the unusually good  $\chi^2$  for each fit. The charge slopes exhibit an odd versus even octant dependence after the deadtime correction. This can be attributed to differences in electronics between the North American (1,3,5,7) and French (2,4,6,8) octants. A similar pattern was observed in the forward angle experiment [77]. According to the charge plot, the crude deadtime correction appears to over-correct. If the correction were perfect, the charge slope after the crude deadtime correction would be zero. From the charge plot, the combined effect of random coincidences and deadtime is about -2% ( $-0.001\%/nC \times 2000 \text{ nC/MPS}$ ) at  $60 \mu\text{A}$ . According to the results of the crude deadtime correction (see Table 4.2), the combined effect of random coincidences and deadtime at  $60 \mu\text{A}$  ranges from about -2% to -10% (depending upon octant number).



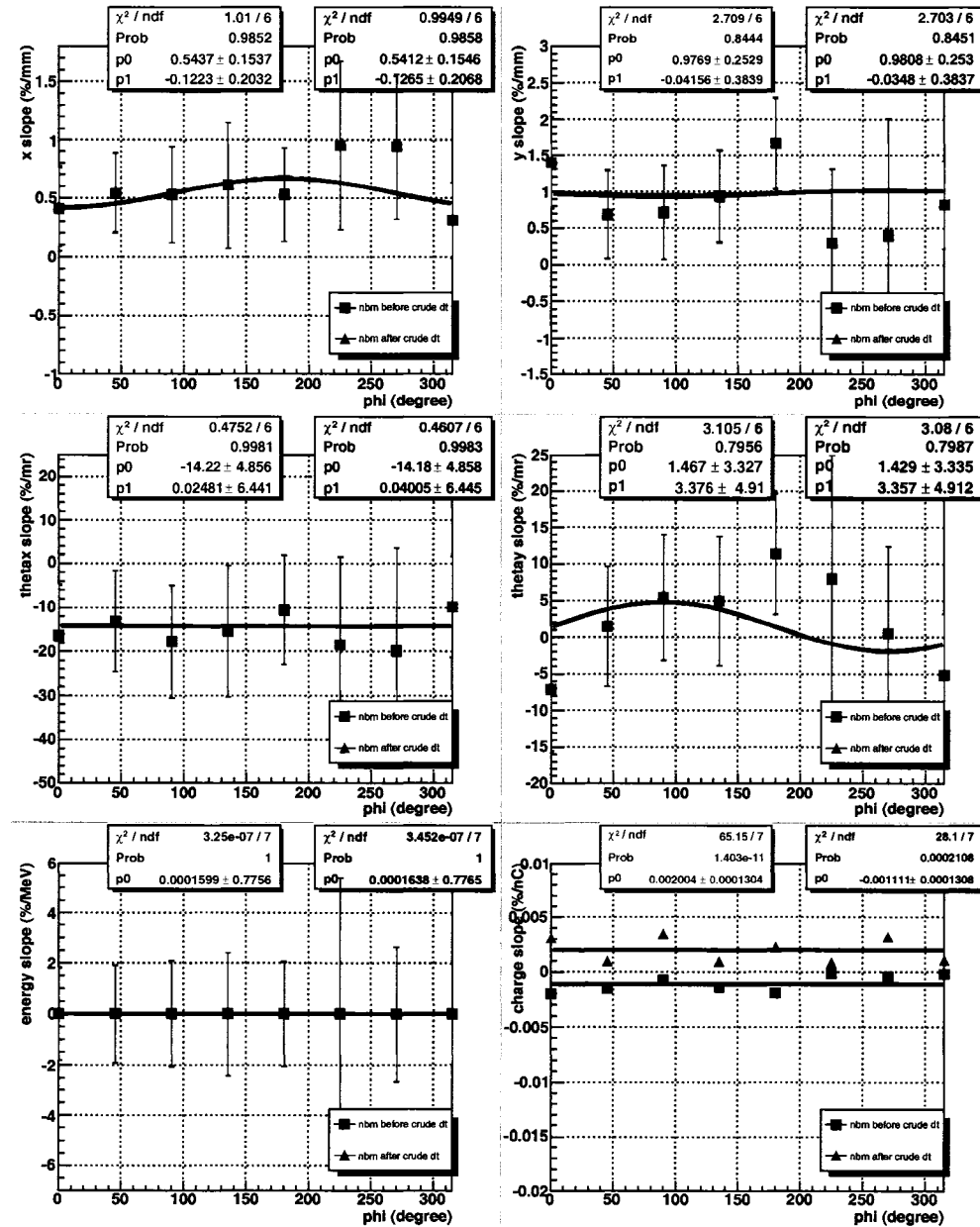


FIG. 4.8:

Average slope determined using natural beam motion versus average  $\Phi$  of each octant before (blue) and after (pink) a crude deadtime correction. The  $x$  and  $\theta_x$  slopes are fitted according to a cosine function and the  $y$  and  $\theta_y$  slopes are fitted according to a sine function. In both cases, the phase is fixed at zero. The parameter  $p_0$  is the offset and  $p_1$  is the amplitude. The  $E$  and  $Q$  slopes are fitted to a constant. The parameter  $p_0$  is the constant. The  $|\chi^2|$   $\chi^2$  probability, and parameters are displayed in a statistics box at the top of each plot. The slopes correspond to the elastic electron locus.

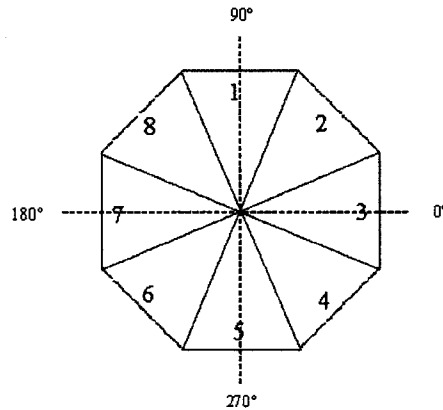


FIG. 4.9:  
*Relationship between octant number and average  $\Phi$ .*

The same plot was produced for coil modulation data (see Figure 4.10). As discussed later, coil modulation was only enabled for a small fraction of the runs. In contrast to natural beam motion, the slopes of all of the spatial parameters change after the crude deadtime correction. Consistent with natural beam motion, the crude deadtime correction appears to over-correct. According to the charge plot, the combined effect of random coincidences and deadtime is about -4% at 60  $\mu\text{A}$ . From this point on, any reference to slope will refer to the deadtime corrected slope.

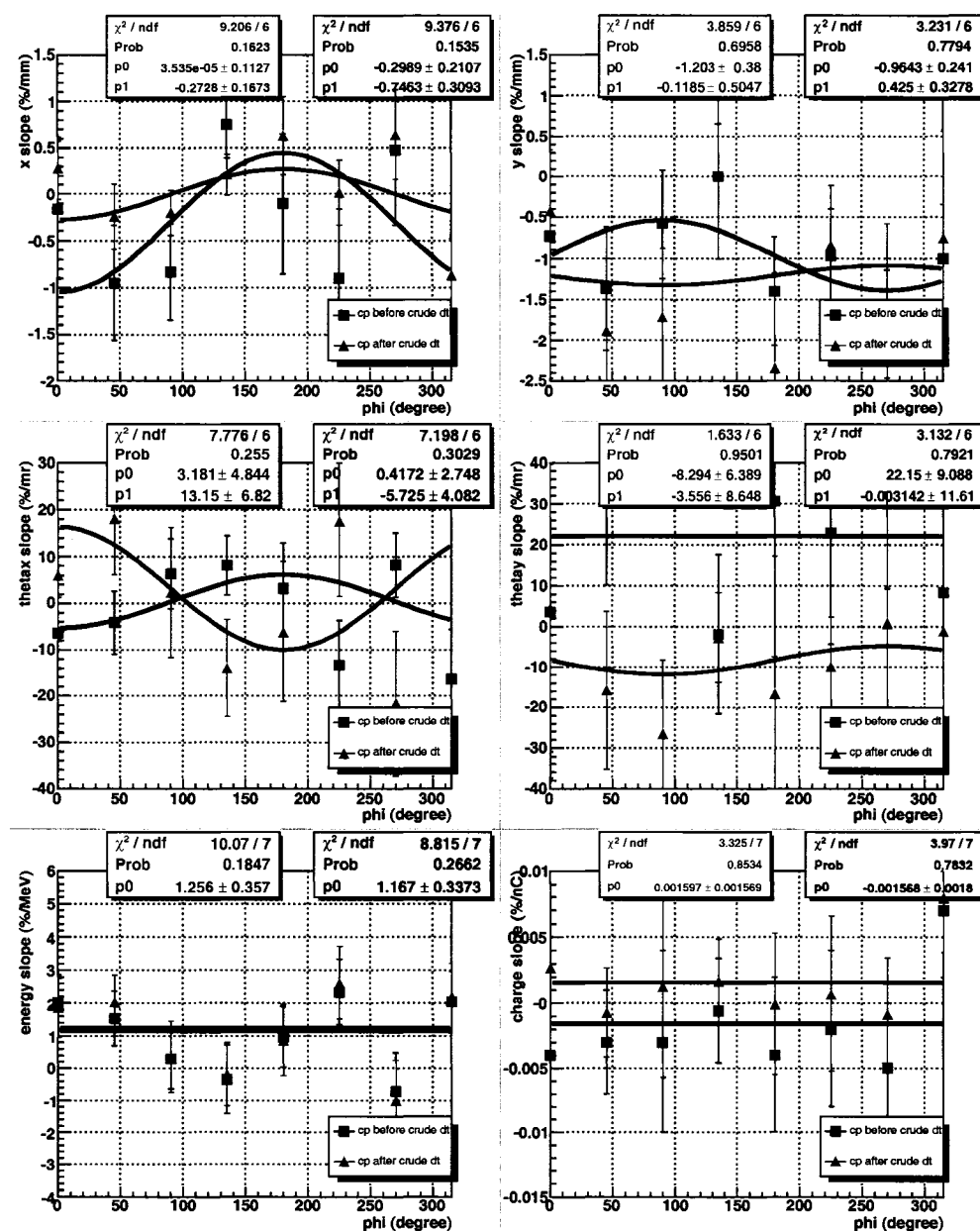


FIG. 4.10:

Average slope determined using coil modulation versus average  $\Phi$  of each octant before (blue) and after (pink) a crude deadtime correction. The  $x$  and  $\theta_x$  slopes are fitted according to a cosine function and the  $y$  and  $\theta_y$  slopes are fitted according to a sine function. In both cases, the phase is fixed at zero. The parameter  $p_0$  is the offset and  $p_1$  is the amplitude. The  $E$  and  $Q$  slopes are fitted to a constant. The parameter  $p_0$  is the constant. The  $|\chi^2|$   $\chi^2$  probability, and parameters are displayed in a statistics box at the top of each plot. The slopes correspond to the elastic electron locus.

#### 4.7.4 A Comparison of Raw and Corrected Yields

Figure 4.11 shows the raw and corrected elastic electron locus yield for a typical octant versus the six beam parameters ( $x$ ,  $y$ ,  $\theta_x$ ,  $\theta_y$ ,  $E$ , and  $Q$ ) for a typical run. The corrections are based on the slopes determined using natural beam motion for that run and are applied to the natural beam motion of that run. According to the plots, the corrected slopes mostly flatten out the dependence of the detector's yield on the six beam parameters. The run selected here was not one with "outlier" slopes as discussed above, and one sees from Figure 4.11 that for non-outlier runs the slopes as determined from linear regression of natural beam motion are reasonable and should allow a meaningful correction for helicity-correlated beam motion.

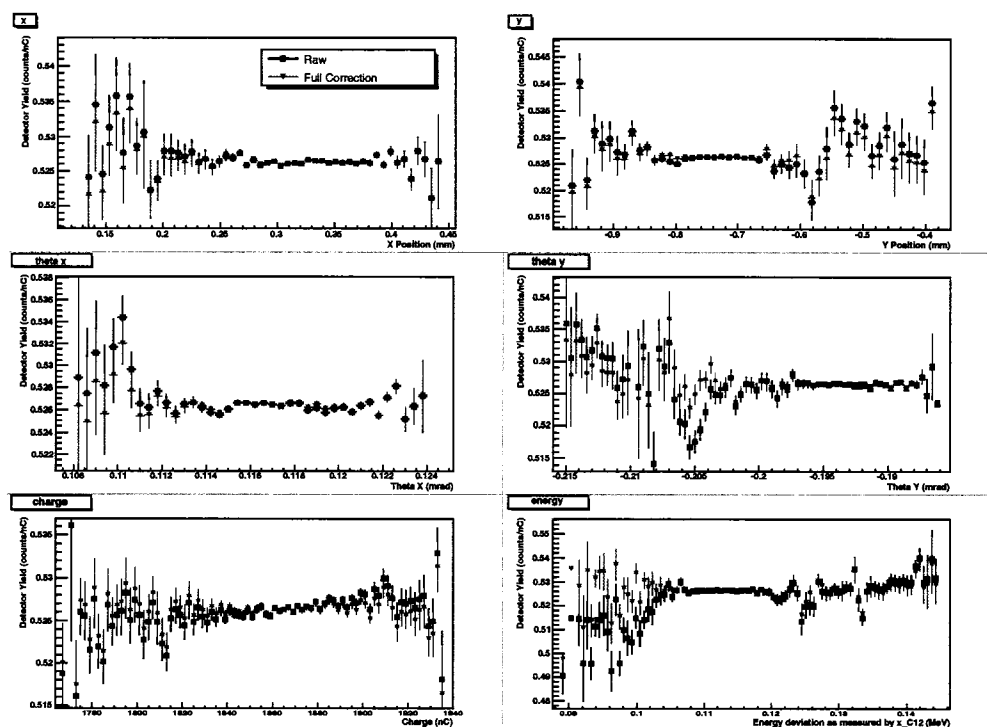


FIG. 4.11: *The raw and corrected elastic electron locus yield vs beam parameters for octant 1 in run 29023. The corrections are based on slopes determined using natural beam motion for that run and are applied to natural beam motion of that run.*

### 4.7.5 Target Projections by Different Sets of BPMs

The beam position and angle are projected onto the target based on BPMs H00 and G0B. BPM H00 was selected for the reason that it provides the greatest lever arm to BPM G0B while maintaining a path free of any magnetic elements. BPM H00 is 3.254 m upstream of the standard pivot center of Hall C while BPM G0B is 15.755 m downstream of the standard pivot center of the Hall C. The distance between H00 and G0B is 19.009 m.

The beam angle and position on the target are calculated according to

$$\tan \theta = \frac{x_1 - x_2}{d_{x_1x_2}} \quad (4.59)$$

and

$$\begin{aligned} x_{targ} &= \frac{x_1 + x_2}{2} - c \\ &= \frac{x_1 + x_2}{2} - \tan \theta d_{midtarg}, \end{aligned} \quad (4.60)$$

where  $d_{x_1x_2}$  is the distance between the two BPMs and  $d_{midtarg}$  is the distance between the target and the midpoint of the two BPMs (see Figure 4.12).

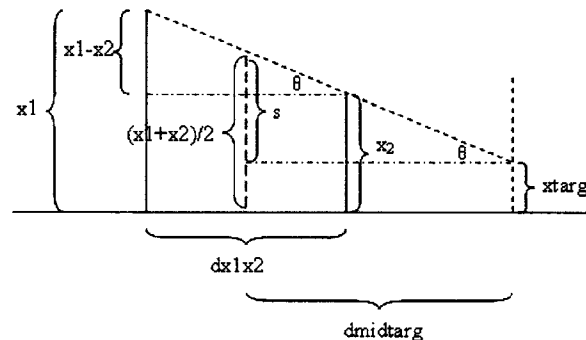


FIG. 4.12: A diagram showing the position and angle projection onto the target.

To study the effects of using different upstream BPMs to project the beam position and angle onto the target, the slopes determined using natural beam motion were re-calculated based on BPMs G0 and G0B (as was done in the forward angle experiment). BPM G0 is 13.206 m downstream of the standard pivot center of Hall C. The distance between G0 and G0B is 2.549 m. In Figure 4.13, the average slopes determined using BPMs G0 and G0B are plotted versus the average  $\Phi$  of each octant. The average slopes determined using BPMs H00 and G0B are overlaid on the same plots. The slopes are determined by natural beam motion.

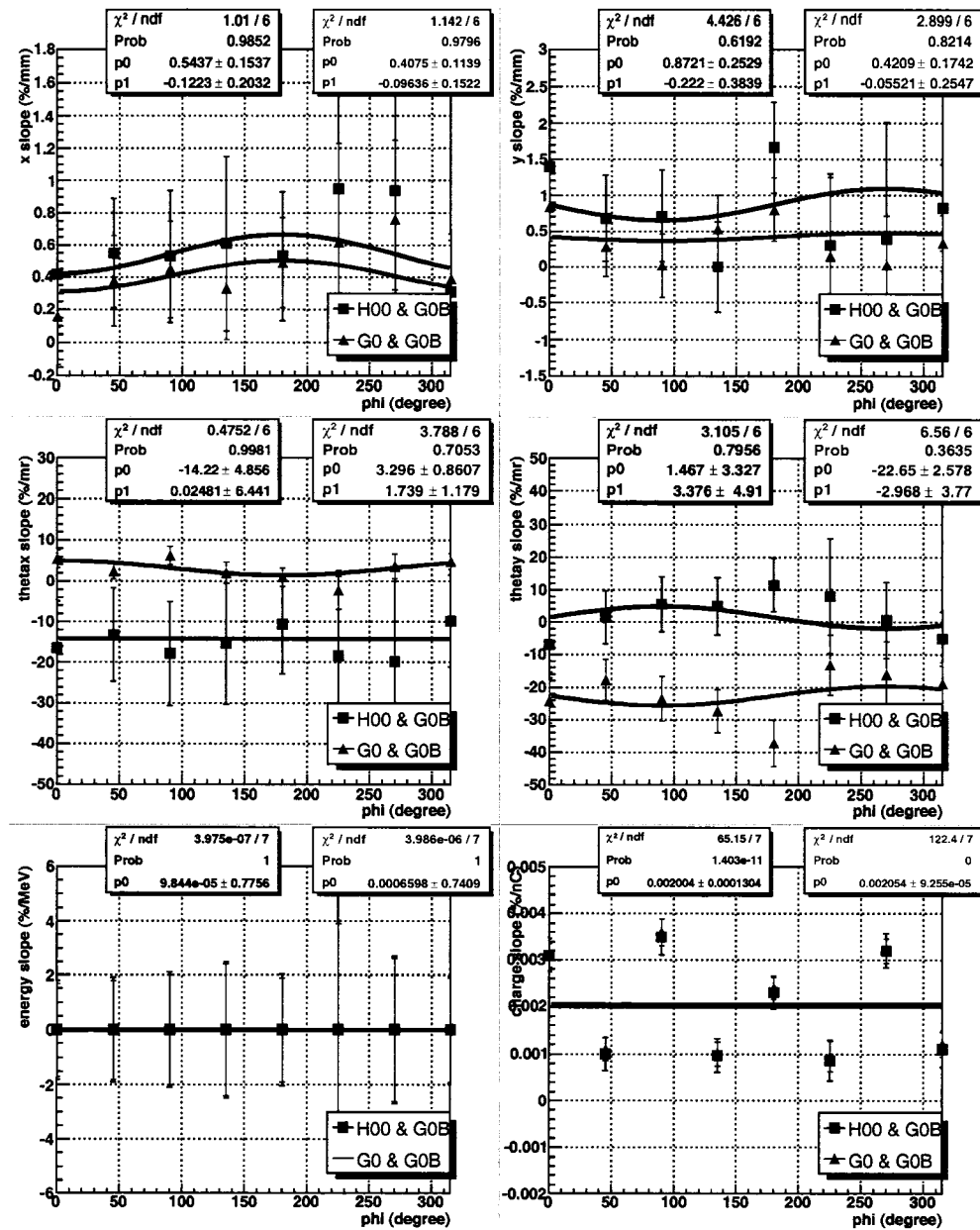


FIG. 4.13:

Average slope determined using natural beam motion versus octant for BPMs H00 and G0B (blue) and BPMs G0 and G0B (pink). The  $x$  and  $\theta_x$  slopes are fitted according to a cosine function and the  $y$  and  $\theta_y$  slopes are fitted according to a sine function. In both cases, the phase is fixed at zero. The parameter  $p_0$  is the offset and  $p_1$  is the amplitude. The  $E$  and  $Q$  slopes are fitted to a constant. The parameter  $p_0$  is the constant. The  $|\chi^2|$   $\chi^2$  probability, and parameters are displayed in a statistics box at the top of each plot. The slopes correspond to the elastic electron locus.

An obvious observation is that the angle slopes change sign with a different choice of upstream BPM. Since there are no magnetic elements between BPMs H00 and G0B, the electron beam must travel in a straight line. Therefore, it is physically impossible that the angles calculated by different sets of BPMs are different. This suggests that either BPM H00 or G0 is backwards relative to the other. To identify which BPM is backwards, the  $x$  position of multiple BPMs were subtracted from the  $x$  position of BPM G0B mps by mps. (see Figure 4.14). According to this Figure, the polarity of the last plot  $x_{G0B} - x_{G0}$  is opposite to the others. This is true for  $y$  values as well. Therefore, BPM G0 is backwards relative to the others. This has the effect of flipping the  $\theta_x$  and  $\theta_y$  slopes on the horizontal axis in Figure 4.13. Therefore, the average  $\theta_x$  and  $\theta_y$  slopes calculated by BPMs G0 and G0B are actually negative and positive, respectively.

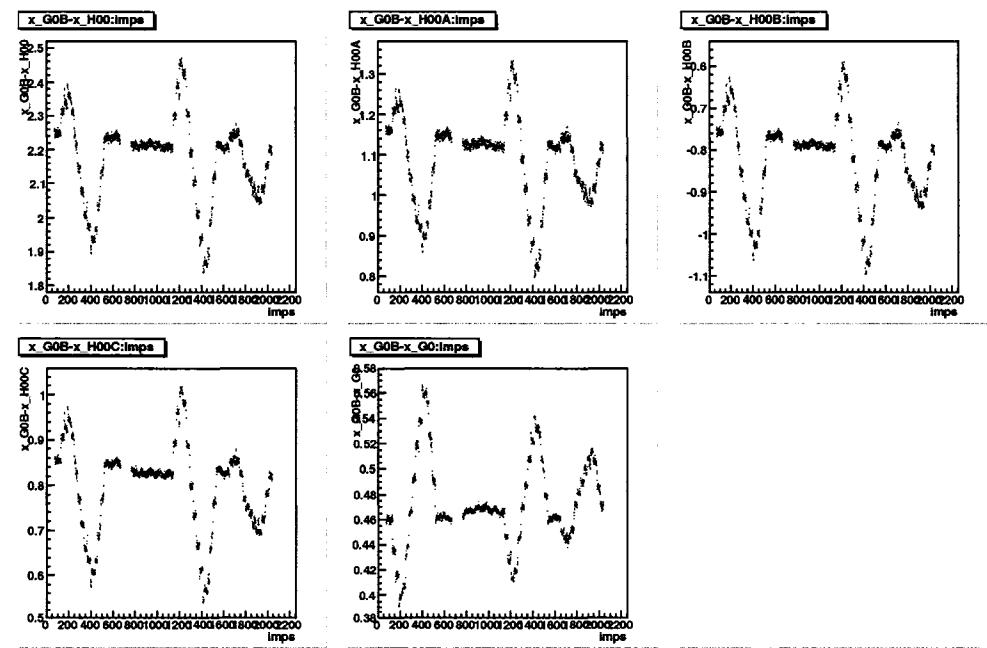


FIG. 4.14:

*The  $x$  position of multiple BPMs subtracted from the  $x$  position of BPM G0B mps by mps.*



Parameter	Value	Uncertainty	Slope	Value	Uncertainty
$\Delta x$ (nm)	18.2	6.0	$\frac{1}{Y} \frac{\partial Y}{\partial x}$ (%/mm)	0.61	0.1
$\Delta y$ (nm)	21.6	5.0	$\frac{1}{Y} \frac{\partial Y}{\partial y}$ (%/mm)	0.97	0.2
$\Delta E$ (eV)	4.3	1.1	$\frac{1}{Y} \frac{\partial Y}{\partial E}$ (%/MeV)	0.0	0.8
$\Delta \theta_x$ (mrad)	-0.88	0.18	$\frac{1}{Y} \frac{\partial Y}{\partial \theta_x}$ (%/mrad)	-14	5
$\Delta \theta_y$ (mrad)	-1.85	0.39	$\frac{1}{Y} \frac{\partial Y}{\partial \theta_y}$ (%/mrad)	2	3
$\Delta A_Q$ (ppm)	-0.03	0.26	$\frac{1}{Y} \frac{\partial Y}{\partial Q}$ (%/nC)	0.0020	0.0001

TABLE 4.4: *Left table: helicity-correlated differences/asymmetries of individual parameters (calculated quartet by quartet and averaged over the entire run) determined by BPMs H00 and G0B. Right table: average slope for all 8 octants determined using natural beam motion and based on BPMs H00 and G0B.*

Parameter	$A_{false}$ (ppm)	Uncertainty (ppm)
$x$	0.06	0.02
$y$	0.10	0.04
$E$	0.00	0.02
$\theta_x$	0.06	0.02
$\theta_y$	-0.02	0.03
$Q$	-0.001	0.01
Total	0.20	0.06

TABLE 4.5: *Overall false asymmetry and false asymmetries of individual beam parameters determined using natural beam motion and BPMs H00 and G0B.*

The helicity-correlated differences/asymmetries of individual parameters (calculated quartet by quartet and averaged over the entire run) and slopes determined using natural beam motion (averaged over all 8 octants) and BPMs H00 and G0B are listed in Table 4.4. The overall helicity-correlated false asymmetry and helicity-correlated false asymmetries of individual beam parameters are listed in Table 4.5. The overall false asymmetry is

$$A_{false} = 0.20 \pm 0.06 \text{ ppm.} \quad (4.61)$$

The helicity-correlated differences/asymmetries of individual parameters (calculated quartet by quartet and averaged over the entire run) and slopes determined using natural beam motion (averaged over all 8 octants) and BPMs G0 and G0B

Parameter	Value	Uncertainty	Slope	Value	Uncertainty
$\Delta x$ (nm)	22.4	5.6	$\frac{1}{Y} \frac{\partial Y}{\partial x}$ (%/mm)	0.40	0.11
$\Delta y$ (nm)	46.7	9.1	$\frac{1}{Y} \frac{\partial Y}{\partial y}$ (%/mm)	0.41	0.17
$\Delta E$ (eV)	4.3	1.1	$\frac{1}{Y} \frac{\partial Y}{\partial E}$ (%/MeV)	0.00	0.74
$\Delta \theta_x$ (nrad)	0.05	0.5	$\frac{1}{Y} \frac{\partial Y}{\partial \theta_x}$ (%/mrad)	-3.6	0.83
$\Delta \theta_y$ (nrad)	1.16	0.5	$\frac{1}{Y} \frac{\partial Y}{\partial \theta_y}$ (%/mrad)	23.0	2.5
$\Delta A_Q$ (ppm)	-0.03	0.3	$\frac{1}{Y} \frac{\partial Y}{\partial Q}$ (%/nC)	0.0020	9.3E-5

TABLE 4.6: *Left table: helicity-correlated differences/asymmetries of individual parameters (calculated quartet by quartet and averaged over the entire run). Right table: average slope determined using natural beam motion and based on BPMs G0 and G0B for all octants.*

Parameter	$A_{false}$ (ppm)	Uncertainty (ppm)
$x$	0.04	0.03
$y$	0.10	0.04
$E$	0.00	0.02
$\theta_x$	-0.001	0.008
$\theta_y$	0.130	0.008
$Q$	-0.001	0.01
Total	0.27	0.08

TABLE 4.7: *Overall helicity-correlated false asymmetry and false asymmetries of individual beam parameters determined using natural beam motion and based on BPMs G0 and G0B.*

are listed in Table 4.6. The overall helicity-correlated false asymmetry and helicity-correlated false asymmetries of individual beam parameters are listed in Table 4.7. The overall false asymmetry is

$$A_{false} = 0.27 \pm 0.08 \text{ ppm.} \quad (4.62)$$

The overall false asymmetry and associated error calculated by BPMs G0 and G0B is comparable to the overall false asymmetry and associated error calculated by BPMs H00 and G0B. Given the consistency, from here on we just use BPMs H00 and G0B.

### 4.7.6 A Comparison of Natural Beam Motion and Coil Modulation

During this running period, coil modulation was enabled for only 10 of the 90 production runs. These runs were the last ten runs of the running period (29014-29024). To make a direct comparison of the two running modes, the slopes of the six beam parameters determined using coil modulation and normal beam motion were plotted versus run number and overlaid on the same plots for all octants. The  $x$  slopes are shown in Figure 4.15. According to the figure, all of the slopes determined by coil pulsing are self-consistent ( $\chi^2/ndf$  is reasonable). Similar results hold for the other beam parameters. Therefore, the coil pulsing slopes are stable run-to-run. In contrast, the slopes determined by natural beam motion are not stable run-to-run. Recall Figure 4.6 where this is seen more dramatically over the whole run period.

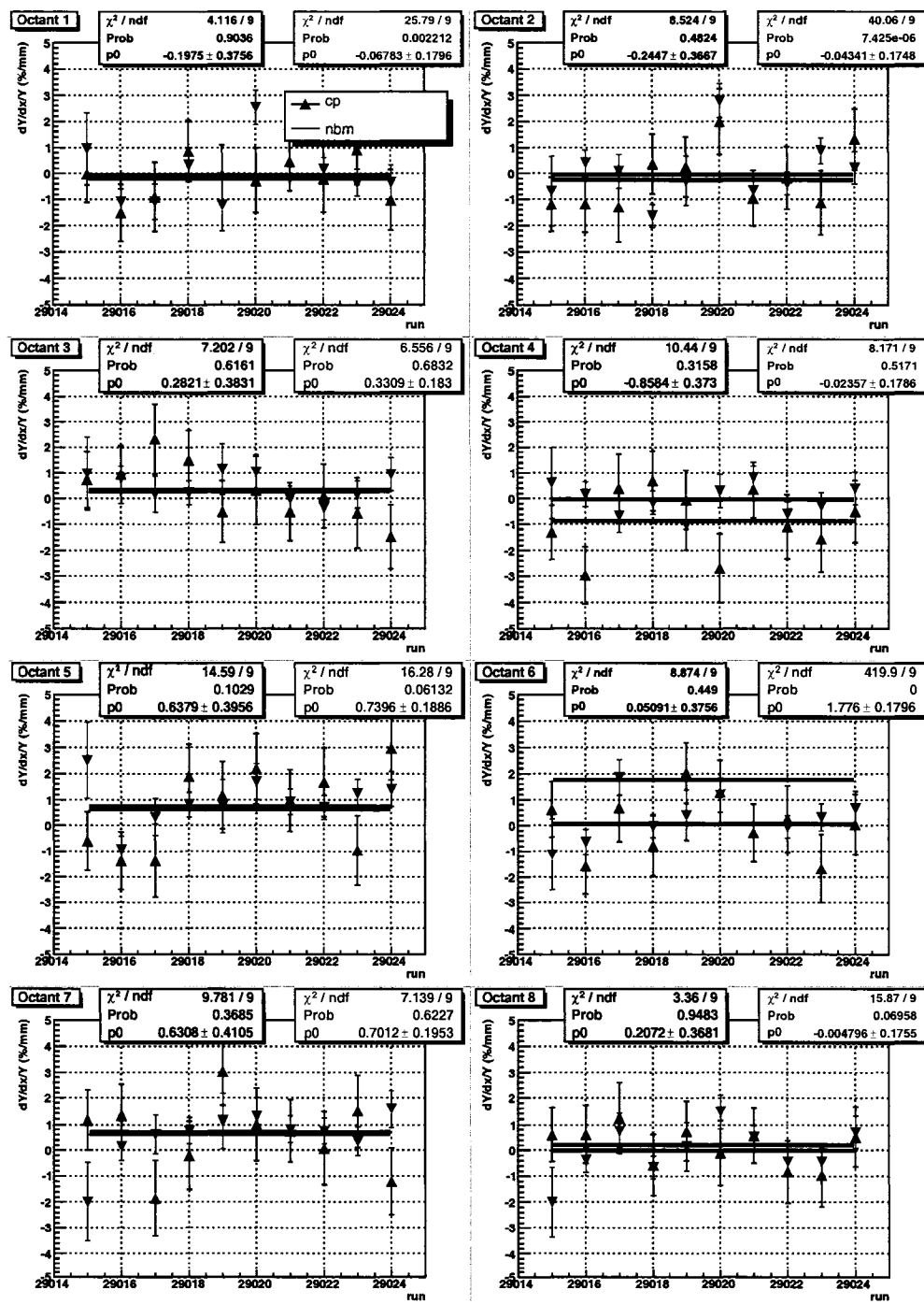


FIG. 4.15:

The  $x$  slope versus run number for normal beam motion (pink) and coil pulsing (blue). The slopes are fitted to a constant and the fit parameters are displayed in a statistics box at the top of each plot. The parameter  $p0$  is the mean.

A study to examine the instability of the slopes determined by natural beam motion revealed that the beam trip cut is sometimes ineffectual and consequently permits non-physical yields. Figure 4.16 is a plot of the elastic electron yield in octant 1 versus mps for a given run. It shows unphysical yields at about 25,000 and 68,000 mps where the beam trips. The deviation of the measured yield from the mean of the parent distribution at the location of a beam trip cut is unusually large. As a result, the calculated slope is large and unphysical. The coil pulsing results were not affected by the beam trip cut as there were no beam trips during coil modulation. Since the coils are pulsed for only the first three minutes of a run, the probability of a beam trip during this time is small.

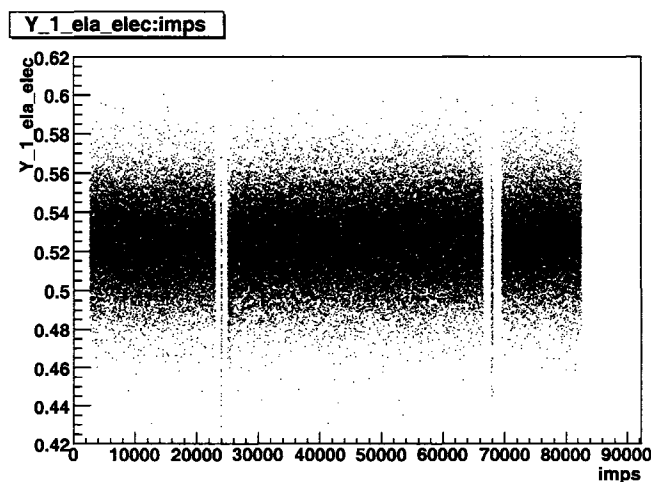


FIG. 4.16:

*Yield for a typical octant versus mps showing the sometimes ineffectual beam trip cut.*

To compare the geometrical sensitivity of individual octants to the beam positions and angles between natural beam motion and coil pulsing, the average slopes of the spatial beam parameters of the last ten runs were plotted against the average  $\Phi$  of each octant (see Figure 4.17). As seen in the Figure 4.17, the offsets of the  $x$  and  $\theta_x$  fits corresponding to coil modulation are consistent with zero while the

offsets of the  $x$  and  $\theta_x$  fits corresponding to natural beam motion are not. There is no significant improvement in the  $y$  and  $\theta_y$  slopes. This is consistent with the fact that the  $x$  range for coil modulation is two times larger than for natural beam motion and the  $y$  range for coil modulation is three times smaller than for natural beam motion (see Table 2.2).

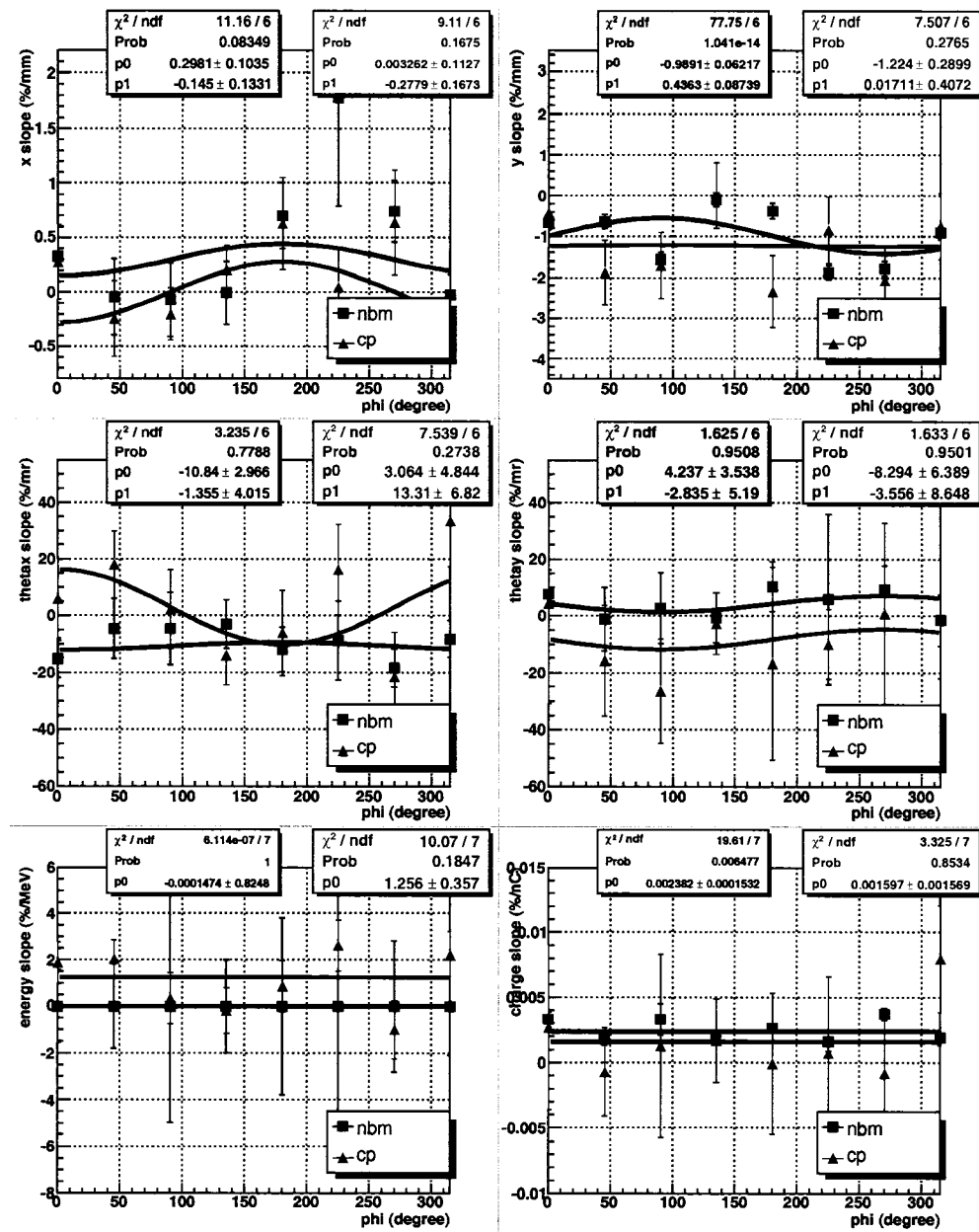


FIG. 4.17:

Average slope of the last ten runs versus average  $\Phi$  of each octant for both natural beam motion (blue) and coil pulsing (pink). The  $x$  and  $\theta_x$  slopes are fitted according to a cosine function and the  $y$  and  $\theta_y$  slopes are fitted according to a sine function. In both cases, the phase is fixed at zero. The parameter  $p_0$  is the offset and  $p_1$  is the amplitude. The  $E$  and  $Q$  slopes are fitted to a constant,  $p_0$ . The  $\chi^2$  probability, and parameters are displayed in a statistics box at the top of each plot. The slopes correspond to the elastic electron locus.

It is also interesting to fit the slopes of the spatial parameters to sine curves with the phase being a free parameter. In Figure 4.18, the average slopes of the spatial beam parameters plotted against the average  $\Phi$  of each octant. One would expect the  $x$  and  $\theta_x$  fits to have a phase of  $\pi/2$  and the  $y$  and  $\theta_y$  fits to have a phase of zero. According to the plot, the phases of the  $x$  and  $\theta_x$  fits corresponding to coil modulation are consistent with  $\pi/2$  while the phases of the  $x$  and  $\theta_x$  fits corresponding to natural beam motion are not. Similarly, the offsets of the  $x$  and  $\theta_x$  fits corresponding to coil modulation are consistent with zero while the offsets of the  $x$  and  $\theta_x$  fits corresponding to natural beam motion are not. Based on these observations, one can conclude that the slopes determined by coil modulation are well-behaved.



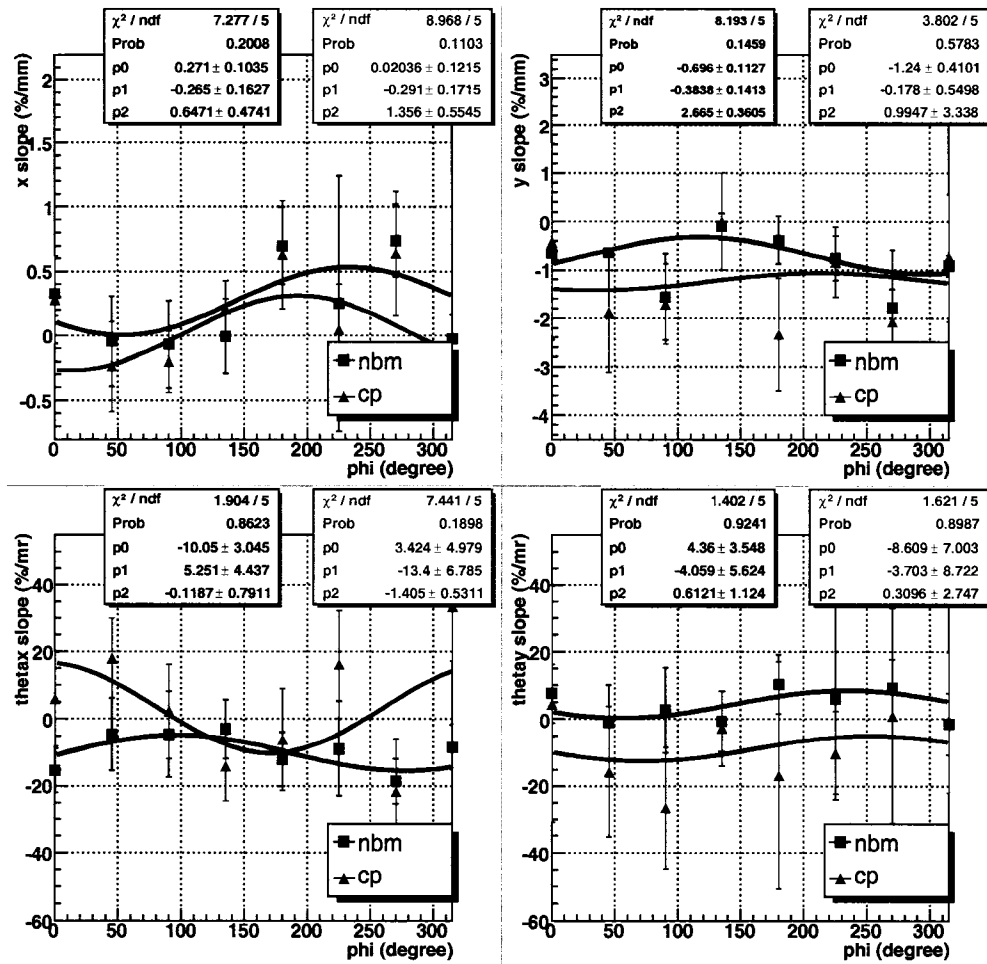


FIG. 4.18:

Average slope versus average  $\Phi$  of each octant for both natural beam motion (blue) and coil pulsing (pink). The spatial parameters are fitted according to a sine function, where the phase is a free parameter. The  $\chi^2$ ,  $\chi^2$  probability, and parameters of each fit are displayed in a statistics box at the top of each plot. The parameter  $p_0$  is the offset,  $p_1$  is the amplitude, and  $p_2$  is the phase.

Slope	Value	Uncertainty
$\frac{1}{\bar{Y}} \frac{\partial Y}{\partial x}$ (%/mm)	0.02	0.12
$\frac{1}{\bar{Y}} \frac{\partial Y}{\partial y}$ (%/mm)	-1.21	0.38
$\frac{1}{\bar{Y}} \frac{\partial Y}{\partial E}$ (%/MeV)	1.26	0.36
$\frac{1}{\bar{Y}} \frac{\partial Y}{\partial \theta_x}$ (%/mrad)	3.0	4.8
$\frac{1}{\bar{Y}} \frac{\partial Y}{\partial \theta_y}$ (%/mrad)	-8.8	6.3
$\frac{1}{\bar{Y}} \frac{\partial Y}{\partial Q}$ (%/nC)	0.002	0.002

TABLE 4.8:

*Average slope determined using coil modulation for all octants.*

The slopes determined using coil modulation (averaged over all 8 octants) are listed in Table 4.8. The helicity-correlated differences/asymmetries of individual parameters (calculated quartet by quartet and averaged over the entire run) are listed in Table 4.4. The overall helicity-correlated false asymmetry and helicity-correlated false asymmetries of individual beam parameters are listed in Table 4.9. The overall false asymmetry is

$$A_{false} = -0.03 \pm 0.08 \text{ ppm.} \quad (4.63)$$

The overall false asymmetry calculated by coil modulation is consistent with zero and smaller than the overall false asymmetry calculated by natural beam motion. The errors are comparable.

#### 4.7.7 Simulation of the Slopes

A simulation of the position slopes versus octant at 687 MeV was performed by E. Beise [79]. The yields used in the simulation are for all events in the CED-FPD matrix produced from elastic scattering. In Figures 4.19 and 4.20, the simulated average  $x$  and  $y$  slopes are plotted against octant number, respectively. The slopes are fitted according to sine functions, where the phase is a free parameter. The  $x$  slope should vary like sine with octant number and the  $y$  slope should vary like

Parameter	$A_{false}$ (ppm)	Uncertainty (ppm)
$x$	0.002	0.01
$y$	-0.13	0.05
$E$	0.03	0.01
$\theta_x$	-0.01	0.02
$\theta_y$	0.08	0.06
$Q$	-0.001	0.01
Total	-0.03	0.08

TABLE 4.9:

*Overall false asymmetry and false asymmetries of individual beam parameters as determined using coil modulation.*

	Simulation	Coil Modulation Data
$x$	$0.10 \pm 0.01$	$0.29 \pm 0.17$
$y$	$0.07 \pm 0.001$	$0.18 \pm 0.50$

TABLE 4.10:

*A comparison of the geometry amplitudes between simulation and the measured slopes from coil modulation. Amplitudes are given in %/mm.*

cosine with octant number. A comparison of the geometry amplitudes between the simulation and the actual slopes is made in Table 4.10. According to the Table, the amplitudes of the actual slopes are consistent with the amplitudes of the simulation.

### **A Comparison to the Forward Angle Experiment**

It is also interesting to draw a comparison to the forward angle experiment. A comparison of the average slopes (over all octants) is made in Table 4.11. As seen in the Table, the errors on the backward angle data are between 2 and 15 times larger than the errors on the forward angle data. Hence, it is difficult to draw any real conclusions about the degree of cancellation due to symmetry.

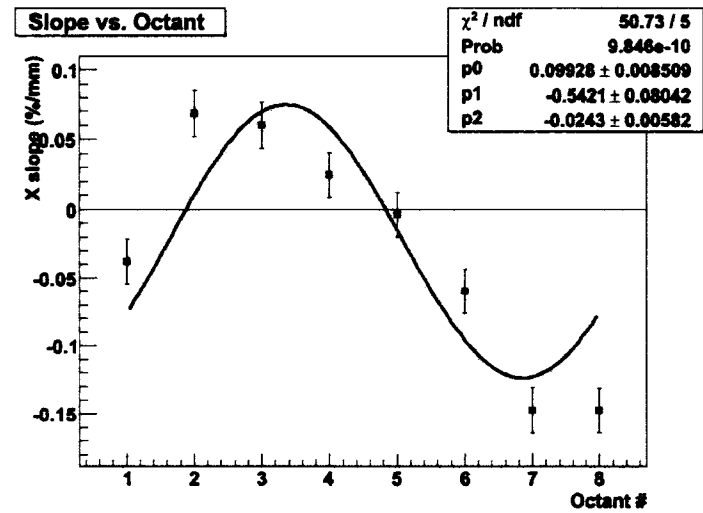


FIG. 4.19:

*Simulated average x slope versus octant number at 687 MeV. The slopes are fitted according to a sine function and the phase is a free parameter [79]. The  $\chi^2$ ,  $\chi^2$  probability, and parameters of the fit are displayed in a statistics box at the top of the plot. The parameter  $p_2$  is the offset,  $p_0$  is the amplitude, and  $p_1$  is the phase.*

#### 4.7.8 Conclusion on Beam Correction Method

Based upon these studies, I recommend linear regression according to coil modulation, at least until the beam trip cut is better understood and improved. With a perfect beam trip cut, the two approaches should agree with each other. For this thesis, we compute the false asymmetry due to helicity-correlations according to coil modulation. In addition, I recommend dedicated studies to determine the source of the small range of motion in  $y$  during coil modulation. Extending this range will improve the linear regression results in  $y$ . Sometime during the summer months, the frequency of coil modulation was changed from once every run to once every three runs to gain more production time. I recommend reversing this change.

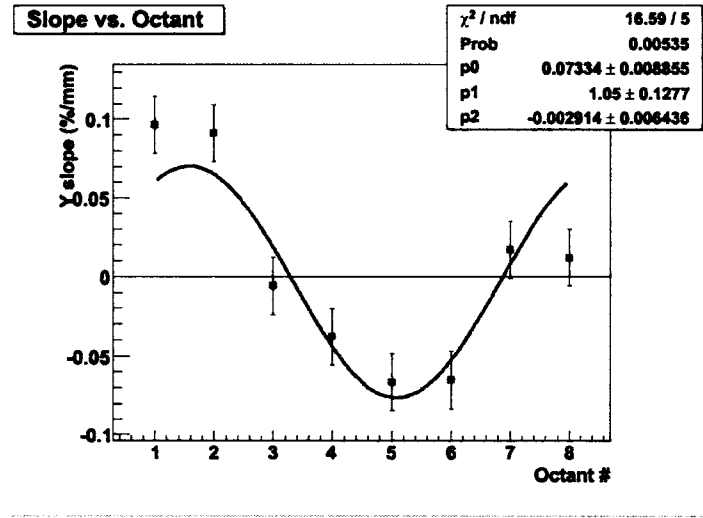


FIG. 4.20:

Simulated average  $y$  slope versus octant number at 687 MeV. The slopes are fitted according to a cosine function and the phase is a free parameter [79]. The  $\chi^2$ ,  $\chi^2$  probability, and parameters of the fit are displayed in a statistics box at the top of the plot. The parameter  $p_2$  is the offset,  $p_0$  is the amplitude, and  $p_1$  is the phase.

## 4.8 Background

The measured asymmetry  $A_{meas}$  of the elastic electron locus in the CED-FPD matrix space, after deadtime and linear regression corrections, is a weighted average of the elastic  $A_{elas}$  and background  $A_{back}$  asymmetries

$$\begin{aligned}
 A_{meas} &= \frac{Y_{elas}A_{elas} + Y_{back}A_{back}}{Y_{elas} + Y_{back}} \\
 &= \frac{Y_{elas}A_{elas} + Y_{back}A_{back}}{Y_{meas}} \\
 &= \frac{Y_{elas}}{Y_{meas}}A_{elas} + \frac{Y_{back}}{Y_{meas}}A_{back} \\
 &= \frac{Y_{meas} - Y_{back}}{Y_{meas}}A_{elas} + dA_{back} \\
 &= (1 - d)A_{elas} + dA_{back}, \tag{4.64}
 \end{aligned}$$

	Forward	Backward (Coil Modulation)
$x$ (%/mm)	$0.12 \pm 0.05$	$0.03 \pm 0.10$
$y$ (%/mm)	$-0.02 \pm 0.04$	$-1.2 \pm 0.4$
$\theta_x$ (%/mr)	$-1.6 \pm 0.9$	$2.9 \pm 4.8$
$\theta_y$ (%/mr)	$0.08 \pm 0.4$	$-8.8 \pm 6.3$

TABLE 4.11:

*A comparison of the slopes averaged over the 8 octants between the forward and backward angle experiments.*

where  $d = \frac{Y_{back}}{Y_{meas}}$  is the elastic dilution factor defined in Section 4.5. A simple rearrangement of Equation 4.64 yields the elastic asymmetry

$$A_{elas} = \frac{1}{1-d} (A_{meas} - dA_{back}). \quad (4.65)$$

In order to extract the elastic asymmetry in the elastic locus, it is necessary to determine the background asymmetry in the elastic locus. Ideally, the background asymmetry would be evaluated by looking at the cell-to-cell variation across the matrix. For each CED, the measured asymmetry would be plotted as a function of FPD. A fit would then be made to the measured asymmetry according to Equation 4.64, where the elastic asymmetry in the elastic locus is assumed to be constant as a function of FPD (or time) while the background asymmetry in the elastic locus is a polynomial (or other appropriate smooth) function in FPD. From the parameters of the fit, both the background and elastic asymmetries could be constructed.

Due to the limited statistics of this thesis, a CED by CED background fit was not possible. A cruder approach was adopted instead, as described below. The technique initially assumes that the measured asymmetry of the elastic locus is the true elastic asymmetry  $A_{elas}$ . For each cell immediately surrounding the elastic locus (cells that are neither part of the elastic locus nor the inelastic locus), the corrected background cell asymmetry  $A_{back}$  is calculated according to Equation 4.65. The corrected background asymmetries are fitted according to a constant and

the goodness of fit is evaluated according to the reduced chi-square  $\chi^2/ndf$ . The quantity  $ndf$  is the number of data points (or asymmetries) minus the number of adjustable parameters of the curve (in this case one). The reduced chi-square should be near one for a good fit. If the reduced chi-square is reasonable, then the average background asymmetry from the fit is the new corrected background asymmetry and it is used in Equation 4.65 to determine the new elastic asymmetry in the elastic locus. In principle, the new elastic asymmetry should be used to determine a new background asymmetry in an iterative process. For this data set, a few iterations showed that the background asymmetry had adequately converged at the first computation. The background asymmetry (averaged over all background cells in all octants) is

$$A_{back} = (36 \pm 35) \text{ ppm.} \quad (4.66)$$

The corresponding  $\chi^2/ndf$  is 117.9/119.

## 4.9 Beam Polarization

The polarization of the electron beam is described by a vector  $\vec{P}$ . The orientation of the vector determines the polarization direction of the beam and the magnitude of the vector determines the degree of polarization of the beam. If  $|\vec{P}| = 1$ , then the beam is 100% polarized. Conversely, if  $|\vec{P}| = 0$ , then the beam is 100% unpolarized. For values between 0 and 1, the beam is partially polarized. If the vector is parallel to the direction of motion of the electrons, then the beam is called a longitudinally polarized beam. If the vector is perpendicular to the direction of motion of the electrons, then the beam is called a transversely polarized beam. In general, the beam polarization has both a longitudinal and transverse component.

The final correction to the raw asymmetry is the correction for the incomplete

polarization of the electron beam delivered to the hall. This correction is performed last as the incomplete polarization is a simple dilution effect that affects every measured quantity in the experiment equally. The correction is simply

$$A_{corr} = \frac{A_{meas}}{P_b}, \quad (4.67)$$

where  $P_b$  is the longitudinal beam polarization or the fraction of the beam that is spin polarized. The error on the polarization fraction of the beam must be propagated to the final asymmetry.

The longitudinal polarization of the electron beam was measured with both the Moller Polarimeter in Hall C and the Mott polarimeter in the injector. The principles of the Moller and Mott measurements are described in Sections 2.6.5 and 2.6.5, respectively. The beam polarization was measured three times and the results are summarized in Table 4.12. The quoted error on the Moller measurements are statistical only. The systematic uncertainty is unknown at this time and will depend largely on the optics, which had to be adjusted to operate the Moller polarimeter at this low energy. According to the Hall C Moller expert, a conservative systematic uncertainty would be 3% [80]. Therefore, this thesis takes the systematic uncertainty to be 3%. According to Table 4.12, there is a discrepancy in the polarizations measured by the two polarimeters. The Mott polarimeter consistently measures a smaller longitudinal polarization. As the Moller is located in the experimental hall and is more directly relevant, this thesis takes the polarization to be the average of the Moller measurements

$$P_b = (-86.03 \pm 0.22 \pm 3)\%. \quad (4.68)$$

According to Section 2.6.5, the Moller asymmetry is negative. Consequently, the spin of the electron beam points upstream (+ helicity). As seen in Table 4.12, the beam polarization is positive when the IHWP is OUT. Therefore, the raw exper-



Date	IHWP	Moller (%)	Mott (%)
04-10-2006	IN	$-86.36 \pm 0.36$	$-81.85 \pm 1.25 \pm -0.98$
04-13-2006	IN	$-85.09 \pm 0.42$	$-82.20 \pm 0.97 \pm -0.99$
04-24-2006	OUT	$86.65 \pm 0.36$	

TABLE 4.12:

*Moller and Mott measurements of beam polarization in April, 2006. Error on Moller values are statistical only. Errors on Mott values are statistical and systematic.*

imental asymmetry is positive when the IHWP is out and negative when the IHWP is IN.

# CHAPTER 5

## Results

### 5.1 Introduction

This chapter presents the results of the analysis for data taken during the first part of the 687 MeV run, beginning in March 2006 and ending in May 2006. During this period, a total of 15 C of beam charge was accumulated on the liquid hydrogen target, of which 7 C was taken with the IHWP in and 8 C was taken with the IHWP out (see Figure 5.1). The total accumulated charge on the target represents about 15% of the 110 C which was proposed for this beam energy.

A summary of the parity quality beam is provided in Section 5.2 followed by a discussion of the raw detector asymmetries in Section 5.3. Section 5.4 presents the physics asymmetry and Section 5.5 relates the physics asymmetry to the strange form factors.

### 5.2 Parity Quality Beam

During the Pockels Cell installation in March 2006, we achieved 3.2% linear polarization and 99.9% circular polarization at the Pockels cell. We aligned the

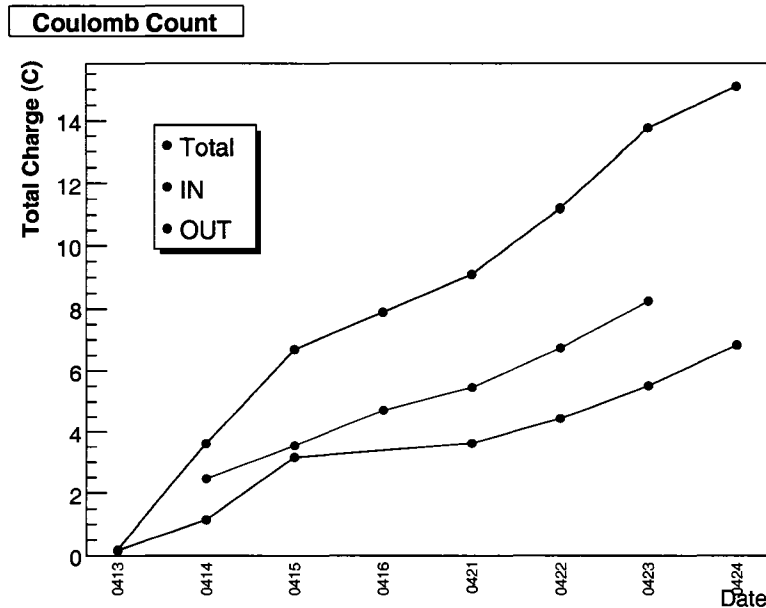


FIG. 5.1: *Accumulated charge on target versus date.*

IA cell with a  $\lambda/4$  waveplate at  $14^\circ$  and measured its slope (linear dependence of charge asymmetry on voltage) to be  $-17.75$  ppm/V. Table 5.1 summarizes the position differences obtained on the QPD when steering is the dominant effect (LP out) and our goals for these measurements. To achieve position differences in the injector smaller than  $0.3 \mu\text{m}$ , we aimed for position differences on the QPD (LP out) smaller than  $0.1 \mu\text{m}$ . We aimed for position differences of this magnitude because the position differences on the QPD will be amplified about three times on the photocathode, since the photocathode is located about three times further from the PC than the QPD. We achieved position differences on the QPD less than  $0.1 \mu\text{m}$  in the  $x$  direction. However, we could not achieve position differences on the QPD less than  $0.1 \mu\text{m}$  in the  $y$  direction without compromising the position differences in the  $x$  direction.

Table 5.2 summarizes the position differences obtained on the QPD when phase

	IHWP IN ( $\mu\text{m}$ )	IHWP OUT ( $\mu\text{m}$ )	Goal ( $\mu\text{m}$ )
$\Delta x$	$0.024 \pm 0.023$	$0.10 \pm 0.014$	$< 0.1$
$\Delta y$	$0.37 \pm 0.019$	$-0.21 \pm 0.019$	$< 0.1$

TABLE 5.1:

*Position differences obtained on the QPD when steering is the dominant effect (LP out).*

	IHWP IN ( $\mu\text{m}$ )	IHWP OUT ( $\mu\text{m}$ )	Goal ( $\mu\text{m}$ )
$\Delta x$	$5.71 \pm 0.015$	$-2.96 \pm 0.015$	$< 6$
$\Delta y$	$-5.12 \pm 0.023$	$1.71 \pm 0.025$	$< 6$

TABLE 5.2:

*Position differences obtained on the QPD when phase gradients are the dominant effect (LP in).*

gradients are the dominant effect (LP in) and our goals for these measurements. To achieve position differences in the injector smaller than  $0.3 \mu\text{m}$ , we aimed for position differences on the QPD (LP in) smaller than  $6 \mu\text{m}$ . We aimed for position differences of this magnitude because the position differences on the QPD will drop about 20 times on the photocathode since the LP has an analyzing power of 100% and the photocathode has an analyzing power of 5%. We achieved position differences on the QPD less than  $6 \mu\text{m}$  in both the  $x$  and  $y$  directions.

Figure 5.2 shows the helicity-correlated differences/asymmetry of the six beam parameters versus slug number over the running period. A slug refers to a data sample with a consistent half-waveplate state (IN versus OUT). The  $\chi^2$  of each fit is reasonable. Therefore, the differences/asymmetry of the six beam parameters are stable slug-to-slug.

### 5.3 Raw Asymmetry

The average raw (blinded asymmetry) of the elastic electron locus is plotted versus slug number for each of the eight octants in Figure 5.3. The  $\chi^2$  of each fit is reasonable. Therefore, the raw asymmetries are stable slug-to-slug.

To assess possible octant dependence on the raw asymmetry, the average raw asymmetry of the elastic electron locus is plotted versus octant number in Figure 5.4a. The  $\chi^2$  of both fits (IN and OUT) is reasonable. Therefore, the raw asymmetry exhibits no octant dependence. To check for electronic asymmetries, the average raw asymmetry for each waveplate state of each octant is added together and plotted in Figure 5.4b. The line represents the average over all eight octants

$$\langle A_{raw} \rangle^{IN} + \langle A_{raw} \rangle^{OUT} = -11.0 \pm 9.6 \text{ ppm.} \quad (5.1)$$

This number is consistent with zero and thus provides no evidence for false electronic or other uncorrected false asymmetries. Figure 5.4c is the waveplate-averaged raw asymmetry (out-in)

$$\langle A_{raw} \rangle = -38.16 \pm 4.81 \text{ ppm.} \quad (5.2)$$

The  $\chi^2$  of the fit is reasonable. Hence, the wave-plate averaged raw asymmetry shows no tendency toward octant dependence.

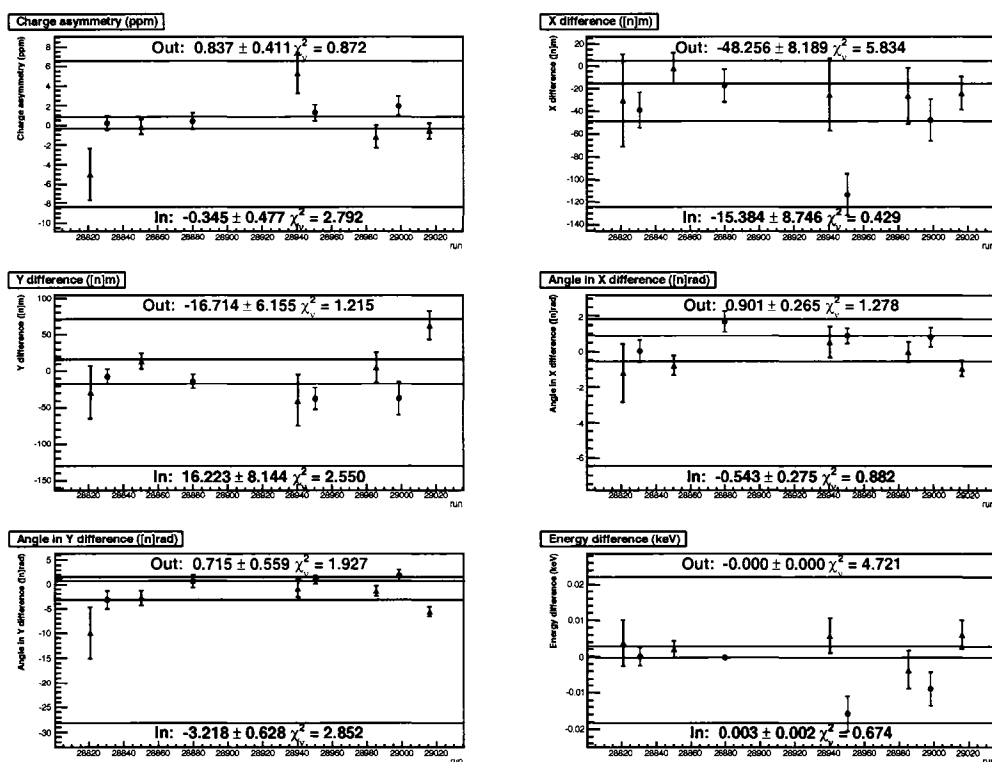


FIG. 5.2:

*The helicity-correlated differences/asymmetry of the six beam parameters versus slug number. The red line is the average of the helicity-correlated difference/asymmetry when the IHWP was OUT and the blue line is the average of the helicity-correlated difference/asymmetry when the IHWP was IN. The average difference/asymmetry and  $\chi^2$  of the fit when the IHWP was OUT is printed in red at the top of each plot. Similarly, the average difference/asymmetry and  $\chi^2$  of the fit when the IHWP was IN is printed in blue at the bottom of each plot.*

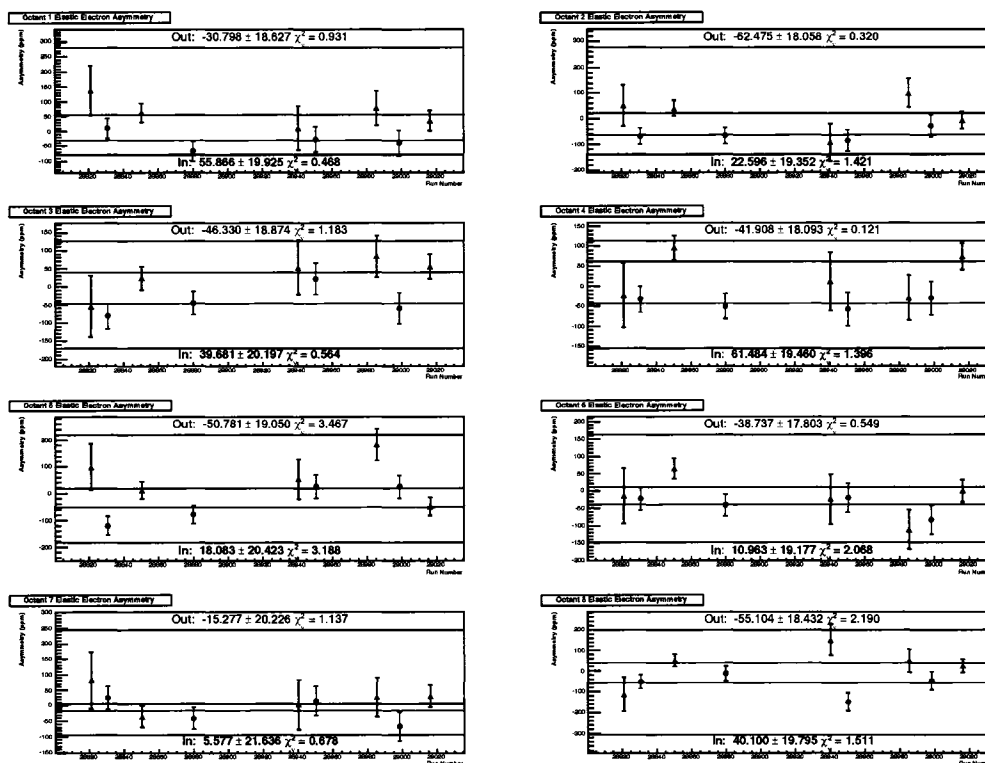


FIG. 5.3:

The average raw (blinded) asymmetry of the elastic electron locus versus slug number. The red line is the average asymmetry when the IHWP was out and the blue line is the average asymmetry when the IHWP was in. The average raw asymmetry and  $\chi^2$  for the case when the IHWP was out is printed in red at the top of each plot. Similarly, the average raw asymmetry and  $\chi^2$  for the case when the IHWP was in is printed in blue at the bottom of each plot.

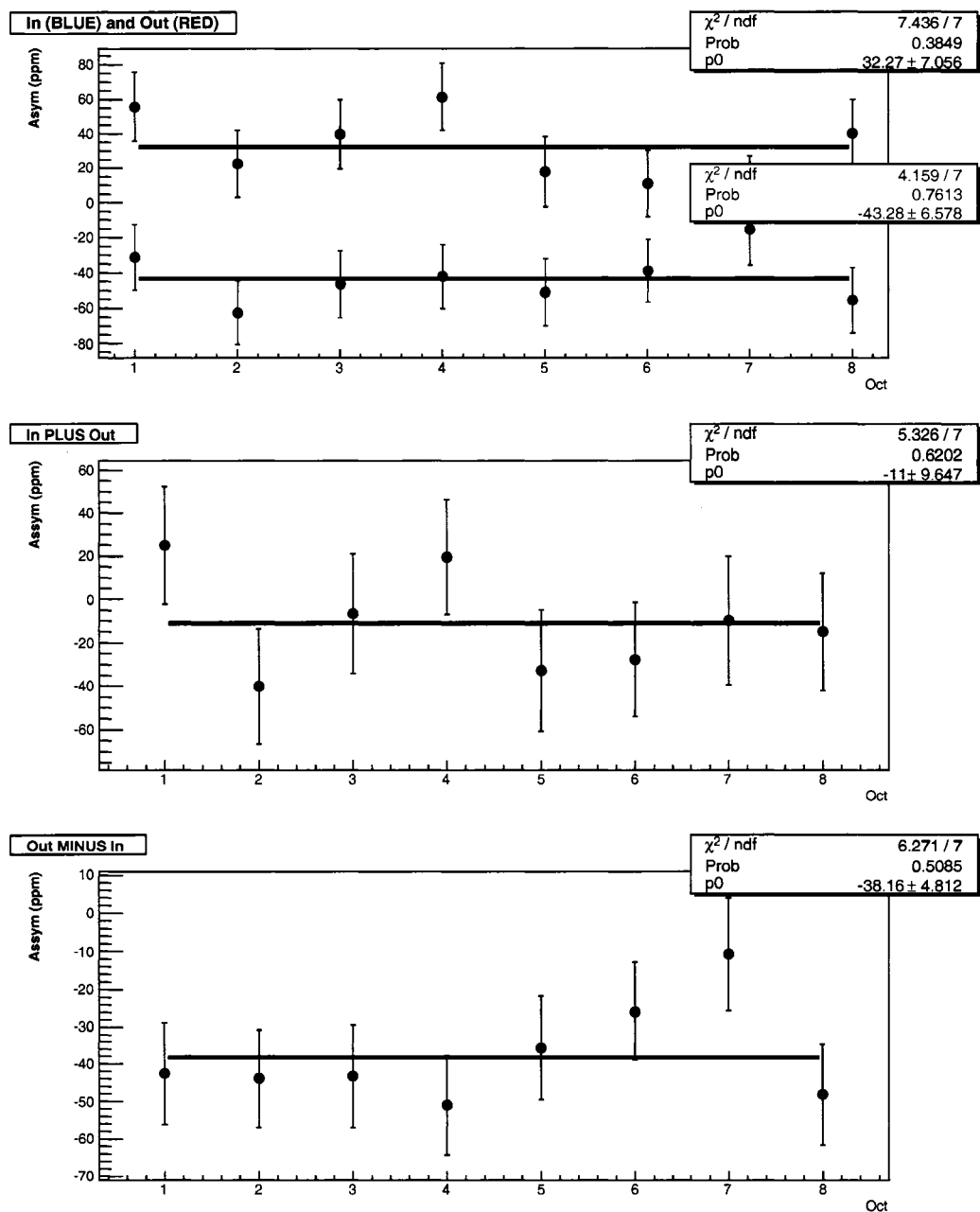


FIG. 5.4:

(a) The average raw asymmetry of the elastic electron locus versus octant number. The red line is the average asymmetry when the IHWP was out and the blue line is the average asymmetry when the IHWP was in. (b) The sum of the average raw asymmetries (in and out) versus octant number. (c) The waveplate-averaged raw asymmetry (out-in).



## 5.4 Physics Asymmetry

To preserve the true physics asymmetry until the entire 687 MeV data set has been analyzed, the blinding factor was not unmasked for this thesis. This decision was made by the  $G^0$  executive committee. In this thesis, we treat the blinding factor as an additional uncertainty on the asymmetry. As explained in Section 4.1, the blinding factor is a multiplicative factor between 0.75 and 1.25. This creates an additional 25% uncertainty on the asymmetry. The physics asymmetry (corrected for deadtime, helicity-correlated effects, background, and polarization) and taking into account the true sign of the physics asymmetry is

$$A_{phys} = (-47.4 \pm 7.1 \pm 5.9 \pm 11.8) \text{ ppm}, \quad (5.3)$$

where the first uncertainty is statistical, the second uncertainty is systematic, and the third uncertainty is associated with the blinding factor (25% of 47.4 ppm). The statistical uncertainty is the raw statistical uncertainty added in quadrature with the statistical component of the deadtime uncertainty.

The goal of the experiment is to measure the asymmetry with an overall uncertainty (statistical and systematic) of 5% of the measured asymmetry. The overall uncertainty in this thesis (excluding the uncertainty due to the blinding factor) is about 25% of the raw measured asymmetry (38.16 ppm). The data analyzed in this thesis represents 15 C of the 110 C collected at this  $Q^2$ . Therefore, the entire data set at this  $Q^2$  will contain about 7 times more statistics. Thus the final raw statistical error will be a factor of  $1/\sqrt{7} \sim 0.38$  smaller than the raw statistical error of this thesis. Given this fact, to achieve an overall uncertainty of 5% on the entire data set, the systematic uncertainty must be less than 1 ppm.

The sizes and corresponding uncertainties of the systematic corrections leading to the physics asymmetry in this thesis is provided in Table 5.3. The background correction uncertainty dominates the systematic uncertainties, followed by the po-

Source	Correction (ppm)	Uncertainty (ppm)
Deadtime	2.0	0.3
Helicity-correlated beam properties	0.03	0.08
Background	0.6	4.8
Polarization	6.6	1.4

TABLE 5.3:

*The sizes and corresponding uncertainties of the systematic corrections leading to the physics asymmetry.*

larization uncertainty. Both of these uncertainties will need to be reduced to achieve the desired precision on the entire data set. The uncertainty associated with the helicity-correlated beam properties is a negligible contribution to the 5% overall uncertainty that the experiment aims for. Therefore, the helicity-correlated beam properties and slopes are under adequate control for the final precision of the experiment.

## 5.5 Strange Form Factors

As explained in Section 1.9.2, the quantity  $G_E^{\gamma,s} + \eta G_M^{\gamma,s}$  is calculated according to

$$\begin{aligned}
A(\vec{e}p) = & - \frac{G_F Q^2}{4\pi\alpha\sqrt{2}} (1 - 4\sin^2\theta_w) (1 + R_V^p) \\
& + \frac{G_F Q^2}{4\pi\alpha\sqrt{2}} (1 + R_V^n) \frac{(\epsilon G_E^{\gamma,p} G_E^{\gamma,n} + \tau G_M^{\gamma,p} G_M^{\gamma,n})}{\epsilon (G_E^{\gamma,p})^2 + \tau (G_M^{\gamma,p})^2} \\
& + \frac{G_F Q^2}{4\pi\alpha\sqrt{2}} (1 + R_V^{(0)}) \epsilon G_E^{\gamma,p} \frac{(G_E^{\gamma,s} + \eta G_M^{\gamma,s})}{\epsilon (G_E^{\gamma,p})^2 + \tau (G_M^{\gamma,p})^2} \\
& + \frac{G_F Q^2}{4\pi\alpha\sqrt{2}} (1 - 4\sin^2\theta_w) \frac{\epsilon' G_M^{\gamma,p} G_A^{e,p}}{\epsilon (G_E^{\gamma,p})^2 + \tau (G_M^{\gamma,p})^2}, \tag{5.4}
\end{aligned}$$

where

$$\eta = \frac{\tau G_M^{\gamma,p}}{\epsilon G_E^{\gamma,p}} = 2.84. \tag{5.5}$$

In order to calculate  $G_E^{\gamma,s} + \eta G_M^{\gamma,s}$  at  $Q^2 = 0.631 \text{ (GeV/c)}^2$ , it is necessary to know the electromagnetic form factors  $G_E^{\gamma,p}$ ,  $G_M^{\gamma,p}$ ,  $G_E^{\gamma,n}$ , and  $G_M^{\gamma,n}$  and the axial form factor  $G_A^e$  at the same  $Q^2$ . The form factors at  $Q^2 = 0.631 \text{ (GeV/c)}^2$  are determined via parametrizations of the world data set. Section 5.5.1 describes the parametrizations of the electromagnetic form factors and section 5.5.2 describes the parametrization of the axial form factor.

### 5.5.1 Parametrization of the Electromagnetic Form Factors

According to Kelly [40], the parametrization of nucleon form factors takes the form

$$G(Q^2) \propto \frac{\sum_{k=0}^n a_k \tau^k}{a + \sum_{k=1}^{n+2} b_k \tau^k}, \quad (5.6)$$

where both the numerator and denominator are polynomials in  $\tau = Q^2/4m_p^2$ , and  $a_k$  and  $b_k$  are parameters. For magnetic form factors, a factor of  $\mu$  is included on the right-hand side. This parametrization provides excellent fits to  $G_E^{\gamma,p}$ ,  $G_M^{\gamma,p}/\mu_p$ , and  $G_M^{\gamma,n}/\mu_n$  with  $n = 1$  and  $a_0 = 1$ . However, this parametrization is less successful for  $G_E^{\gamma,n}$  because there is limited data. The Galaster parametrization is used to compute the electric neutron form factor

$$G_E^{\gamma,n}(Q^2) = \frac{A\tau}{1+B\tau} G_D(Q^2), \quad (5.7)$$

where  $G_D = (1 + Q^2/\Lambda^2)^{-2}$  with  $\Lambda^2 = 0.71(\text{GeV/c})^2$ .

The electromagnetic form factors at  $Q^2 = 0.631 \text{ GeV/c}^2$  are calculated to be

$$\begin{aligned} G_E^{\gamma,p} &= 0.273 \pm 0.017 \\ G_M^{\gamma,p}/\mu_p &= 0.283 \pm 0.007 \\ G_E^{\gamma,n} &= 0.054 \pm 0.005 \\ G_M^{\gamma,n}/\mu_n &= 0.289 \pm 0.064. \end{aligned} \quad (5.8)$$

### 5.5.2 Parameterization of the Axial Form Factor

According to Section 1.9.2, the radiatively corrected axial form factor  $G_A^{e,p}$  is

$$G_A^{e,p} = - (1 + R_A^{T=1}) G_A^{T=1} + \sqrt{3} R_A^{T=0} G_A^{(8)} + (1 + R_A^{(0)}) G_A^s. \quad (5.9)$$

In order to calculate  $G_A^{e,p}$ , it is necessary to know  $G_A^{T=1}$ ,  $G_A^{(8)}$ , and  $G_A^s$ . For consistency, this thesis uses the same values used in the  $G^0$  forward angle experiment [75]. The isovector  $G_A^{T=1}$  is known from charged current quasi-elastic scattering and is parametrized according to

$$G_A^{T=1}(Q^2) = \frac{G_A^{T=1}(0)}{(1 + Q^2/\Lambda^2)}, \quad (5.10)$$

where  $G_A^{T=1}(0) = 1.2695 \pm 0.0029$  [82] is measured in neutron  $\beta$  decay and  $\Lambda = 1.001 \pm 0.02$  GeV [83] is the axial mass and is known from neutrino charged current cross section data. The isoscalar  $G_A^{(8)}$  at  $Q^2 = 0$  is estimated from hyperon decay [84]

$$2\sqrt{3}G_A^{(8)}(0) = 0.585 \pm 0.025. \quad (5.11)$$

Its  $Q^2$  dependence is expected to have the same dipole form and axial mass parameter as the isovector axial form factor. The strange axial form factor  $G_A^s$  at  $Q^2 = 0$  is the strange quark contribution to the nucleon spin and is taken to be [85]

$$\Delta s = -0.084 \pm 0.040. \quad (5.12)$$

Just like the isovector and isoscalar pieces, the strange axial form factor is assumed to have the same  $Q^2$  dependence.

The radiatively corrected axial form factor at  $Q^2 = 0.631 \text{ GeV}^2/c^2$  is thus calculated to be

$$G_A^{e,p} = -0.39 \pm 0.48. \quad (5.13)$$

### 5.5.3 Results

Based on these parametrizations, a linear combination of the strange form factors is extracted from our physics asymmetry (Equation 5.3). Taking the blinding factor to be 0.75, we get

$$G_E^{\gamma,s} + 2.84G_M^{\gamma,s} = -0.92 \pm 0.55. \quad (5.14)$$

Taking the blinding factor to be 1.25, we get

$$G_E^{\gamma,s} + 2.84G_M^{\gamma,s} = 0.21 \pm 0.55. \quad (5.15)$$

The error associated with each linear combination is the statistical and systematic errors added in quadrature. The result is thus somewhere between these two bounds. In comparison, the result of the forward angle experiment, at  $Q^2 = 0.631 \text{ (GeV/c)}^2$ , is

$$G_E^s + 0.543G_M^s = 0.060 \pm 0.028, \quad (5.16)$$

where the uncertainty is the statistical and systematic errors added in quadrature. All three of these linear combinations are overlaid in a plot of  $G_E^s$  versus  $G_M^s$  in Figure 5.5.

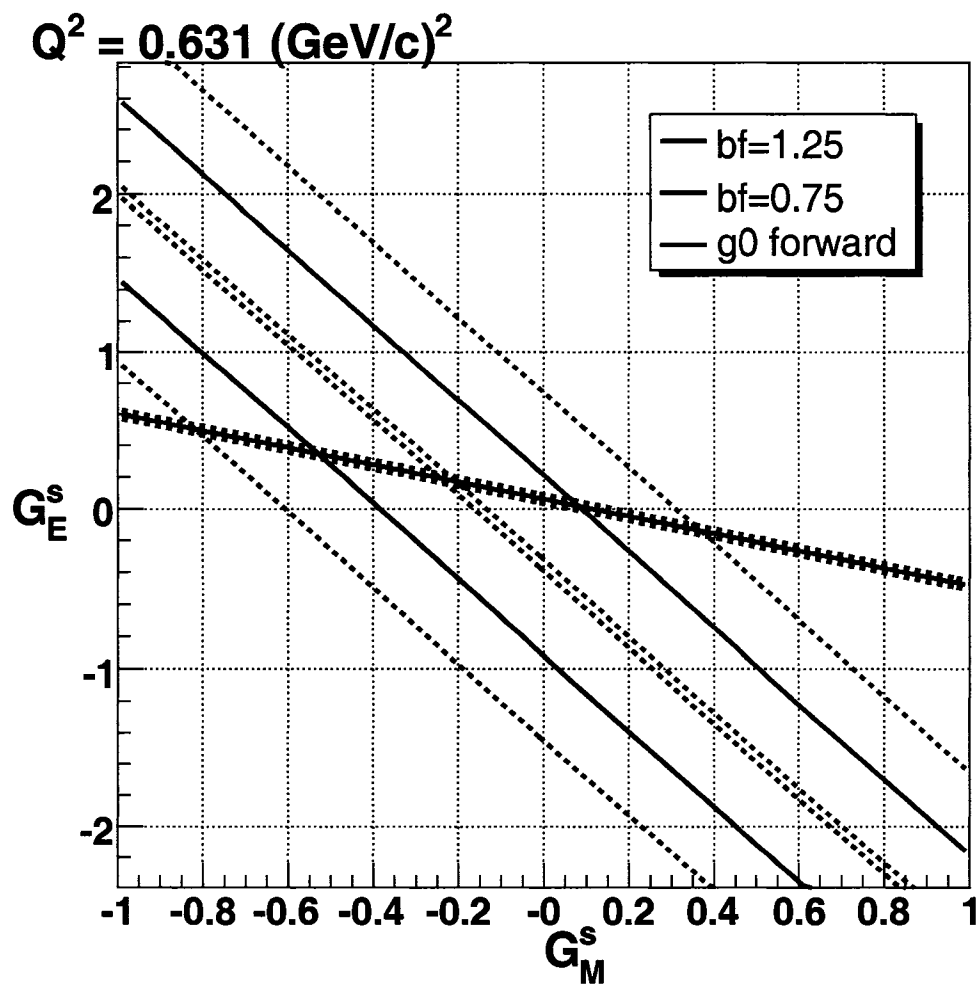


FIG. 5.5:

*A linear combination of strange form factors. The red line corresponds to a blinding factor of 1.25, the blue line corresponds to a blinding factor of 0.75, and the green line corresponds to the forward angle result. The solid lines are the central values and the dashed lines are the one sigma errors.*

According to the Figure, for the case where the blinding factor is 1.25, the strange form factor combination is consistent with zero. For the case where the blinding factor is 0.75, the strange form factor combination is two sigma away from zero. Thus, this result is consistent with the absence of strange quarks. The blinding factor prevents us from making a more precise interpretation of the strange form factors.

This thesis demonstrates that the helicity-correlated beam properties are under sufficient control for the remainder of the experiment. Parity quality was achieved to the level where the helicity-correlated false asymmetry is considered a negligible contribution to the 5% overall uncertainty that the experiment aims for in the determination of its parity violating asymmetry. As a result, the experiment can proceed successfully without a concern for this systematic.

# APPENDIX A

## Mathematical Identities

This appendix shows four simple mathematical identities that can be used to decompose a compound asymmetry [73]. The asymmetry  $A_q$  is defined to be

$$A_q = \frac{q^+ - q^-}{q^+ + q^-}, \quad (\text{A.1})$$

where  $q$  is any variable and is the average of the two helicity states  $q^+$  and  $q^-$

$$q = \frac{q^+ + q^-}{2}. \quad (\text{A.2})$$

Substituting Equation A.2 into A.1 yields

$$q^\pm = (1 \pm A_q) q \quad (\text{A.3})$$



## Addition

$$\begin{aligned}
 A(a+b) &= \frac{(a^+ + b^+) - (a^- + b^-)}{(a^+ + b^+) + (a^- + b^-)} \\
 &= \frac{(a^+ - a^-) + (b^+ - b^-)}{(a^+ + a^-) + (b^+ + b^-)} \\
 &= \frac{2aA_a + 2bA_b}{2a + 2b} \\
 &= \frac{a}{a+b}A_a + \frac{b}{a+b}A_b
 \end{aligned} \tag{A.4}$$

## Multiplication

$$\begin{aligned}
 A(ab) &= \frac{a^+b^+ - a^-b^-}{a^+b^+ + a^-b^-} \\
 &= \frac{ab(1+A_a)(1+A_b) - ab(1-A_a)(1-A_b)}{ab(1+A_a)(1+A_b) + ab(1-A_a)(1-A_b)} \\
 &= \frac{2ab(A_a + A_b)}{2ab(1 + A_aA_b)} \\
 &\simeq A_a + A_b,
 \end{aligned} \tag{A.5}$$

where we assume that  $A_aA_b \ll 1$ .

## Division

$$\begin{aligned}
 A\left(\frac{a}{b}\right) &= \frac{\frac{a^+}{b^+} - \frac{a^-}{b^-}}{\frac{a^+}{b^+} + \frac{a^-}{b^-}} \\
 &= \frac{ab(1+A_a)(a-A_b) - ab(1-A_a)(a+A_b)}{ab(1+A_a)(a-A_b) + ab(1-A_a)(a+A_b)} \\
 &= \frac{2ab(A_a - A_b)}{2ab(1 - A_aA_b)} \\
 &\simeq A_a - A_b
 \end{aligned} \tag{A.6}$$

## Scalar Multiplication

$$\begin{aligned} A(ca) &= \frac{ca^+ - ca^-}{ca^+ + ca^-} \\ &= A(a), \end{aligned} \tag{A.7}$$

where  $c$  is a scalar.

# APPENDIX B

## Construction and Assembly of CEDs

This appendix details the steps used to construct and assemble the CEDs. The construction of the CEDs began in Fall 2003 and ended in December 2004. The job required a team of one postdoctoral researcher, one graduate student, and three undergraduate students. Following their construction, the CEDs were transported to the experimental hall and mounted to the ferris wheel.

Step 1: Assemble the necessary materials. These include black tape, mylar, teflon, tedlar, the scintillator, the light guide, the PMT, its adaptor, UV lamp, goggles, glue, syringe, rubber bands, binder clips.

Step 2: Clean the PM adapter faces of any old grease or dirt. Wrap the mid-section of the PMT adapter in teflon. On top of the teflon, wrap the PMT adapter in one layer of tedlar. Affix the tedlar with black tape.

Step 3: Clean the faces of the light guide of any old grease or dirt. Apply the glue to the face of the light guide using a syringe. The glue should be applied in a single straight line along the center of the face. Using the tip of the syringe, spread

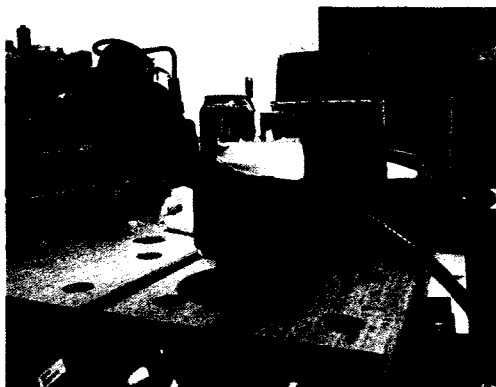


FIG. B.1: *CED Construction Step 2.*

the glue out uniformly to form a smooth, thin layer. Couple the entire surface of the light guide to the PMT adapter by means of rubber bands and binder clips. If some excess glue spills out over the edges, this is acceptable. Avoid trapping air bubbles between the light guide and PMT thus producing an inefficient optical coupling. Handling the light guide with bare hands should also be avoided. Apply UV light to the interface for about two minutes.

Step 4: Wrap the ends of the light guide loosely in mylar so as to assure a layer of air in contact with the surfaces. On top of the mylar, wrap the light guide in two layers of tedlar. Affix the mylar and tedlar with black tape. Wrap the light guide neatly in black tape along its entire length so as to ensure light tightness. Special attention should be paid to corners and sharp bends where light leaks will most likely occur.

Step 5: Test the light guide/PM adapter assembly for light tightness. Cover the assembly in black felt and apply voltage. Read the anode current. Remove the felt and read the anode current. A significant change in anode current indicates a light leak.

Step 6: Apply glue to the other face of the light guide using a syringe. Using

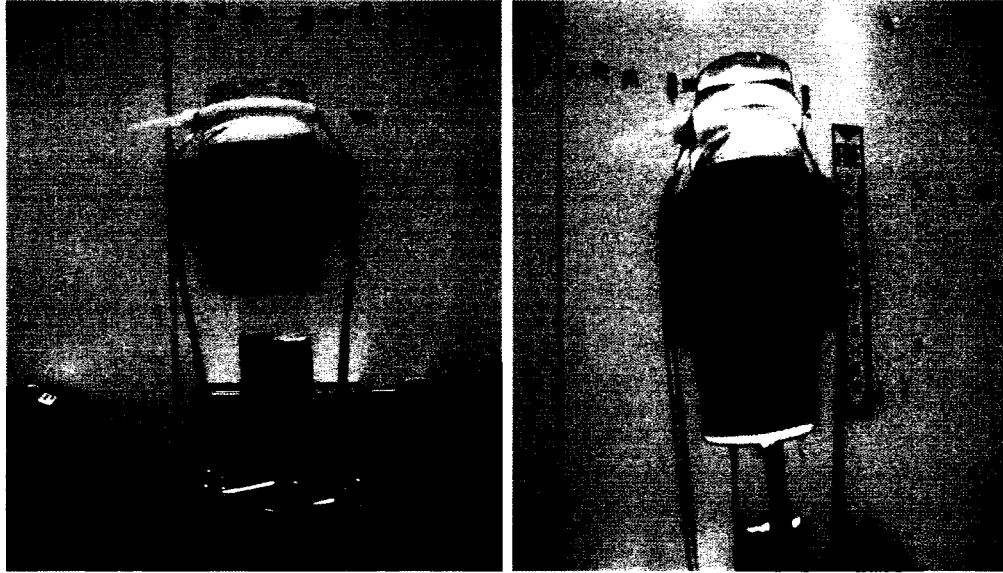


FIG. B.2: *CED Construction Step 3.*

the tip of the syringe, spread the glue out uniformly to form a smooth, thin layer. Couple the entire surface of the light guide to the scintillator by means of rubber bands and binder clips. Apply UV light to the interface for about two minutes.

Step 7: Wrap the interface of the PMT and PMT adapter loosely in mylar so as to assure a layer of air in contact with the surfaces. On top of the mylar, wrap the interface in black tape to ensure light tightness.

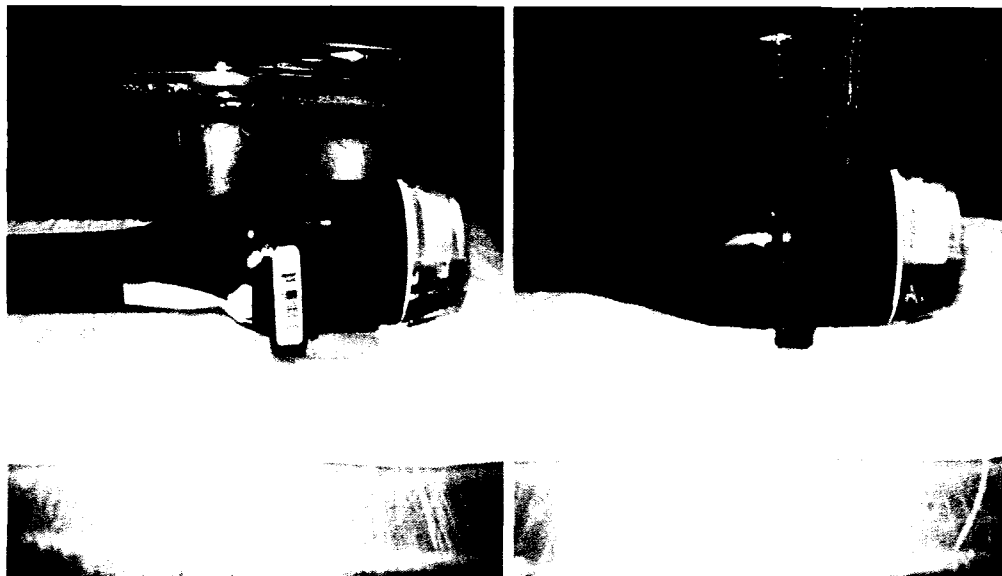


FIG. B.3: *CED Construction Step 4.*



FIG. B.4: *CED Construction Step 5.*



FIG. B.5: *CED Construction Step 6.*

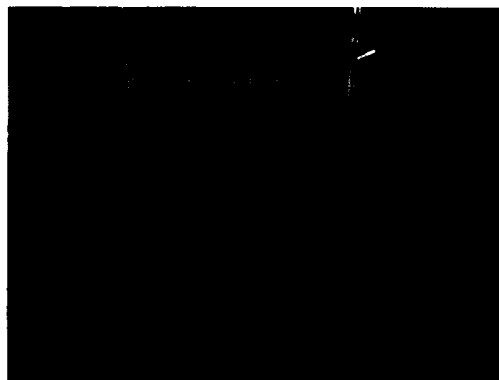


FIG. B.6: *CED Construction Step 7.*

## BIBLIOGRAPHY

- [1] M. Riordian, “Science Fashions ad Scientific Fact.” 2003.  
<http://www.aip.org/pt/vol-56/iss-8/p50.html>.
- [2] Particle Data Group, Eur. Phys. J. C**54**, 1 (2000).
- [3] A.O. Bazarko et al., Phys. C **65**, 189 (1995).
- [4] T.P. Cheng, Phys. Rev. D **38**, 2869 (1988).
- [5] J. Gasser and H. Leutwyler, Nucl. Phys. B **250**, 465 (1985).
- [6] J. Gasser, H. Leutwyler, and M.E. Sainio, Phys. Lett. B **253**, 252 (1991).
- [7] T.P. Cheng and R.F. Dashen, Phys. Rev. Lett. **26**, 594 (1971).
- [8] R.L. Jaffe, A.V. Manohar, Nucl. Phys. B**337**, 509 (1990).
- [9] K. Abe et al., Phys. Lett. B**405**, 180 (1997).
- [10] G. Altarelli et al., Nucl. Phys. B**496**, 337 (1997).
- [11] A. Airapetian et al., Nucl. Phys. D**71**, 012003 (2005).
- [12] W.J. Marciano and J.L. Rosner, Phys. Rev. Lett. **65**, 2963 (1990).
- [13] S. Eidelman et al., Phys. Lett. B**592**, 1 (2004).
- [14] S.L. Zhu, S.J. Puglia, B.R. Holstein, and M.J. Ramsey-Musolf, Phys. Rev. D**62**, 033008 (2000).
- [15] J. Arrington, Phys. Rev. C**69**, 022201 (2004).
- [16] I.A. Qattan et al., Phys. Rev. Lett.**94**, 142301 (2005).



- [17] A.F. Sill et al, Phys. Rev. D**48**, 29 (1993).
- [18] J. Arrington, private communication.
- [19] H. Anklin et al., Phys. Lett. B **428**, 248 (1998).
- [20] G. Kubon et al. Phys. Lett. B, **524**, 26 (2002).
- [21] B. Anderson, et al., nucl-ex/0605006 .
- [22] H. Gao et al., Phys. Rev. C, **50**, 546-549 (1994).
- [23] C. Herberg, Eur. Phys. J. A **5**, 131 (1999).
- [24] I. Passchier et al, Phys. Rev. Lett. **82**, 4988 (1999).
- [25] R. Madey et al, Phys. Rev. Lett. **91**, 122002 (2003).
- [26] R. Schiavilla and I. Sick, Phys. Rev. C **64**, 041002 (2001).
- [27] J. Golak, Phys. Rev. C **63**, 034006 (2001).
- [28] D.I. Glazier et al, Eur. Phys. J. A **24**, 101 (2005).
- [29] G. Warren et al, Phys. Rev. Lett. **92**, 042301 (2004).
- [30] C. Crawford et al, new preprint.
- [31] O. Gayou et al, Phys. Rev. Lett. **88**, 092301 (2002).
- [32] O. Gayou et al, Phys. Rev. C **64**, 038202 (2001).
- [33] V. Punjabi et al, Phys. Rev. C **71**, 069902 (2005).
- [34] G. MacLachlan et al., Nucl. Phys. A **764**, 261 (2006).
- [35] M. Jones et al, new preprint, (2006).
- [36] T. Pospischil et al, Phys. Rev. Lett. **86**, 2959 (2001).
- [37] B. Milbrath et al, Phys. Rev. Lett. **80**, 452 (1998).

- [38] J. Arvieux, S. Baunack, E.J. Beise, M.A. El-Yakoubi, R. Frascaria, F. Maas, M. Morlet, J. Roche, and J. Van de Wiele, *Evaluation of Strange Form-Factors in Parity-Violating Electron Scattering*, Internal G0 Report, G0 Analysis Log: Analysis Notes 73.
- [39] H. Gao, Int. Journal of Modern Physics E **12**, 1 (2003)
- [40] J.J. Kelly, Phys. Rev. C. **70**, 068202 (2004).
- [41] J. Friedrich, T. Walcher, Eur. Phys. J. A,**17**, 607 (2003).
- [42] E.J. Beise, M.L. Pitt and D.T. Spayde, Prog. Part. Nucl. Phys. **54**, 289 (2005).
- [43] K.A. Aniol et al., Phys. Rev. C **69**, 065501 (2004).
- [44] K.A. Aniol et al., Phys. Lett. B **635**, 275 (2006).
- [45] K.A. Aniol et al., Phys. Rev. Lett. **96**, 022003 (2006).
- [46] A. Acha et. al, nucl-ex/0609002.
- [47] F.E. Maas et al., Phys. Rev. Lett. **93**, 022002 (2004).
- [48] F.E. Maas et al., Phys. Rev. Lett. **94**, 152001 (2005).
- [49] D.S. Armstrong et al., Phys. Rev. Lett. **95**, 134 (2005).
- [50] <http://www.npl.uiuc.edu/exp/G0/Forward/qq201.pdf>
- [51] S.D. Covrig et al., Nucl. Instrum. Meth. A**551**, 218 (2005).
- [52] R. Carr et al. ( $G^0$  collaboration), in preparation for Nucl. Instrum. Meth.
- [53] S. Wells, private communication.
- [54] S. Geraud, "Resonant Cavities (BCMs)." <http://www.jlab.org/geraud/bcms.html>
- [55] A. Slaughter, *Parity Violation in High-Energy Electron Scattering: Data Analysis for the  $G^0$  Experiment*, Senior Honors Thesis, William and Mary, 2004
- [56] D.S. Armstrong, B. Moffit, R. Suleiman, *Target Density Fluctuations and Bulk Boiling in Hall A Cryotarget*, JLab Technical Note JLAB-TN-03-017 (2003).

- [57] C. Ellis, private communication.
- [58] M. Hauger et al, Nucl.Instrum. Meth. A**462**, 382 (2001).
- [59] C.K. Sinclair, *Electron Beam Polarimetry*, Beam Instrumentation Workshop '98 (BIW98) conference proceedings
- [60] M. Steigerwald, *MeV Mott Polarimetry at Jefferson Lab*, The fourteenth international spin physics symposium, SPIN2000, AIP Conference Proceedings, Volume 570, 935-942 (2001).
- [61] <http://coda.jlab.org>
- [62] F. Benmokhtar, private communication.
- [63] <http://www.aps.anl.gov/epics/>
- [64] D. Schultz, R. Alley, J. Clendenin, J. Frisch, G. Mulhollan, P. Saez, H. Tang and K. Witte, *The Polarized Electron Source of the Stanford Linear Accelerator Center*, SLAC-PUB-6606, 1994.
- [65] P. Adderley, M. Baylac, J. Clark, T. Day, J. Grames, J. Hansknecht, M. Poelker and M. Stutzman, *Jefferson Lab Polarized Source*, Mainz Parity Workshop Proceedings, Mainz, 2002.
- [66] J. Hansknecht, private communication.
- [67] M. Pitt, et al., *Helicity Control Requests from the  $G^0$  Experiment*, Internal Report G0-doc-236-v1.
- [68] G.D. Cates, Eur. Phys. J.**24**, 109 (2005).
- [69] S. Bailey, *Laser Room Scans for HAPPEX and Backward Angles of the  $G^0$  Experiment*, Internal Report G0-doc-547-v2.
- [70] M. Muether, *Dilution Factors from SMS Field Scan Runs,  $G^0$  Backward Angle analysis Logbook Analysis Notes ID 14*, 2006.
- [71] M. Muether, private communication.
- [72] J. Liu, private communication.
- [73] J. Liu,  *$G^0$  Leakage Correction*, Internal Report G0-doc-551-v1, 2005.

- [74] D. Gaskell and S. Wood, private communication
- [75] J. Liu, *A Measurement of the Strange Quark Contributions to the Electromagnetic Form Factors of the Nucleon*, Ph.D. Dissertation, U. Maryland, 2006.
- [76] W.H. Press, B.P. Flannery, S.A. Teukolsky and W.T. Vetterling, *Numerical Recipes in C: The Art of Scientific Computing*, second ed., Cambridge University Press, 1992.
- [77] K. Nakahara, *Linear Regression*,  $G^0$  Forward Angle Analysis Logbook Analysis Notes ID 113, 2005.
- [78] T. Suwada, N. Kamikubota, K. Furukawa, H. Kobayashi, *Beam-Position Monitor System for the KEKB Injector Linac*, Beam Instrumentation Workshop '98 (BIW98) conference proceedings
- [79] E. Beise, *Simulation of detector slopes vs position at 687 MeV  $G^0$*  Backward Angle analysis Logbook Simulation Notes ID 46, 2006.
- [80] D. Gaskell, private communication.
- [81] L. Lee, *Cerenkov Efficiencies (preliminary) from 31 MHz data @ 687 MeV/c  $G^0$*  Backward Angle analysis Logbook Analysis Notes ID 13, 2006.
- [82] S. Eidelman et al., Phys. Lett. B.**592**, 1 (2004).
- [83] H. Budd, A. Bodek, J. Arrington, Nuclear Physics B.**139**, 90 (2005).
- [84] Y. Goto et al, Phys. Rev. D.**62**, 034017 (2000).
- [85] J. Arvieux et al., *Towards a Common PVA4-SAMPLE Analysis: a First Step*,  $G^0$  Internal Document, G0-doc-609-v1 (2005).

## VITA

### Stephanie Louise Bailey

Stephanie Louise Bailey was born in Santa Rosa, California on May 17th 1979 to Michael and Deborah Bailey. She received her Bachelor of Science degree in physics at the College of William and Mary in 2002. As an undergraduate, she pursued research in a variety of fields. Among these were Cryogenics and Astrophysics at the NASA Goddard Space Flight Center, Nondestructive Evaluation Sciences at the NASA Langley Research Center, Biophysics at the Los Alamos National Laboratory, Condensed Matter Theory at the University of Chicago, and Nuclear Physics at the Thomas Jefferson National Accelerator Facility. In the Spring of 2003, she earned a Diploma of Advanced Studies (DEA) in Experimental Physical Methods from the Joint Universities Accelerator School, organized by the European Scientific Institute, in Archamps, France. This was followed by a technical placement in Accelerator Theory at the European Synchrotron Radiation Facility in Grenoble, France. She earned a Master of Science in 2004 from the College of William and Mary. As a graduate student at Jefferson Lab, she had opportunities to meet and make presentations to both the Secretary of Energy Samuel Bodman and Virginia Senator George Allen. This dissertation was defended on January 8th 2007 at the College of William and Mary. Currently, Stephanie is a National Cancer Institute (NCI) postdoctoral fellow in the Radiology Department at the Stanford University School of Medicine.